In-depth Understanding of Multilayered Photoelectrodes for Water Splitting Using *Operando* Electrochemical Methodologies

---

Dissertation*

zur

Erlangung der naturwissenschaftlichen Doktorwürde
(Dr. sc. nat.)

vorgelegt der

Mathematisch-naturwissenschaftlichen Fakultät

der

Universität Zürich

von

Wei Cui

aus der V. R. China

Prof. Dr. David Tilley (Leitung der Dissertation)

Prof. Dr. Greta R. Patzke

Prof. Dr. Karl-Heinz Ernst

Zürich, 2019

Abstract

Photoelectrochemical (PEC) water splitting has been considered as a potential technology to convert quasi-infinite solar energy into clean H_2 chemical fuel. Over decades, a vast amount of research effort has focused on the design of multilayered photoelectrodes to achieve improved solar-to-H_2 efficiency and long-term stability. However, due to the high complexity of this multilayer configuration, the traditional electrochemical characterization method involving current–voltage curves with a three-electrode setup is not able to ascertain an in-depth understanding of several fundamental issues in these systems, including properties of the buried junction, the electrode degradation mechanism and charge carrier processes under realistic photo-electrolysis conditions.

This thesis details our work in utilizing *operando* electrochemical techniques to study the above-mentioned issues. Chapter 1 presents the basic knowledge and principle of PEC water splitting, semiconductors, and introduces different functional layers in a photoelectrode. The common electrochemical techniques to examine a photoelectrode were then discussed as well as their limitation in characterization.

Then we used the dual-working-electrode (DWE) technique in Chapter 2 and 3, where a second working electrode (WE2) was introduced to probe *in situ* the surface potential of a $pn^+Si/TiO_2/Pt$ photocathode for H_2 generation. The traditional three-electrode setup–including a working electrode (WE1), a reference electrode and a counter electrode–can only provide the overall PEC performance, which is represented by a photocurrent density-back contact potential curve (J-V1 curve). With the help of the WE2, the photovoltaic performance of the buried pn^+Si junction can be extracted, which is represented by a J-ΔV curve. By comparing the J-ΔV curves before and after a long-term photoelectrolysis test, the degradation mechanism of the photocathode could be revealed: for the $pn^+Si/TiO_2/Pt$ photocathode, the J-ΔV curve showed a negligible change after the long-term test, implying that the pn^+Si junction was stable, as expected; for the $Cu_2O/Ga_2O_3/TiO_2/Pt$ photocathode, the J-ΔV curve showed an obvious loss in open circuit voltage (V_{OC}), suggesting an instability of the Cu_2O/Ga_2O_3 junction under

operational conditions. Moreover, the DWE technique was applied to assess emerging materials (Sb_2Se_3/Sb_2S_3) and new methods such as tunable dipole layers (p-Si/Phosphonic acid (PA)/TiO_2 photocathodes). The Sb_2S_3 formation during the post-sulfurization of Sb_2Se_3 produced enhanced photovoltage; the PA layer also increased the V_{OC} generated by p-Si/TiO_2 junction and exhibited good stability.

In Chapter 4 and 5, photoelectrochemical impedance spectroscopy (PEIS) was applied to investigate charge-carrier processes in TiO_2-protected photoanodes. For the np^+-Si/TiO_2/Ni photoanode, several basic processes were deconvoluted and studied in the form of equivalent resistances: (1) photo-excited electron-hole pair recombination inside the np^+-Si junction (R_{rec}); (2) hole transport through the TiO_2 (R_{TiO2}); (3) water oxidation by holes at the Ni-based water oxidation catalyst (R_{ct}). Moreover, we further elucidated the “hole leaky” property of TiO_2. R_{TiO2} of both np^+Si/TiO_2/Ni and nSi/TiO_2/Ni photoanodes, did not show a clear thickness dependence, suggesting that a conduction band mechanism was applicable. In addition, results from the DWE measurements strongly suggest that the “hole-leaky” property of TiO_2 can be interpreted by charge transport in the conduction band, in spite of the presence of the defect states in TiO_2. Last but not least, it was found that the R_{TiO2} behaved differently in the nSi/TiO_2/Ni. R_{TiO2} increased as the photocurrent increases, which was interpreted by trapping in the defect states present at the interface of the nSi/TiO_2. Therefore, a detailed picture of charge carriers process in both the np^+Si/TiO_2/Ni and nSi/TiO_2/Ni photoanodes has been achieved.

Chapter 6 concludes this comprehensive *operando* study of photoelectrodes realized by the DWE technique and PEIS. Several unclear issues are then laid out, and suggestions for future research are put forward.

Acknowledgements

I would like to express my gratitude to all those who helped me during my PhD study at the University of Zurich.

First of all, my sincerest thanks goes to my respected supervisor, Prof. David Tilley. This thesis would not be completed without his guidance and input. He led me in to such a challenging but fascinating research area. In the past 4 years, he has given me lots of patient instructions and constructive suggestions. Beyond research, he is also a talented teacher but also a good friend to me.

Next, I would like to give special thanks to my colleague, Dr. Thomas Moehl, who has broadened the scope of my knowledge and taught me many critical approaches in electrochemical and structural characterizations. He always let me “harass” him and encouraged me when I felt loss.

I express my thanks to all members of the Tilley group. Dr. Wooseok Yang, Dr. Laxman Gouda, Dr. René Wick-Joliat, Dr. Laurent Sévery, Rajiv Prabhakar, Jihye Suh, Xi Zhang, Erin Service, Jonas Zurflüh, Casey Beall, Dhananjeya Kumaar, and all former members, Dr. Magdalena Marszalek, Dr. Whenzhe Niu, Dr. Wilman Septina Conner Firth, Antony Sibilia and Marin Nikolic. They made my daily life inside and outside the laboratory so wonderful and I was very lucky to become friends with all of them.

I would also like to thank all members of the LightChEC. I thank Prof. Greta Patzke and Prof. Karl-Heinz Ernst for being my committee members, and I thank Prof. Roger Alberto and Prof. Chunhua Cui for giving me insightful scientific tips and kind support for my academic career.

I express my thanks to our assistant, Ramona Erni, and HR members, Maja Gossweiler and Larissa Mostacciuolo, for helping me to survive in Switzerland.

I would like to thank Dr. Sebastian Siol from The Swiss Federal Laboratories for Materials Science and Technology (EMPA) for the XPS measurements and data analysis.

I also thank Dr. Andres Käch and Gery Barmettler from the Center for Microscopy and

Image Analysis for their kind support on thin film deposition and morphology characterization.

Last but not the least, my gratitude would go to my beloved parents. They gave me life and all their love. Through all these years, they were always very supportive of me to study abroad and pursue my dream.

Contents

1 Introduction

1.1 Solar energy utilization

1.1.1 Solar energy conversion

The earth is beginning to show a limitation for supporting human beings due to the fast growing human population and resulting intensive demands of energy and materials from the natural environment on earth. The industrialization and modernization of human society was established on fossil fuels, including, oil and natural gas.[1,2] To date, burning fossil fuels still supplies most of the energy in the world.[3] However, with the rapidly increasing consumption and decreasing resources, the fossil fuel supply won't last long since they are not renewable (on a human time scale). For instance, it is predicted that oil deposits will run out in around 50 years.[4] Additionally, fossil fuels account for 90% of global carbon emissions from human activity, and the global temperature is rising.[5,6] Moreover, plundering the earth for fossil fuels causes other environmental issues, including habitat destruction as well as air and ocean pollution, which are getting worse as the population increases.[7] Hence there is a need for a growing awareness to achieve a more sustainable societal use of materials.

From the sun radiation, the earth receives 1.2×10^5 TW of power,[8] much more than the amount of current global energy demand (~ 18.6 TW, for the year of 2020).[9] Solar energy is silent, infinite, and non-polluting. To be utilized, the solar radiation needs to be converted into other forms of energy. Generally, there are three approaches:

Conversion to usable heat via thermal collectors: the process of solar heat conversion involves concentrating solar radiation and transferring the heat to a carrier fluid in a tube.[10]

Conversion to electricity via photovoltaic (PV) effect: PV cells, also known as solar cells, are made of semiconductors such as silicon (Si), which is currently the most commonly used. In general, when sunlight shines on the solar cell, a portion of the solar radiation is absorbed by the semiconductor material. This solar energy will excite the electrons, which flow to form electric current.[11]

Conversion to chemical fuels (e.g., photocatalytic water splitting and biomass formation through artificial photosynthesis): there is a drawback in the storage for solar heat and PVs since they do not produce a sufficient amount of heat or electricity during cloudy weather or at night. Converting solar energy to chemical fuels is not only "utilization" of solar energy but also demonstrates the "storage" of solar energy in the form of chemical bonds. Indeed, this occurs in nature. The photosynthesis by plants turns water and CO_2 into sugars, releases O_2 and makes the earth hospitable to life.[12] Inspired by natural photosynthesis, the concept of "solar fuels" refers to utilizing and converting solar energy to generate molecules, such as hydrogen (H_2)[13] and methanol (CH_3OH)[14], as the energy carrier from water and CO_2, respectively. In particular, H_2, is a carbon-free energy and with the highest gravimetric energy density ($J\ kg^{-1}$) has been considered as the ultimate sustainable energy carrier.[15,16] Solar energy conversion into H_2 gas can be realized in three ways: (1) direct photocatalytic overall water splitting by a photocatalyst, which is the simplest fashion but suffers from the low solar-to–hydrogen efficiency;[17] (2) utilizing solar electricity to drive the electrolysis, also named as PV-electrolysis;[18,19] (3) photoelectrochemical (PEC) water splitting, which demonstrates the direct electrolysis driven by a semiconductor-based electrode under illumination.[20] In the thesis, we only focus on the PEC water splitting process.

1.1.2 The principle of PEC water splitting

Before diving into the details of the basic components and fundamentals of PEC water splitting systems, let us first understand the general principle of PEC water splitting. Figure 1-1 illustrates fundamental processes in a PEC device of a two-electrode system, including a p-type semiconductor-based photocathode and a metal anode. Incident photons (hv) with sufficient energy generate electron-hole pairs, which then separate and travel through the semiconductor in opposite directions. The electrons transfer through the photocathode, enter the electrolyte solution and reduce protons into hydrogen gas, while holes are driven through the electrical connection to the metal anode to oxidize water into oxygen. These carriers must have sufficient potential to drive the water reduction and oxidation reactions, whose thermodynamic potentials are 0 and 1.23 V vs. RHE (reversible hydrogen electrode), respectively.

The semiconductor material is the core component for a photoelectrode. In the next section, the basic concepts and terminologies of semiconductor are presented.

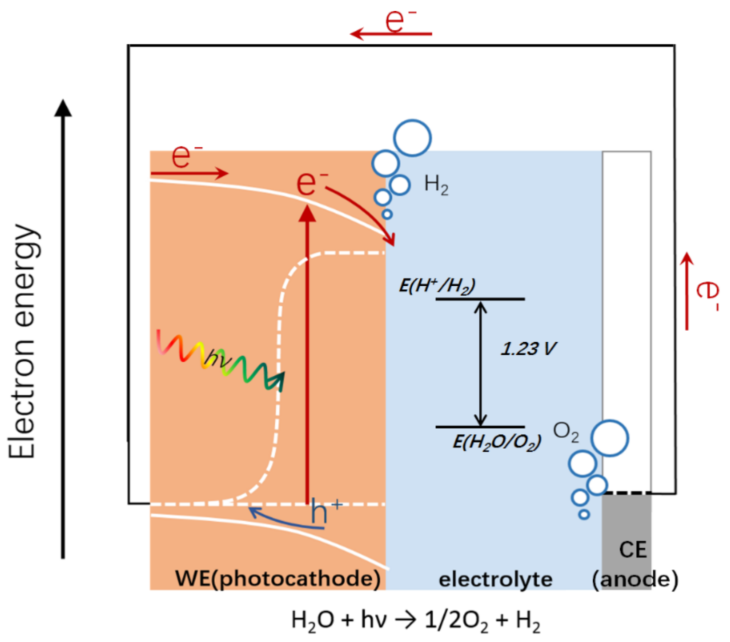

Figure 1-1 Band structure of a p-type photocathode water splitting device.

1.2 Semiconductor basics

1.2.1 Fundamental concepts

Generally, the concept of a “semiconductor” refers to a material or compound with electrical properties between a “conductor” and an “insulator”. Conductors such as gold (Au), copper (Cu) and other metals permit the flow of electrons, while insulators such as glass and rubber, block the flow of electrons. Representative semiconductors are silicon (Si), germanium (Ge), GaAs and so on.

To visualize the difference of insulators, semiconductors and conductors, the available potential energies of the electrons in the materials need to be plotted. Electrons in one free atom can only be found in certain discrete energy states, which are associated with the atomic orbitals. When two of the same atoms are brought close together, their energy levels become degenerate, further splitting into two separate energy levels. When numerous atoms form a solid, energy levels in the atoms are grouped and mixed, finally resulting in a continuous “band” of energy states. The band occupied by valence electrons is called the valence band, while the almost empty band is then called the conduction band. In a band diagram, energy bands are represented by horizontal lines, as shown in Figure 1-2.

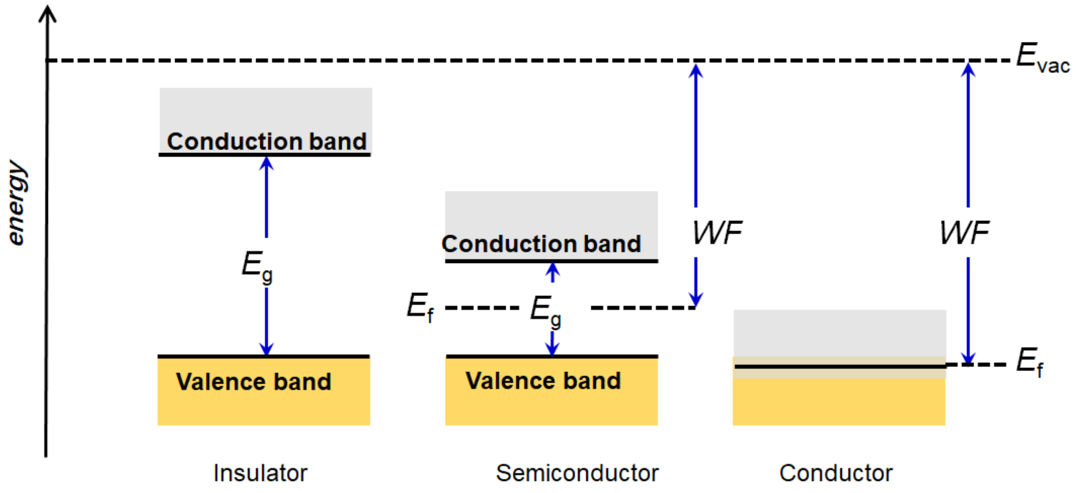

Figure 1-2 Band energy diagram of an insulator, a semiconductor and a conductor. Concepts including the band gap (E_g), vacuum level (E_{VAC}), Fermi level (E_f) and work function (WF), are defined.

When excited by enough additional energy (*e.g.*, heat and/or light), those electrons can be excited from the valence band to the conduction band and become free electrons, which are able to move in the material. The energy gap between the valence and conduction band is called the band gap (E_g). Figure 1-2 illustrates the band gap for insulators, semiconductors and conductors. In insulators, the band gap is very large and there are essentially no free charge carriers at room temperature. For semiconductors, the band gap is smaller, allowing electron excitation from the valence band to the conduction band under non-extreme condition such as visible light or room temperature. The visible light wavelength ranges approximately from 390 to 700 nm, corresponding to a semiconductor with E_g from 3.2 to 1.8 eV, respectively, according to the Formula 1-1:

$$E = \frac{hc}{\lambda} \qquad (1\text{-}1)$$

where E (eV) is the photon's energy or band gap, h is the Planck constant (4.136×10^{-15} eV s), c is the speed of light in vacuum (3.15×10^{8} m s^{-1}) and λ (nm) is the photon's wavelength. Regarding conductors, there is no gap between the conduction and valence band and electrons are thus always free to move.

To quantify and measure the energy of electrons, several important parameters are schematically shown in Figure 1-2 and described as follows:

(1) **Vacuum level (E_{VAC})**. E_{VAC} is the reference to measure the energy level. It refers to the energy level of a free stationary electron at infinite distance from the solid with zero kinetic energy.

(2) **Fermi level (E_f)**. The Fermi level is the electrochemical potential of electrons in the solid. E_f is the energy level which has a 50% probability of being occupied by an electron at any temperature. This is why the E_f lies in the middle of the bandgap of an intrinsic semiconductor (Figure 1-2). Another definition can be "E_f is the average energy of a crystal at any temperature".[21] When a material is under a bias potential, the E_f across the material will be equilibrated with the external potential.

(3) **Work function (WF)**. WF is the energy (or work) needed to withdraw an electron from a solid surface. As can be seen in Figure 1-2, WF = E_{vac} - E_f.

1.2.2 Light absorbing-semiconductors for water splitting

Semiconductors are at the heart of a photoelectrode. For the achievement of good solar energy conversion efficiency, a semiconductor should have a high optical absorption coefficient and a suitable band gap (E_g) and valence and conduction band edges. Additionally, the light absorbing-photovoltage trade-off must be considered. When illuminated, semiconductors with narrow E_g generate small photovoltages while semiconductors with E_g > 3.1 eV can hardly absorb visible light. Another critical point is the energy positions of band edges. For the O_2-evolving photoanode, the light-absorbing semiconductor must have a valence band maximum (VBM) which is more positive than the thermodynamic potential of water oxidation (O_2/H_2O, 1.23 V_{RHE}). Similarly, a semiconductor acting as the light absorber in the H_2-evolving photocathode must have a conduction band minimum (CBM) located more negative than thermodynamic potential of water reduction (H^+/H_2, 0 V_{RHE}). However, the poor surface kinetics for O_2/H_2-evolution will result in extra overpotential during photoelectrolysis. Therefore, some semiconductors cannot be operative alone despite the fact that their band structures satisfy the above thermodynamic criteria, and electrocatalysts on the surface are required.

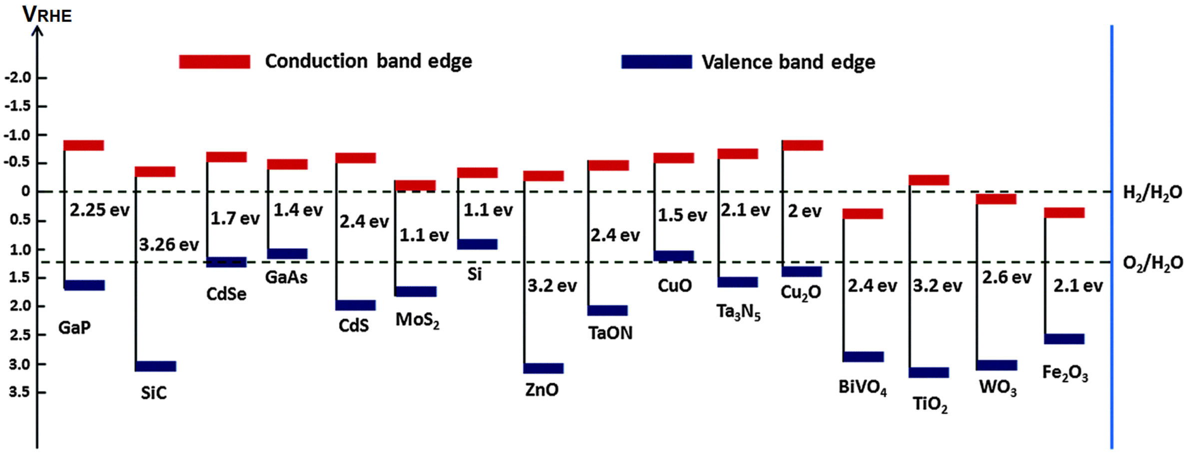

Figure 1-3 Band edge positions of several semiconductors. The energy scale is versus to the reversible hydrogen electrode (RHE).[22]

Metal oxides, including $BiVO_4$,[23] α-Fe_2O_3[24,25] and WO_3,[26–28] are the most commonly used n-type semiconductors for photoanodes. As presented by Figure 1-3,[22] E_g is ~2.4 eV for $BiVO_4$, ~2.2 eV for α-Fe_2O_3 and ~2.6 eV for WO_3, and corresponding to visible-light absorption with wavelength edges of about ~520, ~560 and ~480 nm, respectively. All of these three material have a >1 eV lower valence band position than 1.23 V_{RHE}, which indicates that they are applicable suitable as the light absorber for an O_2-evolving photoanode. However, their conduction band edges are all located positive of 0 V_{RHE}, which means that an electrical bias is required achieve overall water splitting.

Ta_3N_5 has a modest E_g (2.1 eV), allowing to absorb visible light with wavelength up to to ~600 nm. Besides, it has very ideal band energy positions, straddling the $E(O_2/H_2O)$ and $E(H^+/H_2)$ thermodynamic potentials. However, the practical use of Ta_3N_5 is limited by the poor stability under PEC water splitting condition, where the N anions can be also oxidized into N_2 by photo-excited holes.[29,30] Similar stability issues limit the use of p-type Cu_2O as the photocathode material in spite of the nearly ideal E_g. In the water splitting potential range, Cu_2O can be oxidized to CuO and be reduced to metallic Cu as well.[31–33] Fortunately, this photocorrosion problem can be solved by adding a protective layer, which will be presented in section 1.3.2.

1.2.3 N- and p-type semiconductors

One significant feature of a semiconductor is that its conductivity can be tuned with doped impurities. Taking crystalline Si as an example: when introducing a pentavalent phosphorous

(P) atom into the Si lattice, four valence electrons of P are covalently bonded with neighbored valence electrons of Si and the 5th valence electron of P is delocalized in the conduction band. Consequently, there are free electrons present within the structure of the P-doped Si. Since electrons are the majority carriers in the P-doped Si, the P-doped Si is also named n-type Si ("n" means negative charge) and P atoms are donors. In a n-type semiconductor, donors form a donor level near the conduction band. This means that the electrons in these states require a much smaller extra energy to be excited into the conduction band. As a result, the Fermi level will increase from the intrinsic position (the middle of the band gap) towards the conduction band, as shown in Figure 1-4a.

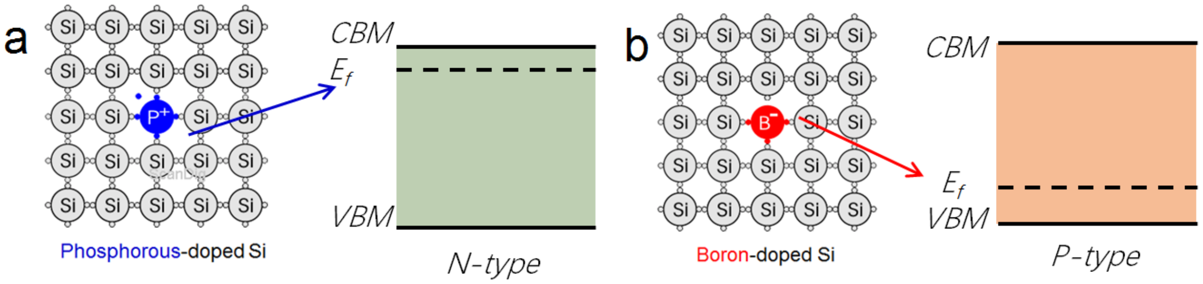

Figure 1-4 Simple diagrams representing the Si lattice with an impurity atom of (a) phosphorous, which produces n-type Si, and (b) boron, which produces p-type Si. CBM and VBM are the conduction band minimum and valence band maximum, respectively**.**

In contrast, when the dopants are 3-valent atoms, *e.g.* boron (B), only 3 of the four Si valence electrons can be bonded. The boron atom accepts an electron from the valence band, leaving a delocalized hole in the valence band. The dopant B atoms are thus considered as "acceptors" and the B-doped Si is also denoted as p-type Si, where "p" means positive charge. At room temperature, in p-type Si, holes are the majority carriers and electrons are the minority carriers. Similarly, in a p-type semiconductor, an acceptor level will form in the band gap but near the valence band. This makes the Fermi level move down and close to the valence band (Figure 1-4b).

When a semiconductor is heavily doped, the Fermi level position will be quite close to the conduction/valence band for a n/p-type material, respectively, and the material will behave more like a metal. A semiconductor with such high doping density is called a degenerate semiconductor.

1.2.4 The p-n junction

The p-n junction, consisting of two semiconductors with opposite type, is an important basic element in semiconductor-based devices. Typically, the p-n junction is a rectifying junction, and is also called the p-n diode. The use of a p-n junction is versatile, including for photodiodes, photovoltaics, light emitting diodes and so on. Figure 1-5 shows the band diagrams before and after the contact of a p- and n-type semiconductors. Due to the diffusion effect by concentration, after contacting, electrons diffuse from the n-side to the p- side and leave behind exposed positive charges on dopant atom sites, which are stationary and fixed in the lattice. Similarly, holes diffuse from p-side to n-side and leave stationary negative charges. Finally, all the free charges are depleted in the junction region. Therefore, this region is called depletion region (or space charge region). As shown in Figure 1-5b, at equilibrium, the space charge region (SCR) extends at both the n- and p-side, and the Fermi level is equal across the junction. This creates a band bending with an energy barrier height (qV_D), which is equal to the Fermi level difference of the n- and p-type materials.

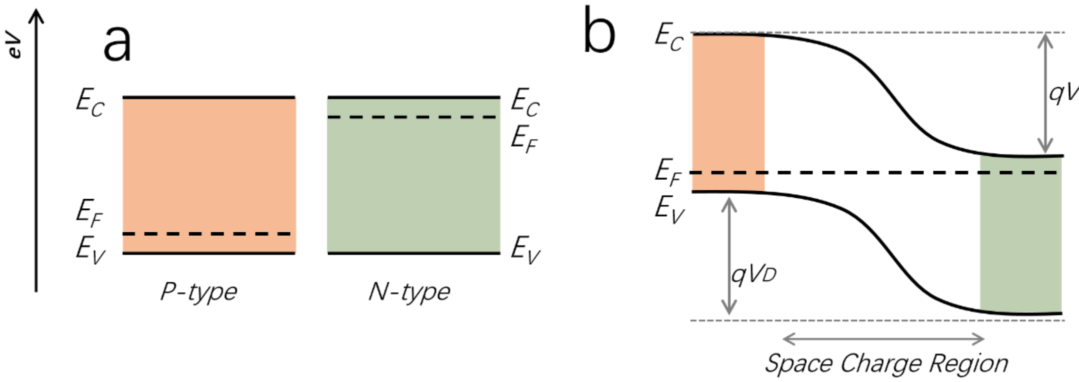

Figure 1-5 (a) Band structure of p-type and n-type semiconductors. E_C and E_V are the energy position of the conduction band minimum and valence band maximum of a semiconductor, respectively. E_f is the Fermi level. (b) Band diagram in the p-n junction. The qV_D is the energy barrier generated by the band bending in the p-n junction

1.2.5 The semiconductor/liquid interface

The simplest fashion of a PEC device is based on the semiconductor/liquid interface. The liquid phase is usually an electrolyte solution containing redox pairs. The electrochemical potential of the solution is determined by the Nernst equation and treated as the Fermi level of the solution, represented as $E_{f,redox}$. As depicted in Figure 1-6, if the $E_{f,redox}$ is lower than the E_f of a n-type semiconductor, after contact, electron will flow from semiconductor to the solution and leave positive charges behind in the space charge region of the semiconductor. As a result, the E_f of the semiconductor near the interface moves downward from the conduction band and an upward band bending is created within the semiconductor near the interface (the depletion condition). Under equilibrium, the Fermi level across the system is constant and this junction behaves like a Schottky junction, blocking electrons in the conduction band entering the solution by an energetic barrier (V_{sc}). If $E_{f,redox}$ is located at the same level as E_f before contact, there will be no band bending in the semiconductor after contact, which is the flat band condition. If $E_{f,redox}$ is higher than the E_f, after contact excess electrons will be injected into the semiconductor and accumulate near the interface and a downward band bending thus forms (the accumulation condition). For the p-semiconductor/liquid interface, the band bending condition is in the reverse direction, as shown in Figure 1-6.

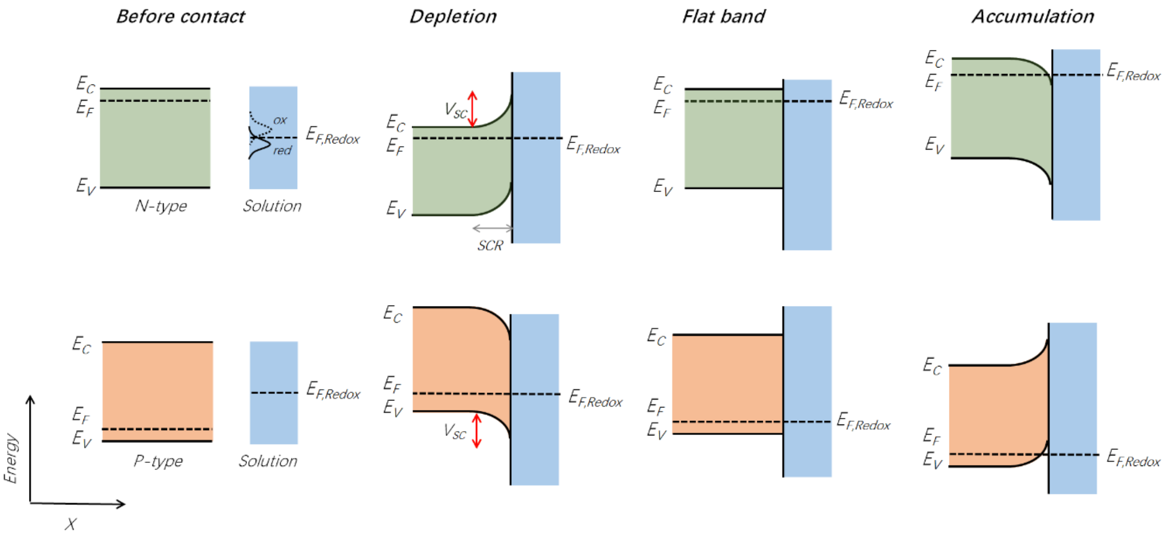

Figure 1-6 Schematic illustrations of the band bending diagram between a semiconductor and an electrolyte containing a redox couple**.** Four situations are indicated: before contact, depletion, flat band and accumulation. The first row is an n-type semiconductor/liquid interface; the second row is a p-type semiconductor/liquid interface. V_{sc} represents the energy barrier created by the band bending within the space charge region.

Next the semiconductor/liquid interface under illumination is discussed by considering a p-Si electrode in a strong acidic solution. As shown in Figure 1-7a, under dark condition, the E_f of p-Si is equilibrated with the $E(H^+/H_2)$ and the net result is that a downward band bending is created within p-Si near the interface. Under illumination, extra electrons (minority carrier for p-Si) and are excited from the valence band to the conduction band, causing the redistribution of charges within the depletion region. This results in the Fermi level splitting in p-Si into the quasi-Fermi levels of electrons and holes ($E_{f,n}$ and $E_{f,p}$, respectively), as shown in Figure 1-7b. Compared to holes, the electrons show a significant concentration change under illumination, therefore, the $E_{f,n}$ is located different from the E_f in dark condition and form equilibrium with $E(H^+/H_2)$. The potential difference between $E_{f,n}$ and $E_{f,p}$, refers to the so-called photovoltage or open-circuit voltage (V_{oc}).

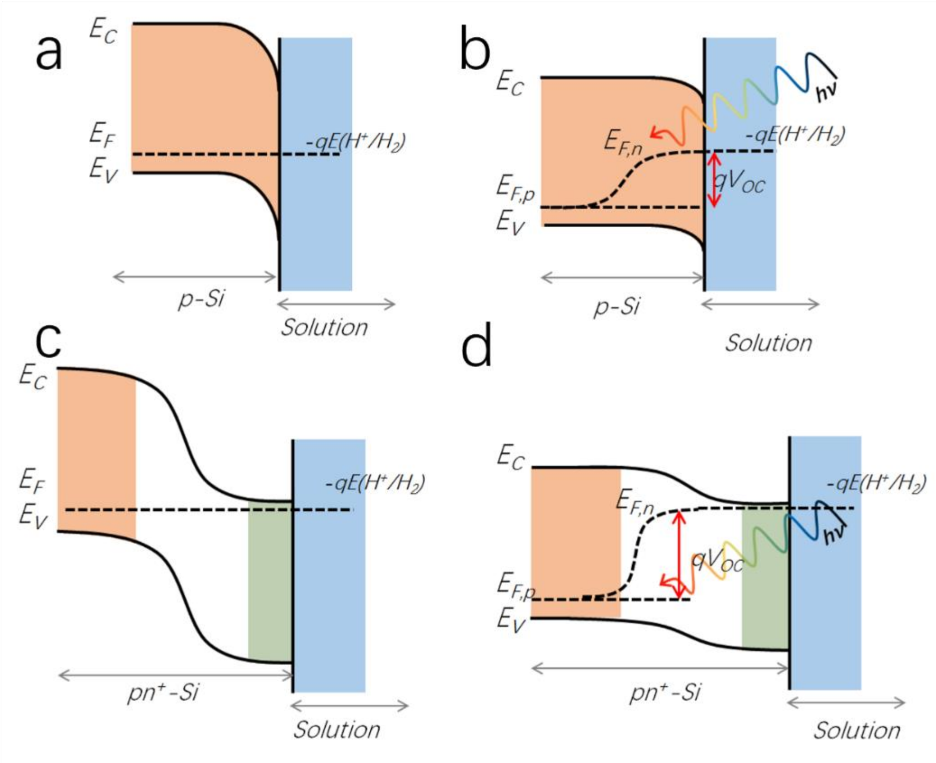

Figure 1-7 Band diagram of pSi in contact with the H^+/H_2 redox couple in solution in (a) dark and (b) light condition. Band diagram of pn^+Si /electrolyte interface in the (c) dark and (d) light condition. $E_{f,p}$ and $E_{f,n}$ are the hole and electron quasi-Fermi levels, respectively, under illumination. Larger photovoltage (V_{oc}) is achieved from pn^+Si/electrolyte contact

The maximum V_{oc} of a photocathode is determined by the relative position of E_f of pSi and

$E(H^+/H_2)$. As for p-Si, the valence band position is ~ 0.6 V lower than $E(H^+/H_2)$ band and the theoretical V_{oc} should be less, in practical, only ~ 0.2 V is achieved.[34] To obtain larger V_{oc}, a buried junction fashion has been designed where in a p-n Si homojunction is involved instead of p-Si. In dark condition, an increased band bending at the p/n^+ interface forms, resulting from the energetic equilibrium across the system (Figure 1-7c). As discussed in section 1.2.4, the V_{oc} is determined by the buried p-n Si junction, in other words, by the Fermi level difference of the n and p side. Hence, the generated V_{oc} is decoupled from the $E(H^+/H_2)$, as shown in Figure 1-7d. Using a degenerated n^+-Si can even enhance the V_{oc}. In the Chapter 2, a V_{oc} of 0.5 V is gained. In a nutshell, this buried-junction fashion allows the versatile design of the underneath junction to obtain larger V_{oc}.

1.3 Multilayer structured photoelectrodes

In 1972, PEC water splitting was first demonstrated by Fujishima and Honda, who used a rutile TiO_2 as the n-type photoabosrber material for O_2 generation.[35] Since this pioneering work, semiconductor-based water splitting photoelectrodes has been extensively studied aiming to improve both the performance and stability.[36–39] Ideal photoelectrodes need to meet several criteria: broad visible absorption, efficient photogenerated carrier transfer, catalytic surface, good stability and so on. All these concerns have lead the tremendous efforts in designing and fabrication of photoelectrodes with the multilayer structured configuration.[40,41] In the following section, we will introduce the involved component layers with different functions: a buried junction (in most cases is a pn-junction) is used to generate large photovoltage;[42,43] a protective layer to protect the semiconductor from photocorrosion;[44,45] surface catalyst to facilitate the water splitting half reaction.[46,47]

1.3.1 Protective layers

One of the largest barriers to be overcome is to achieve a stable PEC reaction without degradation of the semiconductor photoelectrodes in aqueous electrolytes. Most photoelectrodes with relatively high photocurrents, such as Si and III–V, are prone to be corroded quickly when in contact with an aqueous electrolyte and, in general, these materials have a very narrow window of stability based on Pourbaix diagrams.[48–50] So far, various protection layers have been evaluated, and can be generally divided into two categories: transparent oxides and metal catalyst layers. The most common oxide is TiO_2, which has been proven for both photocathodes and photoanodes in a wide range of pH levels from acidic to alkaline, owing to its intrinsic chemical stability.[51,52] For examples, >100 h stability has been achieved from a nSi/Ni photoanode with a 150 nm amorphous TiO_2 protective layer in strong alkaline solution (1 M KOH).[53] Another promising transparent oxide candidate is SnO_2. Azevedo and co-workers reported that the SnO_2-protected Cu_2O photocathode maintained 90% of initial photocurrent after long term photo-electrolysis (57 h).[54] Regarding the metal catalyst protective layer, one representative example is Ni-protected photoanodes[55]. Pt and Ni also function as the H_2 and O_2-evolving catalyst. Note that Ni surface will be oxidized under water oxidation operation.[56,57]

Adding an extra protective layer raises crucial fundamental questions about charge-transfer kinetics and interface energetics. For example, the thickness of the protective layer should be considered. For oxides, the resistance increases with the thickness and the charge transfer will be inhibited. For metals, the increased thickness leads to the optical transmission loss, resulting in a decreased photocurrent. The metal layer cannot be too thin, otherwise electrolyte can penetrate and the semiconductor will be corroded.[58]

1.3.2 Electrocatalyst

1.3.2.1 Water oxidation electrocatalyst

The four-electron involved water oxidation half-reaction ($2H_2O(l) \rightarrow O_2(g) + 4H^+(aq) + 4e^-$) suffers slow kinetics, which limits the efficiency of both photon-driven and electricity-driven water splitting. A calculated volcano plot can be used to evaluate metal oxides' catalytic activity towards water oxidation.[59] Representative oxides include IrO_2,[60–62] RuO_2,[63,64] NiO_x,[65,66] CoO_x[67,68] and MnO_x.[69,70] IrO_2 has been considered as the best water oxidation electrocatalyst with the smallest overpotential (< 200 mV) and has been applied to the hematite photoanode. But the high cost limits its practical use. Even though earth-abundant materials, such as NiO_x and CoO_x, have been investigated as the water oxidation catalyst, they did not show a comparable catalytic performance to IrO_2.[71,72] Fortunately, the performance of NiO_x, CoO_x can be further improved by Fe doping[73–75]. Another, widely used water oxidation catalyst is cobalt phosphate (Co-Pi), which has been demonstrated a comparable activity to IrO_2 in neutral electrolyte solutions.[76,77] Co–Pi can efficiently collect and store photogenerated holes from the semiconductor, reducing the surface charge recombination rate. Co-Pi-coated $BiVO_4$ photoanode has shown an onset potential shifted by 0.4 V.[78]

1.3.2.2 Water reduction electrocatalyst

Similarly, the volcano plot can also predict water reduction catalytic performance of various metals or alloys. To date, Pt and Pt-based materials still exhibits the best intrinsic catalytic activity with nearly zero onset potential.[79–81] When coupled with p-type semiconductor in a photocathode, the work function of the metal (thin film) is a critical parameter, which determines the electric field in the Schottky junction (metal-semiconductor) to drive electron transfer to the surface.[82,83] Considering this, Pt, with the largest work function of metals (6.3 eV), is still the most promising catalyst candidate for photocathodes. However, Pt-based materials suffer from the scarcity and cost issues as well. Therefore, researchers have made huge efforts on developing new water reduction catalyst based on an earth-abundant material. The most representative candidate is MoS_2 or (MoS_x).[84] MoS_2 is a two-dimension material with layered structure and nano-structuring is a widely used strategy to enhance the catalytic activity of MoS_2 by exposing more active sites.[85]

1.3.2.3 The semiconductor/electrocatalyst interface

Understanding the semiconductor/electrocatalyst (SC-EC) interface is critical for designing PEC deceives with high performance. As mentioned before, most SC-EC interfaces can be simply treated as the Schottky junctions in photocathodes. However, this interface gets more complicated for photoanodes since most O_2-evolving catalysts are oxides with multiple metal valence states, which can make the semiconductor/electrocatalyst junction behavior changeable within the working potential windows.[56,86] The origin of the performance enhancement by those catalyst has been intensively studied. Even for Co-Pi catalyst, several mechanism has been proposed. Some work suggested that the Co-Pi passivated the surface states and reduced electron-hole recombination at the semiconductor surface.[78] Some work suggested that Co-Pi formed a Schottky junction with semiconductor, created stronger band bending and improve the charge separation.[87] While another work demonstrated that Co-Pi collected holes and the oxidized Co species catalyzed the water oxidation.[86]

1.3.3 Thin layer deposition techniques.

Various techniques have been developed to produce thin films and here we categorize them into three major groups: solution-process thin film deposition, physical vapor deposition and chemical deposition. For fabricating a photoelectrode with multilayer structure, the flexibility of choosing different techniques guarantees to realize the desirable features of different layers.

1.3.3.1 Solution-process deposition

Solution process deposition is the general category of a serious techniques of thin layer deposition with solution-phase precursors, including drop-casting,[88,89] spin coating,[90,91] chemical bath deposition (CBD),[92,93] (photo)electrodeposition,[94,95] spray pyrolysis[96,97] and so on. The prominent advantage of solution-process deposition is to allow the thin film fabrication directly in a solution or under ambient air process, relaxing the implement requirements of ultra-vacuum. However, the synthesis conditions are usually insufficient to achieve high quality crystallinity. Hence, a post- annealing treatment is included. Here we mainly introduce CBD and electrodeposition. CBD is a widely used technique for semiconductor film deposition where substrates are immersed in solutions with ions as the precursor for the target composite, such as hydroxide, sulfide and so on. The as-deposited film by CBD is usually porous and with a rough surface, which can play an important role in governing the charge carrier process across the photoelectrode. A large number of martials has been produced by CBD, including CdS,[98,99] ZnSe,[100,101] CuS[102,103] and Bi_2S_3[104,105]. However, CBD often suffers from lack of reproducibility.[106]. Electrodeposition requires a conductive substrate and a counter electrode. A wide range of materials, including polymers, metals, oxides, chalcogenides, have been electrodeposited since thermodynamic requirements for a redox reaction can be easily satisfied by applying an electrical potential.[107–109] Regarding the PEC devices, electrodeposition is often used for growing semiconductors (*e. g.* p-type Cu_2O[110,111]) and surface catalysts (*e. g.* Pt,[112] RuO_x[33] and Co-Pi[86]).

1.3.3.2 Physical vapor deposition

Physical vapor deposition (PVD) is characterized by using physical means to vaporize target materials which subsequently deposit onto the receiving substrates. The methods to generate vapor of target materials include heat (*e.g.* thermal evaporation[113]), plasma (*e.g.* sputtering[114]), electron beam (e.g. e-beam evaporation[115]) and laser (*e.g.* pulse laser deposition[116]). Because nearly no chemical processes will occur inside the PVD setup, the purity of as-deposited thin films only depends on the target materials. This ensures the high purity and quality of the deposited thin films. Another key advantage of PVD is versatility. For example, the widest use of PVD is to produce single/multiple metal layers, which can serve as back contacts (Mo,[117] Cr/Au), protective layers (Ti/TiO_2[118]) and surface electrocatalyst (Ni[119]) for PEC devices. Moreover, polycrystalline chalcogenide semiconductor, such as CdZnSe composite films has been deposited by molecular beam epitaxy (MBE).[120,121] Compared with solution-based methods, the use of PVD is limited by the high cost due to the indispensable assemblies for high vacuum, which produces extra fabrication expense.

1.3.3.3 Chemical vapor deposition

In name only, chemical vapor deposition (CVD) involves chemical reactions and is performed based on vapor-phase processes. CVD offers a wide selection of elements of volatile precursors and deposited films are thus very versatile. For example, Si can be deposited via a plasma-enhanced CVD (PECVD) method, where SiH_4 is the precursor.[122] PH_3 and $B(CH_3)$ were used for n and p-type doping, respectively.[123] To synthesize GaAs thin films, trimethyl Ga, and AsH_3 serve as the precursors. Moreover, it is intriguing that sometimes CVD forms thin layer with nanostructures.[124] A dendritic structured Si-doped Fe_2O_3 thin layer has been synthesized by atmospheric pressure CVD (APCVD) with $Fe(CO)_5$ and tetraethoxysilane precursors. The distance of photo-excited holes diffusion to the surface was minimized by the nano-structuring and the charge separation is thus more efficient.[125]

Atomic layer deposition (ALD) is a more “advanced” type of CVD. A typical ALD process for Al_2O_3 is illustrated in Figure 1-8, in which $Al(CH_3)_3$ and water are the Al and O precursors, respectively. $Al(CH_3)_3$ is first pulsed in with enough time to fully react with the -OH group on the substrate, followed by purging to remove by-products and remained precursor molecules. Subsequently, the water is pulsed to the surface to form the first monolayer of oxide and followed by another purging process. Therefore, the thickness of the layer can be precisely controlled by this cyclic deposition process. Another primary advantage is the precise composition control. For example, a binary metal oxide, Al-doped ZnO (AZO), can be deposited by tailoring multiple super-cycles of Al and Zn oxides.[126] Moreover, ALD promises the good conformity of deposited films on high aspect ratio structures due to its self-saturating nature which allows the complete reaction at the entire surface.[127]

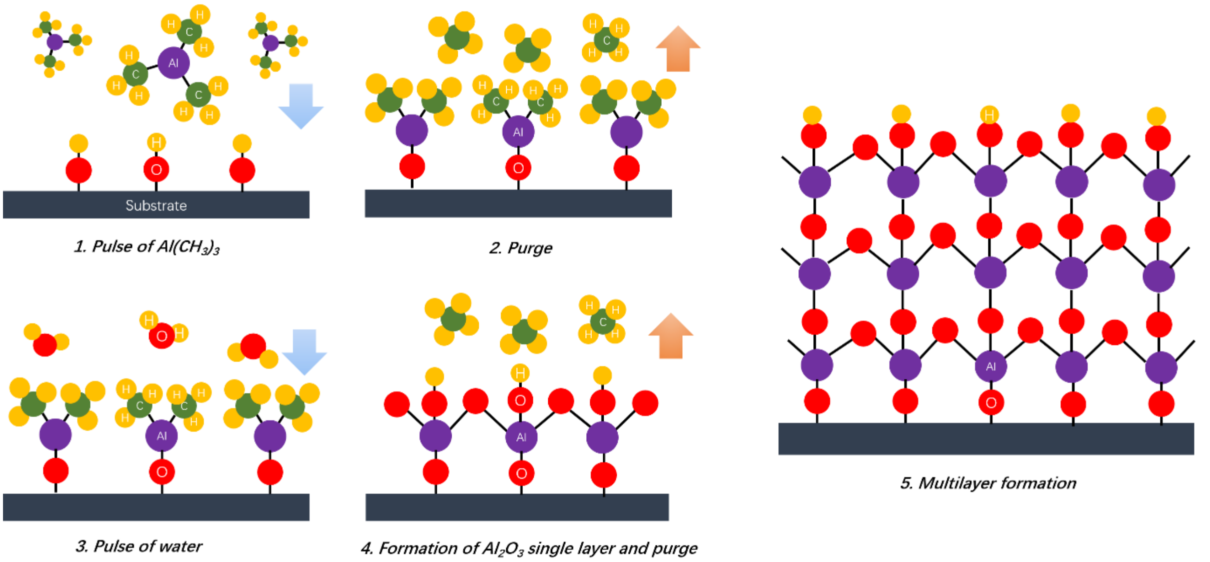

Figure 1-8 ALD cycles for Al_2O_3 growth by using tetrimethylaluminum ($Al(CH_3)_3$ or TMA) and water as precursors.

1.3.4 Typical examples of multilayer structured photoelectrodes

Based on above instructions of functional layers, Figure 1-9 illustrates the integrated

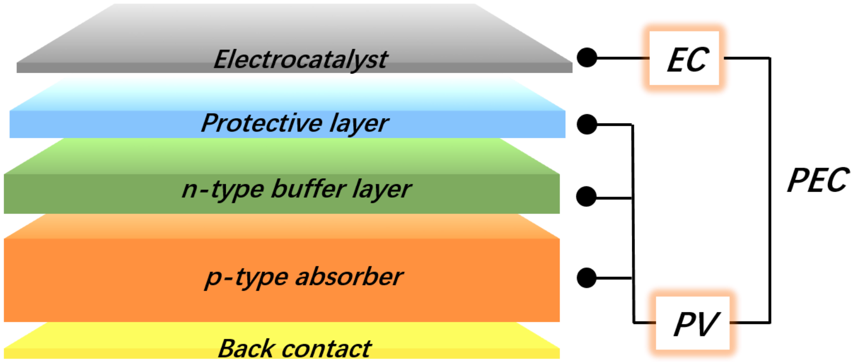

Figure 1-9 Schematic illustration of a water splitting photoelectrode with the multilayer configuration. An n-type buffer layer is used to form the p-n junction with the p-type semiconductor absorber. A protective layer is sometimes necessary to protect the underlying materials from contacting the electrolyte solution. An electrocatalyst is used to overcome the slow kinetics of the water splitting reaction.

multilayer structure of a promising H_2-evolving photocathode. The back contact is ohmic and enables the transfer of holes to the counter electrode to oxidize water. The back contact is often a metal layer such as Au and Mo. Because the substrate is usually glass, an adhesion layer (a Cr metallic layer) between Au and glass is required. Besides metals, Son *et. al*. reported a cost-effective CuO/NiO layer as the hole-selective back contact to avoid the using of noble metal Au.[128] The p-n junction layers then growth to harvest illumination and are responsible for the electron-hole pairs generation. The thickness of absorbers should be according to their absorption coefficient (or optical penetration depth) to fully utilize the incident energy. Sometimes nanostructured films must be considered for shortening the length that carriers must diffuse to reach the surface. Next, a protective layer is necessary if the semiconductor will photocorrode within the working potential range. Finally, an electrocatalyst is usually needed to improve the overpotential of the desired reaction. It is evident that the photocathode illustrated in Figure 1-9 has very similar multilayer structure as a solar cell. One difference is that a solar cell requires a top contact (metal grid) instead of electrocatalyst to collect the generated photocurrent. Another difference is the use of the antireflection layer instead of the protective layer for a solar cell.[129] Therefore, we can simplify the multilayer structure of the photocathode, dividing it into two parts that are in series. The first part is the PV part, including the back contact, the p-n junction and the protective layer. The PV part is responsible for charge generation and separation. The second part is the electrocatalyst, or so-called EC part, accelerating the chemical reaction on the surface. The PEC performance is thus simply considered as a “series combination” of the PV and EC performance, as presented in Figure 1-9. Three typical examples of photoelectrodes with the multilayer configuration are presented. Figure 1-10a is the p-GaP/TiO_2 /Pt photocathode reported by Vesborg group.[130] The n-type TiO_2 acts as the protective layer as well as the n-type partner for the p-n junction, and an onset potential of 0.35 V_{RHE} was achieved. Figure 1-10b illustrates the structure of the pn^+Si/Ti/TiO_x/MoS_x phtocathode, reported by Chorkendorff group.[131] The buried pn^+Si junction generated a V_{oc} of ~0.5 V. The protective Ti/TiO_x layer was synthesized by reactive sputtering, followed by the photo-electrodeposition of the MoS_x catalyst. Figure 1-10c is the Cu_2O-based Cu_2O/AZO/TiO_2/Pt photocathode, reported by Paracchino and co-workers.[112] P-Cu_2O, grown by electrodeposition onto Au-coated FTO slides, acts as the absorber. The

AZO and TiO_2 layer were deposited in sequence by ALD to form the p-n junction with Cu_2O and to protect the Cu_2O, respectively. With the electrodeposited Pt particles as the catalyst, a large photocurrent of -7.6 mA cm^{-2} was obtained in a pH 5 buffer solution.

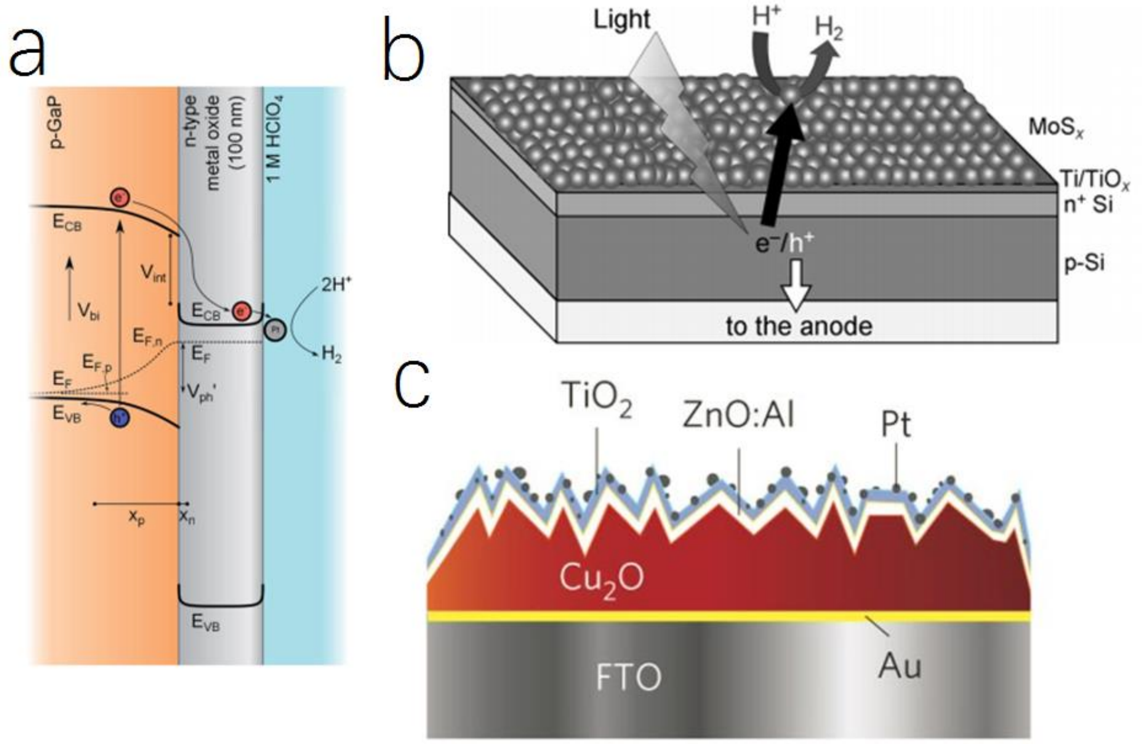

Figure 1-10 Schematic structure of several photocathodes: (a) p-GaP/TiO_2/Pt,[130] (b) pn$^+$Si/Ti/TiO_x/MoS_x[131] and Cu_2O/AZO/TiO_2/Pt[112].

1.4 PEC performance measurements

The general PEC test system is a 3-electrode set up, which consists of a working electrode (WE), a counter electrode (CE) and reference electrode (RE), as shown in Figure 1-11. A CE should be chemically inert to the electrolyte and electrically active to ensure the fast charge transfer between itself and the redox species in the electrolyte. Geometry of the CE also needs to be considered. The surface area of the CE should be large enough to pass the current derived from the WE at a reasonable potential. For characterizing of a photocathode WE which operates H_2 evolution, O_2 evolution occurs at the CE surface. In all PEC measurements mentioned in next chapters, a Pt wire are always used as the CE. The electrolyte used for PEC water splitting are aqueous solutions. A strong acidic solution such as 0.5 M H_2SO_4, will ensure the favorable kinetics as the electrolyte solution, as nearly all water reduction catalysts have lower overpotentials in strong acid solutions. For water oxidation, a strong alkaline solution such as 1 M KOH is often chosen, since most water oxidation catalysts are hydroxides or oxides that are stable and active under basic conditions.[132] In addition, buffer solutions, such as phosphate buffer, with neutral or moderate pHs have been increasingly used because they are more economic and environmentally friendly. However, some of the electrocatalyst (*e. g.* MoS_2) shows less catalytic activity in neutral pH.

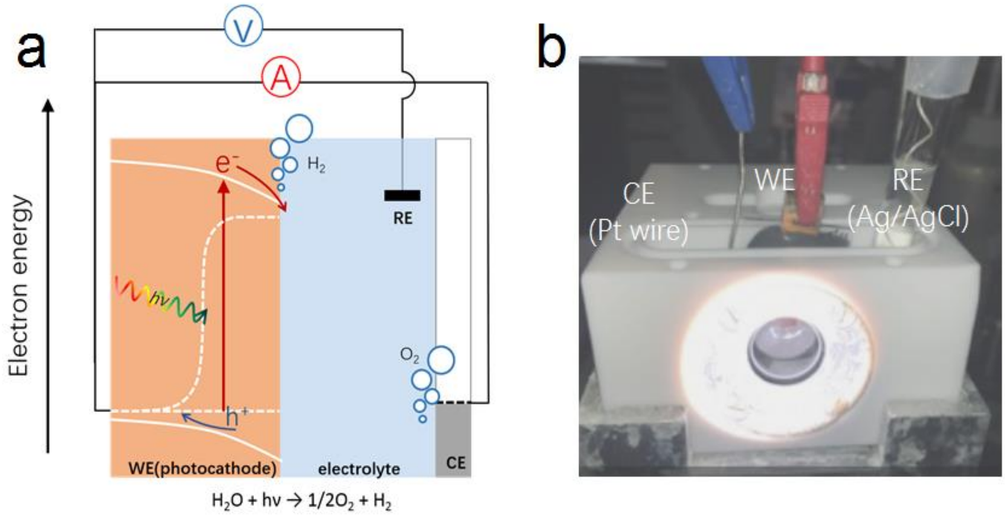

Figure 1-11 (a) Schematic illustration and (b) an optical picture of the traditional 3-electrode setup for PEC measurements under illumination.

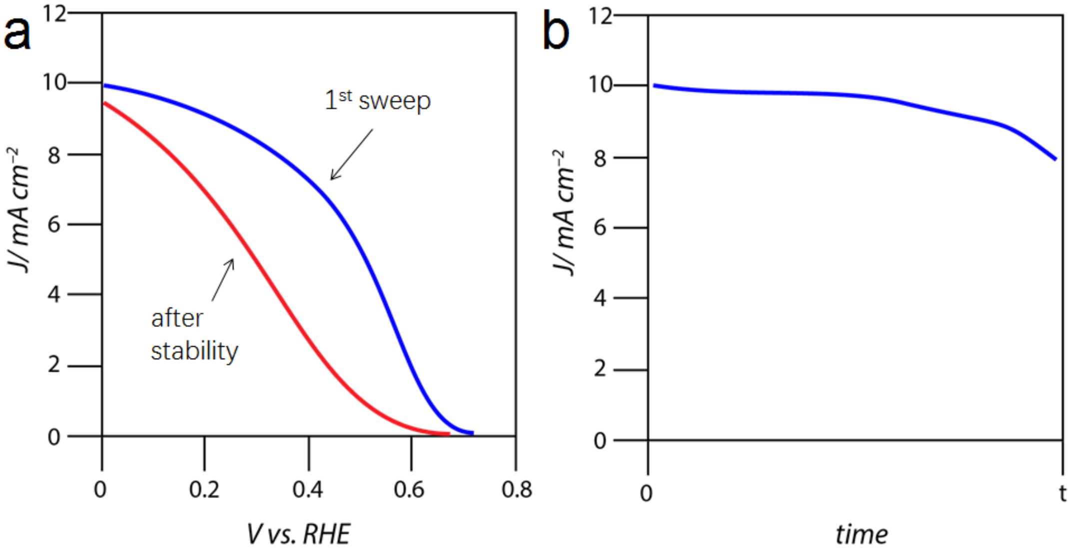

Figure 1-12 Typical (a) J-V curves and (b) J-t curve of a photoelectrode obtained from a three-electrode setup.

To characterize the PEC performance of a photoelectrode, the most common technique is to collect the photocurrent density (J) as a function of applied voltage bias under illumination, the so-called “J-V curve”. The J-V curves in Figure 1-12a are collected by linear sweep voltammetry (LSV) in the potential window of 0-0.8 V_{RHE}. At very positive potential, *e.g.* 0.8 V_{RHE}, the photo-excited minority carriers have insufficient energy to drive the water splitting reaction, thus the photocurrent at 0.8 V_{RHE} is zero. When the bias negatively moves until the thermodynamic requirement is satisfied, the minority carriers can operate the water splitting half reaction and photocurrent starts to raise. The photocurrent onset potential is a critical parameter, which implies the V_{oc} generated by the semiconductor absorber and the overpotential of the catalyst. Another important parameter is the fill factor (FF) of the J-V curve, which is actually used to evaluate a solar cell. But similarly, in the PEC J-V curve, the FF only represents the square-ness of the J-V curve. More squared curve indicates the less series resistance for charge carrier transfer in the tested sample.

The evaluation of the stability of a photoelectrode involves a long-term photo-electrolysis under a fixed bias (chronoamperometry), which has traditionally been 0 and 1.23 V_{RHE} for photocathodes and photoanodes, respectively (these values will be discussed in Section 6.2). The photocurrent values are recorded as a function of time, as shown in Figure 1-12b. In this way, the degradation of the photocurrent is visualized. In addition, the J-V curve after the chronoamperometry experiment is plotted for comparison with the initial one. As shown in Figure 1-12a, after the stability test, the J-V curve (red) exhibits cathodically shifted onset potential and decreased FF, suggesting the instability of the sample.

1.5 Motivations

Regardless, the electrochemical characterization with a 3-electrode configuration is very limited since the J-V curve only provides the overall PEC performance. The information read from the J-V curve is no more than the onset potential, photocurrent values and the FF. Deeper investigation is nearly impossible by one single J-V curve. For example, the exact V_{oc} value cannot be determined because the onset potential is also affected by the overpotential of the catalyst. The FF of the J-V curve represents the series resistance but detailed charge carrier process cannot be identified. In terms of the stability, the degradation mechanism is still ambiguous because the instability can be attributed to the catalyst deactivation or detachment, or from the underlying semiconductor degradation.

Therefore, we aim to develop a pure electrochemical methodology which can provide a deeper and systematic analysis of the PEC performance and stability. We expect this methodology enables to investigate following issues involved in a photoelectrode with complex structure:

(1) To deconvolute the property of the buried junction from the overall PEC performance and determine the actual V_{oc}.

(2) To identify the actual overpotential of the surface catalyst under operating conditions.

(3) To distinguish the catalyst degradation from the semiconductor degradation.

(4) To unveil the charge carrier processes hidden in a multilayered photoelectrode under operational condition.

2 The Dual-Working-Electrode Technique: pn^+Si/TiO_2 model system

2.1 Introduction of the Dual-Working-Electrode technique

Buried junction photoelectrodes can be modeled as a series combination of a p–n junction photoabsorber, a protective layer, and surface catalyst (pn/cat), as shown in Figure 1-9.[133,134] The photovoltage is decoupled from the semiconductor-electrolyte interface, and the increased band bending of the p-n junction can significantly enhance electron-hole pair separation.[135] The efficiency of a pn/cat photocathode is largely determined by the intrinsic properties of the buried p–n junction.[136] However, the semiconductor-catalyst and catalyst-electrolyte interfaces also play a critical role in the overall performance of the system. Issues such as charge transport in the protective layer, the nature of the semiconductor-catalyst contact (ohmic or Schottky-type), as well as the electrocatalytic activity at the catalyst-electrolyte interface are typically obscured within the standard current–voltage measurement data.[137,138] Therefore, we sought to develop an experimental technique that could not only evaluate the PEC performance but also simultaneously provide an understanding of these different interfaces during PEC operation.

The dual working electrode (DWE) technique was first reported in the 1970s. Nakato, Pinson and Wilson reported that n-GaP and n-TiO_2 photoanodes coated with thin gold films showed a photovoltaic effect (Figure 2-1a), representing early examples of *in situ* measurements of the surface potential.[139–141] Recently, the Boettcher group has used the DWE technique to study a photoanode-catalyst interface, as shown in Figure 2-1b and c.[56] It is of note that the second working electrode in all of the previous works has either been a transparent conducting oxide (TCO) or a thin metal film that covers the entire active area.[142,143] For systems that do not employ TCOs as part of the buried junction structure, it has thus far not been possible to carry out DWE studies without introducing a metallic film, which influences the measurement through partial light absorption and by affecting the catalyst binding to the photoelectrode surface. We have therefore developed a new architecture of the DWE technique that is compatible with standard buried junction photocathodes featuring a protective layer, which does not introduce extraneous materials at the semiconductor-electrolyte interface. With this method, one can diagnose a problem of the stability of the catalyst on the surface *versus* the stability of the photovoltaic output of the p–n junction. The stability of the photovoltaic output of emerging material systems is not often reported, and as will be shown in this manuscript, does indeed require consideration. The diagnosis of the point of failure in unmodified PEC devices under operation is critical for identification of targets to improve the system.

In this chapter, TiO_2-protected pn^+-Si junction photocathodes were chosen as the platform to develop this method, as the Si p–n junction is robust and stable. ALD TiO_2 is a common protective layer for water splitting photocathodes due to its favorable conduction band position for the hydrogen evolution reaction, optical transmittance for visible light, high stability over a wide range of electrolyte solutions and pH, and good conductivity. Moreover, the high doping density of ALD TiO_2 enables an ohmic (tunnel) contact to the contacting metal of the second working electrode (WE2), no matter the work function.[51,144] The top contact was made via a thin Au layer covered by epoxy, which was able to sense the surface potential of the photocathode under *operando* conditions, without directly contacting the electrolyte or HER catalyst, as shown in Figure 2-2. The hidden J-V curve of the buried p–n junction can then be extracted (independent from the surface kinetics) by measuring the difference in voltage

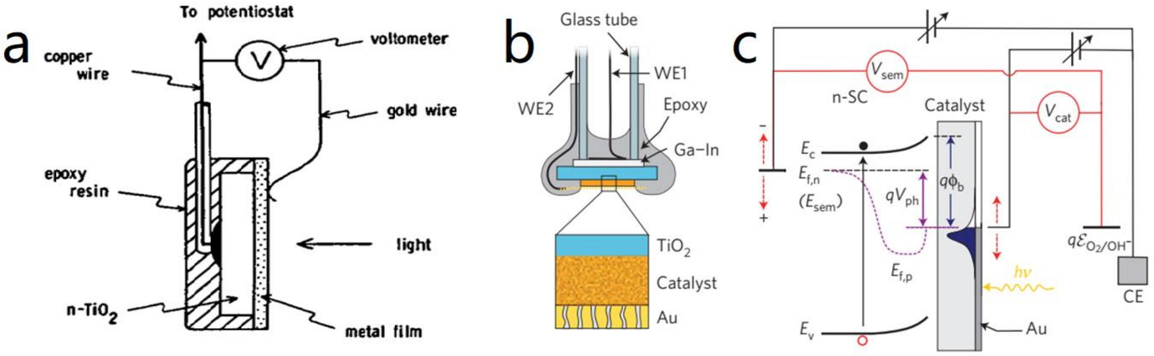

Figure 2-1 (a) Schematic diagram of an n-TiO_2 photoanode with a surface-potential sense electrode (metal film).[137] (b) The structure of the n-TiO_2/catalyst DWE. The second WE consists of a thin porous Au film deposited onto the catalyst surface. (c) Band-bending diagram of the PEC measurement setup, wherein the TiO_2 and catalyst potential (V_{sem} and V_{cat}, respectively) can be sensed or controlled.[168]

between the backside and the surface of the photocathode (ΔV) and plotting versus the water splitting current. By monitoring the evolution of the hidden J–V curve in the 3-electrode water splitting measurements, one can immediately diagnose whether the degradation in the performance of the photocathode derives from a problem with the catalyst or with the photovoltaic output of the p–n junction.

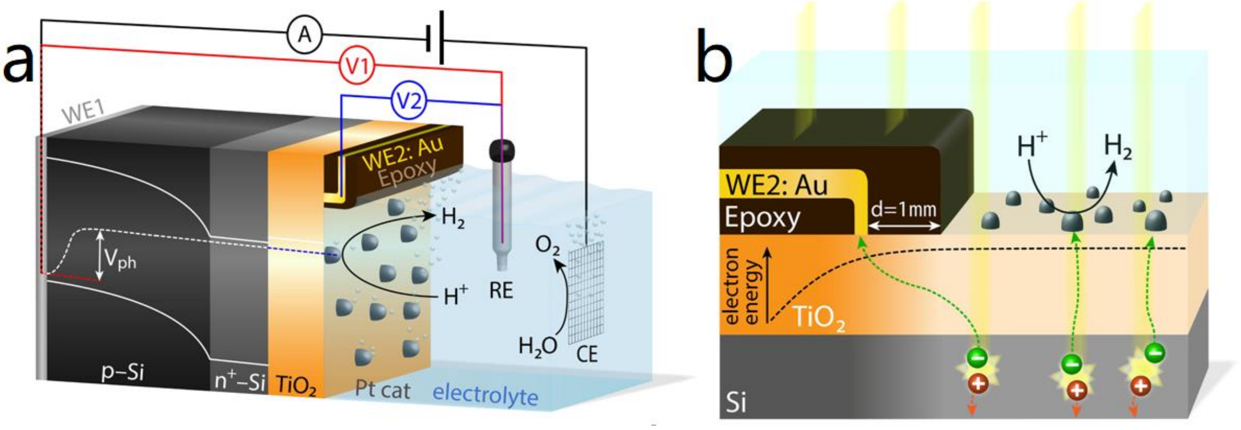

Figure 2-2 Schematic illustration of (a) the DWE configuration used during PEC measurements with a $pn^+Si/TiO_2/Pt$ photocathode and (b) the structure of the sensing electrode WE2, located a small distance (~1 mm) away from the illuminated area, separated by a thin coating of opaque epoxy (not to scale). For simplicity, the band bendings at the interfaces of the highly doped n^+-Si and TiO_2 have been omitted.

2.2 Fabrication the $pn^+Si/TiO_2/Pt$ photocathode DWE

2.2.1 Si wafer cleaning.

(111)-oriented Si wafers (thickness ~0.5 mm) used for DWE fabrication were purchased from PrimeWafers (Netherlands). The p-Si substrate was lightly boron-doped (~2×10^{16} cm^{-3}) and a 2 μm-thick n-type surface layer (polished) was doped with phosphorus (~2×10^{19} cm^{-3}). These wafers were cut into 2.5 × 1 cm^2 pieces and sonicated sequentially in acetone, ethanol and MilliQ water (18 MΩ) for 10 minutes each. Next, a two-step deep cleaning was accomplished by using a 5:1:1 mixture of $H_2O:NH_4OH:H_2O_2$, followed by a 5:1:1 mixture of $H_2O:HCl:H_2O_2$, both at 50 °C for 10 minutes, in order to completely remove organic and inorganic contaminants. The native oxide layer was etched away by dipping the wafer pieces in 2% HF for 30 s. The samples were then rinsed with deionized water and dried under a stream of nitrogen, and then placed immediately into the ALD chamber for deposition of TiO_2 onto the n^+-Si surface.

2.2.2 TiO_2 layer growth by ALD

TiO_2 on Si wafer was deposited by atomic layer deposition (ALD) using a Picosun R200 tool. The wafers were placed inside the ALD chamber, which was already heated to 120 °C. Tetrakis(dimethylamino)titanium (Sigma-Aldrich) and H_2O were used as the precursor for Ti and O, respectively. The Ti precursor was heated to 85 °C and a 1.6 s pulse was used (with software boost function), followed by a 6.0 s N_2 purge. H_2O was held at room temperature and a 0.1 s pulse was used, followed by a 6.0 s N_2 purge. To reach 100 nm of thickness for TiO_2, 1860 cycles were used. Measurement of the thickness of ALD-TiO_2 deposited on a piece of Si witness wafer (or on the Si wafer itself) was carried out by ellipsometry (alpha-SE, J.A. Woolam Co.), and fitted with a model for transparent films. The cross-sectional scanning electron microscopy (SEM) image (Figure 2-3, obtained with a Zeiss Supra 50 VP SEM) shows that the ALD-TiO_2 protective layer is conformably coated on the Si wafer.

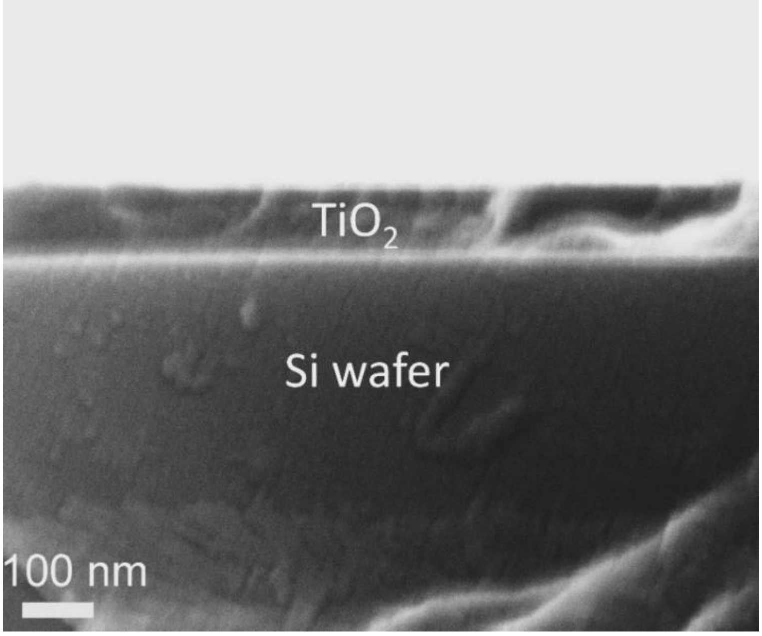

Figure 2-3 Cross-sectional SEM image of the pn^+-Si wafer with 100 nm-thick ALD-TiO_2 protective layer**.**

2.2.3 Fabrication of the back/front contact.

After ALD TiO_2 deposition, the working electrode 1 (WE1) contact was made to the back side of the p-type silicon by scratching the wafer with a diamond pen, applying Ga–In eutectic (Aldrich) and attaching copper foil (Aldrich). A layer of epoxy resin (Loctite Epoxide-resin EA 9461) was then used to cover and glue the electrode to a glass microscope slide, with a certain portion of the TiO_2 surface left uncovered for use as the electrochemical active area. For making the front contact, a 20 nm-thick Au layer was sputtered (Safematic CCU-010) onto the epoxy as well as a small part of the exposed TiO_2. A copper wire was connected to the Au layer with Ag paint (Ted Pella, Inc.) on top of the epoxy, as a connection for the second working electrode (WE2). Finally, the front contact was protected from the electrolyte by masking it with a second epoxy layer. Figure 2-4a shows an optical photograph and the structure scheme of an as-fabricated pn^+Si/TiO_2 DWE.

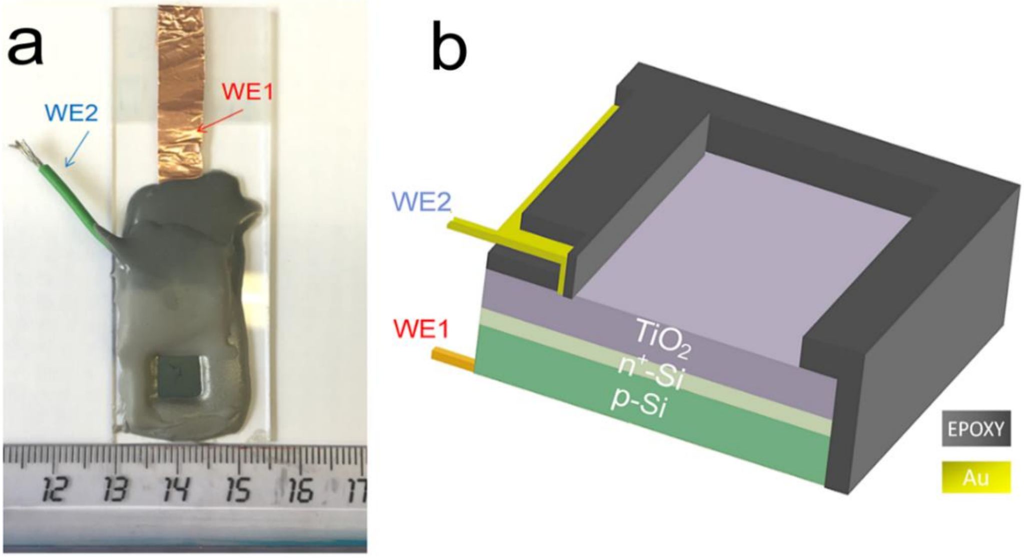

Figure 2-4 (a) Photograph and (b) structure scheme of a pn^+Si/TiO_2 DWE device. The 100 nm-thick ALD-TiO_2 overlayer gives a dark green color on the Si wafer due to optical interference effects. WE1 is a piece of Cu foil attached to the back side of the p-Si via Ga–In eutectic. WE2 is a conductive cable directly connected to the TiO_2 layer via a 20 nm-thick Au layer and Ag paint. The electrode is protected by epoxy. The ruler is in centimeters.

2.2.4 Pt catalyst deposition.

For some samples, Pt catalyst was deposited onto the as-prepared DWE via galvanostatic electrodeposition from a 1 mM H_2PtCl_6 aqueous solution, denoted as Pt(ed). A constant current of -0.85 μA cm^{-2} was applied to the back contact (WE1) for 15 min. For other samples, nominally 2 nm-thick Pt catalyst was deposited by sputter coating, denoted as Pt(sp)

2.3 J-V1 and J-ΔV curves

2.3.1 J-V curve measurements

Photoelectrochemical measurements were performed in a four-electrode configuration using a BioLogic SP-300 bipotentiostat. The reference electrode was Ag/AgCl (0.197 V vs. NHE) and a Pt wire served as the counter electrode. All electrode potentials were converted to RHE scale: at room temperature, $V_{RHE} = V_{NHE} + 0.059 \times pH = V_{Ag/AgCl} + 0.059 \times pH + 0.197$. Before the measurements, the electrolyte was sparged with N_2 for at least 10 min to remove dissolved oxygen. Simulated one sun illumination (100 mW cm^{-2}) was provided by a 150 W Xe-lamp with AM 1.5 G filter from LOT Oriel, and the intensity was calibrated with a standardized silicon diode from PV Measurements (USA). 0.5 M H_2SO_4 was used for Si-based DWE experiments. Linear sweep voltammograms (LSVs) were collected by sweeping the back contact potential (V1). The second working electrode was kept at open circuit to record the surface potential (V2) against the reference electrode.

2.3.2 Results and Discussion

After the Pt catalyst was electrodeposited onto the TiO_2 surface, the conventional current density-back contact potential (J-V1) curve of the $pn^+Si/TiO_2/Pt(ed)$ photocathode was obtained in 0.5 M H_2SO_4 with a linear sweep from positive to negative potential (Figure 2-5). Under one sun illumination, the $pn^+Si/TiO_2/Pt(ed)$ photocathode exhibits an onset potential for water reduction of ~0.5 V_{RHE}. As V1 becomes more negative, the photocurrent density increases and eventually saturates at 25 mA cm^{-2} at V1 = -0.2 V_{RHE}.

WE2 enables the *in situ* measurement of surface potential V2 during the sweep of V1. Figure 2-6 presents V2 and ΔV values as a function of V1 with and without illumination. When V1 is more positive than 0 V_{RHE}, V2 is similar to V1, thus ΔV is 0, indicating that no voltage difference is generated under dark conditions in this potential region. When V1 is scanned to more negative potentials than 0 V_{RHE}, V2 stays mainly unchanged with a value slightly more negative than 0 V_{RHE}, contributing to the tiny dark current. This region of very negative V1 corresponds to a reverse bias across the p–n Si homojunction, as is evident from the ΔV-V1 curve.

Under illumination, ΔV maintains a constant value of 475 mV until V1 reaches ~0.47 V_{RHE}. In this positive potential region, ΔV equals the output V_{oc} as there is no current flow across the interface. The potential where ΔV begins to shrink indicates the real onset potential of hydrogen production, which appears in this case at ~0.47 V_{RHE}. As the photocurrent increases while sweeping the potential negatively, ΔV decreases until a saturation photocurrent density is obtained, and then continues to shrink as the photocurrent remains saturated.

A hidden J-ΔV curve, analogous to the current-voltage characteristic of a PV cell, can then be extracted and is plotted in Figure 2-5. The V_{oc} and J_{sc} are 475 mV and 24.6 mA cm^{-2}, respectively. A significant loss of fill factor is observed when comparing the J-V1 and J-ΔV curves, which derives from the additional series resistances in a PEC cell *versus* a PV cell, namely the TiO_2/catalyst junction resistance, the overpotential of the catalyst required for driving a chemical reaction, and the solution resistance.[145] In essence, the J-ΔV curve shows the best possible fill factor that can be achieved by the J-V1 curve. In practice, a real PEC J-V1 curve will always have a smaller fill factor due to the catalyst overpotential as well as the

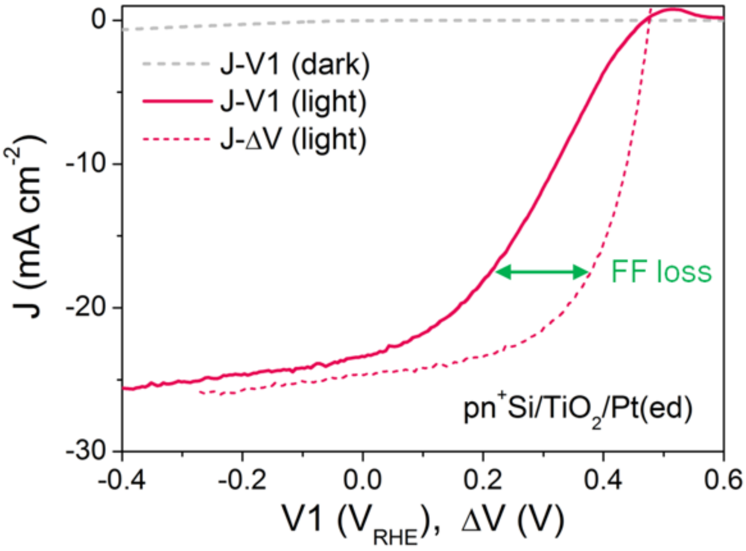

Figure 2-5 The J-V1 and J-ΔV curves of $pn^+Si/TiO_2/Pt(ed)$, collected by a LSV scan toward negative potential with a scan rate of 10 mV s^{-1} in 0.5 M H_2SO_4. ΔV = V1 - V2.

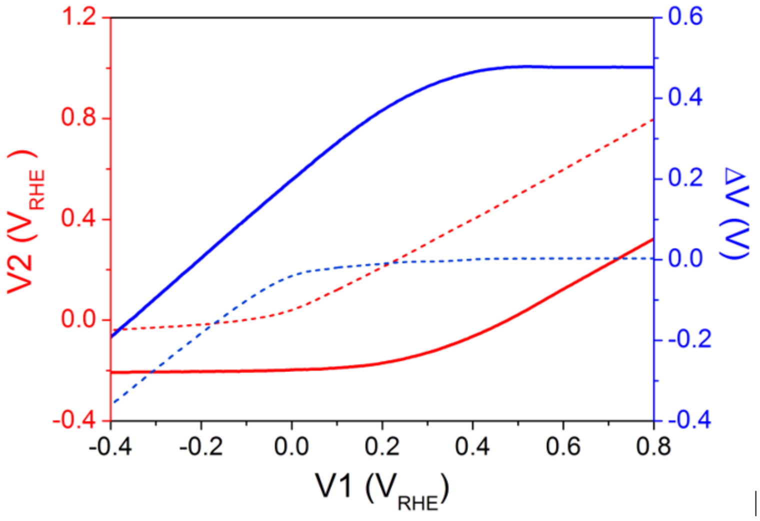

Figure 2-6 V2 and ΔV as a function as linearly swept V1 in dark (dashed) and light (solid) conditions.

series resistances mentioned above. Moreover, because the solution resistance does not change in the strongly acidic solution, the difference in fill factor between J-V1 and J-ΔV curves represents only a change in the electron transfer kinetics through the TiO_2/Pt/electrolyte interfaces.

2.4 Buried PV performance/interface energetics

2.4.1 V1 Stepwise measurements.

V1 stepwise measurements were performed by potential step chronoamperometry (CA). Each V1 potential step had a duration of 30 s. The stability tests of the samples were performed for 2 h with V1 held at 0 V_{RHE} under one sun illumination. During all measurements, the second working electrode was kept at open circuit to record the surface potential (V2) against the reference electrode.

2.4.2 Results and Discussion.

In order to more clearly visualize the effect of the surface potential on the current, a stepwise chronoamperometry measurement was carried out whereby the potential of V1 was stepped every 30 s and both V2 and the photocurrent were recorded (Figure 2-7). When V1 is positive of ~0.5 V_{RHE}, V2 remains at a constant distance (constant ΔV, see also Figure 2-6) and nearly

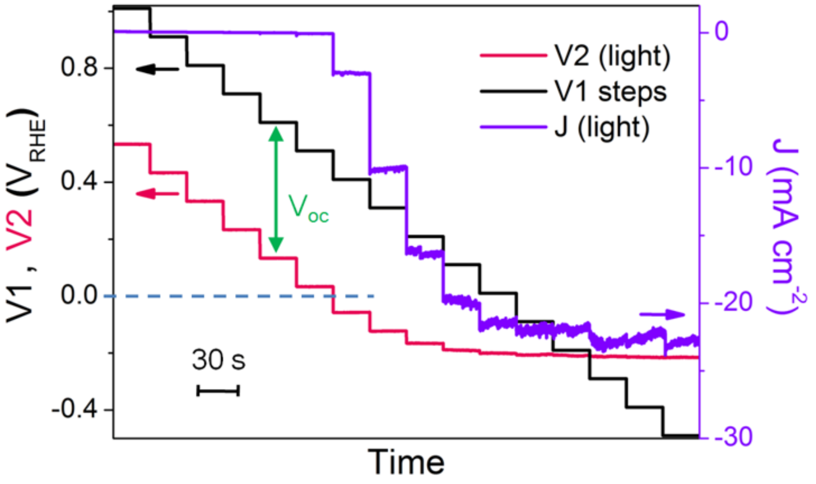

Figure 2-7 V2 and J values of pn$^+$Si/TiO$_2$/Pt(ed) with stepwise controlled V1 under illumination. Each V1 step lasts 30 s. Pt(ed) indicates that the Pt was deposited by electrodeposition.

zero photocurrent is recorded. Substantial cathodic photocurrents appear at V1 = 0.4 V_{RHE}, where V2 is more negative than 0 V_{RHE} (with ΔV now starting to shrink). After the onset potential, although V2 continues to move negatively with each step, ΔV shrinks further as the photocurrent increases. Ultimately, both V2 and the photocurrent become constant, even as V1 becomes more negative, eventually entering a reverse bias-type regime.

Figure 2-8 depicts band energy diagrams under several conditions of applied bias. A pn/cat electrode can be seen as a PV cell with one of the current collectors replaced by the electrolyte solution, where under certain conditions of V1, current can flow due to a chemical redox reaction at the surface. Schematically illustrated above, at very positive V1, such as 0.8 or 0.6 V_{RHE}, the electron quasi-fermi level (V2) is still much more positive than $E(H^+/H_2)$. Photoexcited electrons cannot be transferred into solution since the potential of the photoexcited electrons is still not high enough to drive proton reduction. In this region of V1 (before the onset of hydrogen generation), ΔV values remain constant and equal to V_{oc}. The flat band potential of TiO$_2$ itself is located near $E(H^+/H_2)$. As soon as V2 is slightly more negative than 0 V_{RHE}, hydrogen evolution is thermodynamically allowed, and electrons flow into the electrolyte by reducing protons into hydrogen gas. The V1 potential at this point is defined as the onset potential. As V1 becomes more negative, the ΔV value shrinks as the

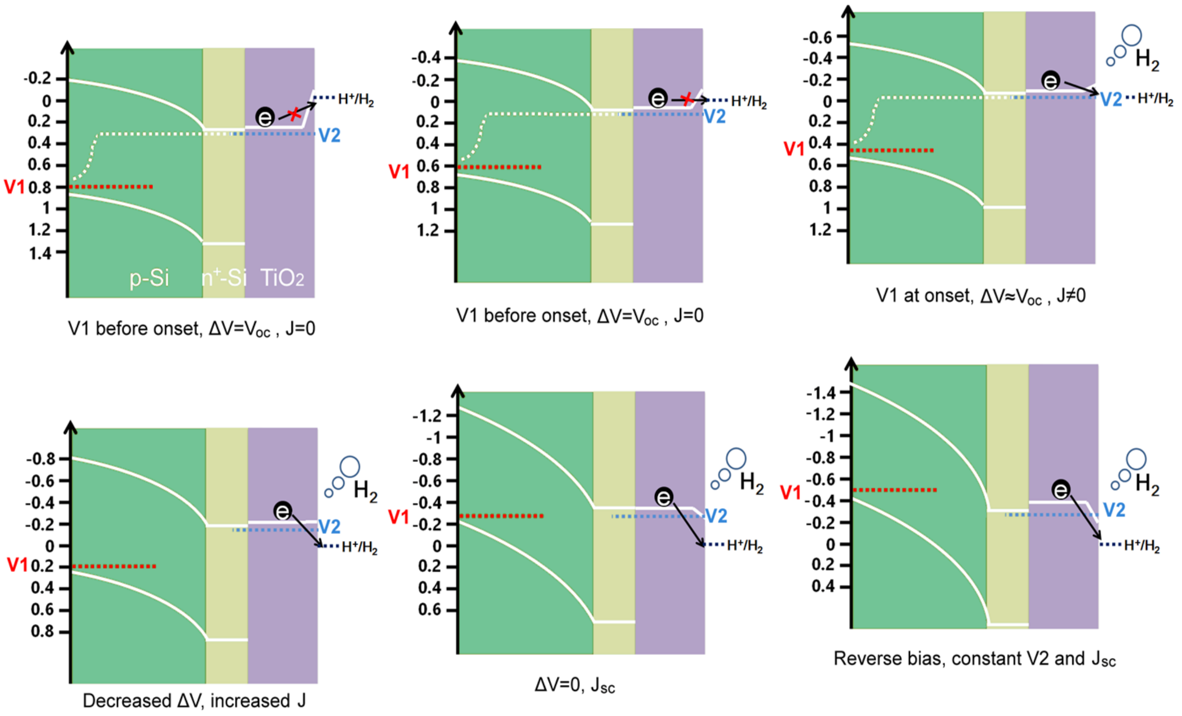

Figure 2-8 Schematic band energy diagrams of a pn$^+$Si/TiO_2 photocathode during a LSV scan by controlling V1 (under illumination). The potentials of the y-axis are V_{RHE}, and $E(H^+/H_2)$ is at 0 V_{RHE}. The Pt catalyst at the TiO_2 surface is not depicted in the schemes. Due to the high carrier doping density in both n$^+$-Si and TiO_2, the electron (quasi)-Fermi levels are located very close to the conduction band edge, and the space charge region widths are very short, ensuring that ohmic contacts are formed at both the n$^+$-Si /TiO_2 and TiO_2/Pt interfaces.

photocurrent corresponding to hydrogen generation increases. When V1 catches up to V2, ΔV is 0 and the buried p–n junction is at the short-circuit condition. Finally, as soon as the photocurrent becomes saturated due to the photon flux and recombination, V2 reaches a steady value independent of V1. The reverse bias across the p–n junction becomes stronger as V1 level continues to move to more negative potential.

2.5 Investigation of the electrocatalyst performance

2.5.1 The onset potential determination.

2.5.1.1 Faradaic efficiency measurements

The Faradaic efficiencies of the photocathodes were measured in a gas-tight three-compartment cell in a three-electrode configuration, with an Ag/AgCl reference electrode and a Pt wire counter electrode. The photocathodes were covered with epoxy to fix the active area to ~0.08 cm^2. The measurement was performed in the same electrolyte as in the PEC measurements (described above). The electrolyte was stirred and constantly sparged with Ar gas at a rate of 20 ml/min. The gas outlet from the cell was connected to a 450-GC Gas Chromatograph Bruker Daltonics GmbH for gas analysis. One LSV scan was first performed for choosing a suitable V1 potential for the Faradaic efficiency tests. During the measurement, the exposed area of the photocathode was illuminated with a white-light LED. The intensity of the light was calibrated to reach a similar photocurrent density as obtained under simulated one sun illumination, as described above.

2.5.1.2 Results and discussion

The V_{oc} appears at a more negative potential than the onset of photocurrent under certain sweeping conditions, as shown in Figure 2-9. This means that V2 is more positive than 0 V_{RHE}

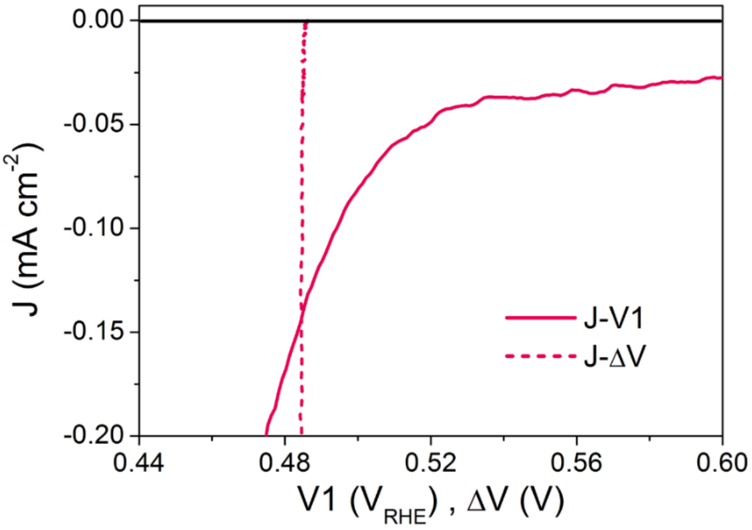

Figure 2-9 Zoom-in view of J-V1 (solid) and J-ΔV (dashed) curves of a pn$^+$Si/TiO$_2$/Pt(ed) photocathode with a scan rate of 10 mV s^{-1}.

while current is flowing. This V_{oc} loss is highly dependent on the distance between the Au contact and the illumination area, represented by d in Figure 2-10. For all the samples we measured, d is ~1 mm. When intentionally lengthening d, V_{oc} further decreases, yielding ~75 mV loss at d = 3 mm, as shown in Figure 2-10. From our experience with more than fifty samples, the offset between the measured V_{oc} and the apparent onset from the J-V1 curves is typically a few tens of mV with a platinum catalyst.

In order to confirm that these small photocurrents correspond to hydrogen evolution and not to e.g. proton intercalation, we carried out faradaic efficiency measurements (See Figure 2-11). Hydrogen was indeed observed at very small cathodic photocurrent densities, such as -0.08 mA cm^{-2}, at potentials more positive than we would expect from the J-ΔV analysis. This phenomenon likely arises from the fact that the slightly lower electron density than in the illuminated area and consequently an actually slightly reduced V_{oc} is detected compared to the illuminated area. Thus, the onset potential appears earlier than the V_{oc} in Figure2-9

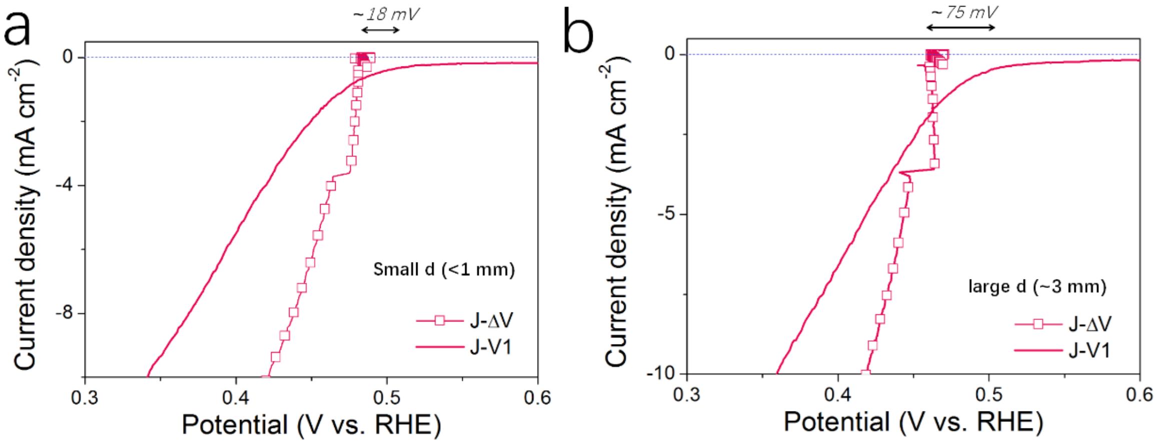

Figure 2-10 Zoom-in view of the offset between the V_{oc} and the onset potential of $pn^+Si/TiO_2/Pt$(ed) DWE with (a) small and (b) large lateral distance d values.

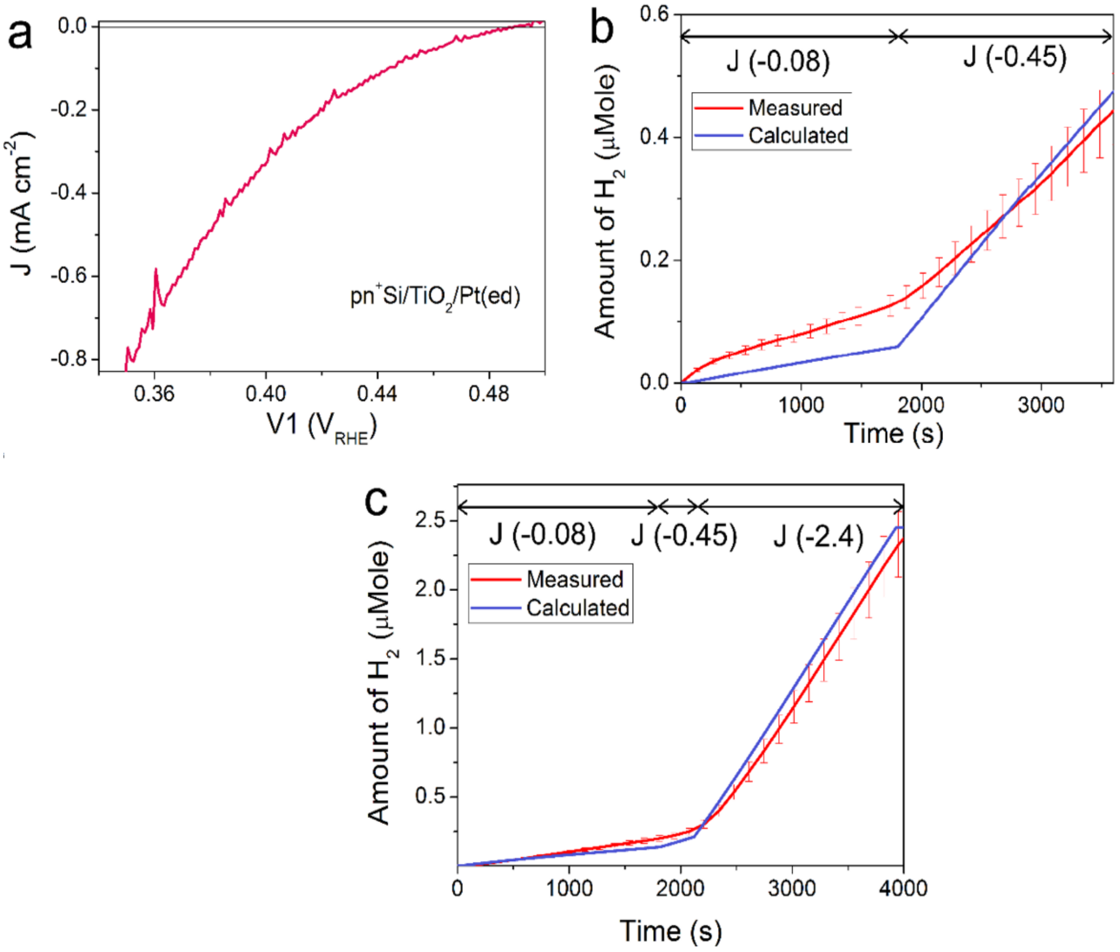

Figure 2-11 **(a)** J-V1 curve of a pn$^+$Si/TiO$_2$/Pt(ed) photocathode for faradaic efficiency measurements. (b)-(c) Comparison of calculated (by photocurrent) and measured H$_2$ (by GC) under current control, due to the variation of potential with illumination intensity. Note that when the photocurrents are very small, precise measurement of the amount of H$_2$ by GC is difficult, resulting in seemingly >100% faradaic efficiency for the very small values.

2.5.2 Comparison of Pt(ed) and Pt(sp) catalyst.

For the pn$^+$-Si photocathodes described above, the Pt catalyst was electrodeposited onto either the TiO$_2$ or Ti metal surface as nanoparticles with a size range of ~10-30 nm (Figure 2-12a). This non-continuous catalyst morphology may be unfavorable for efficient extraction of the surface electrons, resulting in a poor fill factor of the J-V1 curve.[146] Therefore, we investigated a nominally 2 nm-thick Pt film with nearly full coverage on the TiO$_2$ layer by

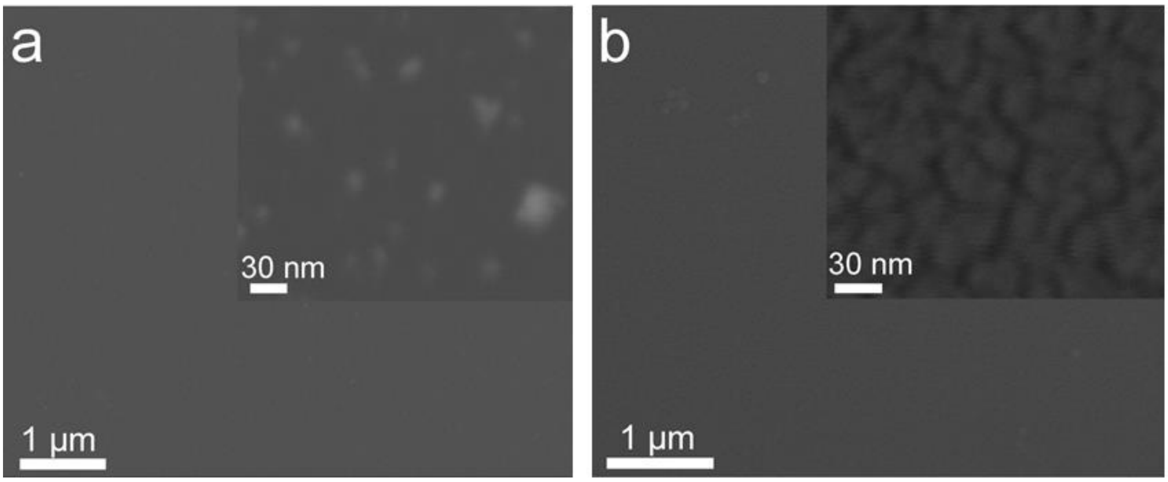

Figure 2-12 Plan view SEM images of (a) pn$^+$Si/TiO$_2$/pt(ed) and (b) pn$^+$Si/TiO$_2$/pt(sp) photocathode.

sputter coating (denoted pn$^+$Si/TiO$_2$/Pt(sp). The Pt deposited in this way makes the surface slightly rough (Figure 2-12b).

Figure 2-13a compares the J-V1 curves of pn$^+$Si/TiO$_2$/Pt(sp) and pn$^+$Si/TiO$_2$/Pt(ed) photocathodes under one sun illumination. Sputtered Pt exhibits a similar onset potential and improved fill factor, but much reduced photocurrent densities due to the optical transmission loss through the 2 nm-thick Pt film (Figure 2-14a). At similar saturation photocurrents the J-ΔV of pn$^+$Si/TiO$_2$/Pt(sp) is essentially identical with the pn$^+$Si/TiO$_2$/Pt(ed) (see the green and red dashed curves in Figure 13-b) while the J-V1 curve shows a clearly higher FF for the device with sputtered Pt. For better comparison between the sputtered and electrodeposited samples, we also measured the J-V1 curve of the pn$^+$Si/TiO$_2$/Pt(sp) at an increased light intensity to achieve a similar photocurrent density, plotted in green. The green curve exhibits an earlier onset potential despite having the same V_{oc} as the Pt(ed) curve, suggesting a better catalytic activity of sputtered Pt over electrodeposited Pt. Support for this hypothesis is shown by comparing their individual catalytic activities towards H_2 generation when deposited on FTO slides (Figure 2-14b). Additionally, pn$^+$Si/TiO$_2$/Pt(sp) always shows an enhancement in the fill

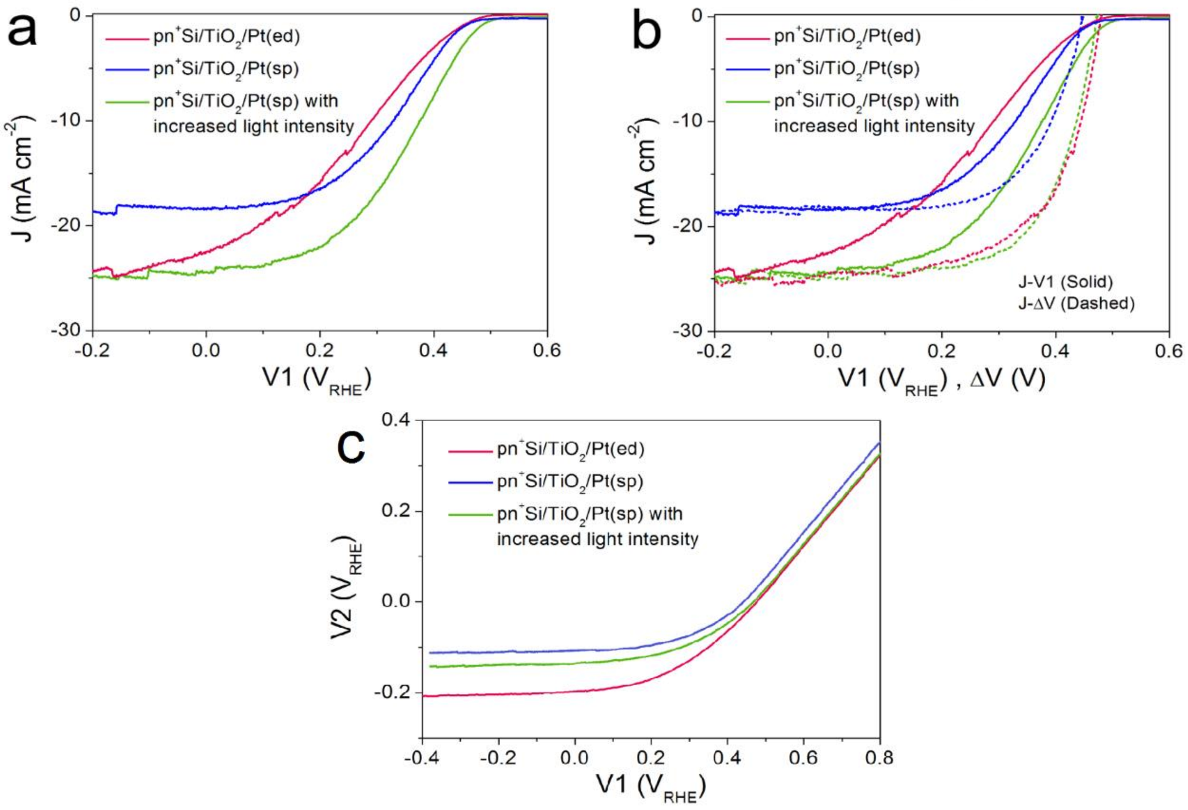

Figure 2-13 (a) Comparison of J-V1 curves between pn$^+$Si/TiO$_2$/Pt(ed) and pn$^+$Si/TiO$_2$/Pt(sp), collected by a LSV scan with a scan rate of 10 mV s^{-1} towards negative potential in 0.5 M H$_2$SO$_4$. (b) J-ΔV curves (dashed) of pn$^+$Si/TiO$_2$/Pt(ed) and pn$^+$Si/TiO$_2$/Pt(sp), combined with their J-V1 curves (solid). (c) V2-V1 curves of a pn$^+$Si/TiO$_2$/Pt(ed) and a pn$^+$Si/TiO$_2$/Pt(sp) photocathodes. All data are collected under illumination. For comparison, the performance of pn$^+$Si/TiO$_2$/Pt(sp) with similar photocurrent densities as pn$^+$Si/TiO$_2$/Pt(ed), by increasing the light intensity, is also displayed (green solid and dashed curves).

---

factor the in J-V1 curves, reflecting the smaller TiO$_2$/Pt/electrolyte interfacial resistance for the TiO$_2$/Pt(sp) as compared to the TiO$_2$/Pt(ed). In the case of a conformal Pt film, electron transfer is more probable as the catalyst surface area is increased, which is also indicated by the much more positive V2 value in pn$^+$Si/TiO$_2$/Pt(sp), shown in Figure 13c. For example, to reach the same saturation photocurrent, a ~130 mV overpotential is required for pn$^+$Si/TiO$_2$/Pt(sp) but ~200 mV for pn$^+$Si/TiO$_2$/Pt(ed). What we have already hypothesized by the performance of the different Pt on FTO is confirmed by the determination of the J-ΔV curves.

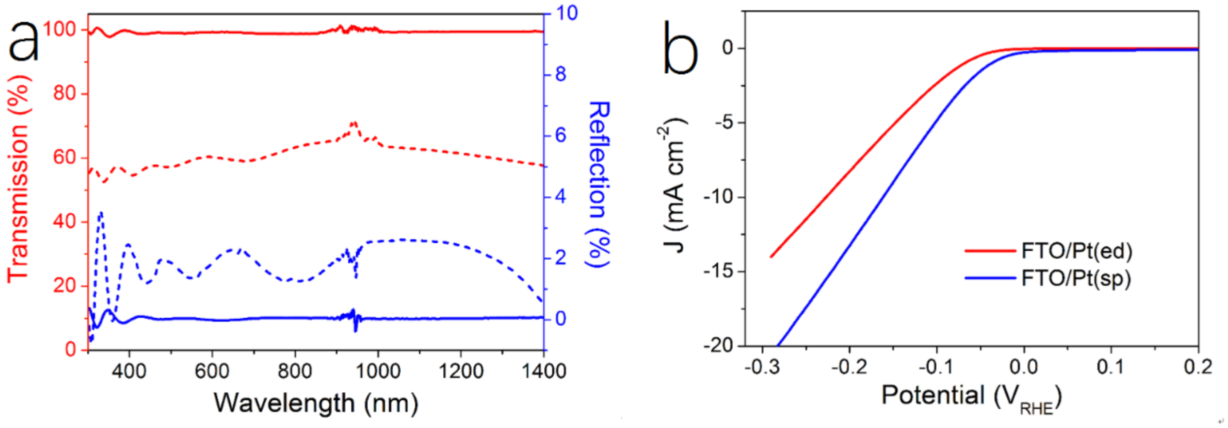

Figure 2-14 (a) Spectral transmission and reflectance curves for a Pt(ed) (solid) and Pt(sp) (dashed) deposited on FTO slides. (b) J-V curves of Pt(ed) and Pt(sp) deposited on FTO slides in 0.5 M H_2SO_4.

2.5.3 MoS_x catalyst.

2.5.3.1 MoSx catalyst deposition.

The MoS_2 catalyst were prepared via a hydrothermal synthesis approach.[147] In a typical synthesis, 1.452 g Na_2MoO_4•$2H_2O$ and 1.035 g H_2NCSNH_2 (mole ratio of Ni/Mo: 1:2) were dissolved in 35 mL deionized water. The mixture was ultrasounded for 30 mins and then transferred to a 50 mL autoclave for hydrothermal reaction at 200 °C for 24 h. After cooling to room temperature naturally, the products were collected by filtration, washed with distilled water and ethanol several times to remove the residue of reactants, and finally dried in vacuum at 80 °C. The solid MoS_2 was then dispersed in ethanol/water (1:1) solution to form a homogeneous suspension with a concentration of 20 mM. The MoS_2 suspension were applied to pn^+Si/TiO_2 electrodes surface by repeatedly dropping 20 μL. Each drop would be applied only after the previous drop was dried. In this study, 20, 40, 80, 100 μL MoS_2 suspension was coated onto the electrode via the drop-casting process, which was named as $pn^+Si/TiO_2/$ MoS_2(dc).

Amorphous MoS_x catalyst was photo-electrodeposited onto pn^+Si/TiO_2 electrodes by passing a constant current density of −50 μA cm^{-2} for 10 minute in a 5 mM $(NH_4)_2[MoS_4]$ solution (containing 0.5 M Na_2SO_4)[148] under one sun illumination. Then the electrode was rinsed with water to remove residue for future electrochemical characterization. This electrode was named as

$pn^+Si/TiO_2/$ MoS_2(ed).

2.5.3.2 Results and discussion

Figure 2-15a plots the J-V1 and J-ΔV curves of $pn^+Si/TiO_2/MoS_x$(ed) collected in 0.5 M H_2SO_4. Due to the large overpotential, a greater difference between the onset potential (0.3 V_{RHE}) and V_{oc} (0.45 V) is observed compared to that of photocathodes with Pt catalyst. Therefore, the real overpotential of MoS_x(ed) catalyst on the photocathode surface can be calculated as 150 mV, which is impossible to be determined by the traditional 3-electrode setup. Additionally, photocathodes with MoS_2(dc) by drop-casting were investigated with similar analysis. As shown in Figure 2-15b, the increase amount of MoS_2(dc) on the surface results in decreased saturated photocurrent densities but quite similar onset potentials. The photocurrent decreases from 26.1 to 14.5 mA cm^{-2} as the drop-casting solution volume increases from 20 to 100 µL. Note that without catalyst, the pure pn^+Si/TiO_2 photocathode exhibits a clearly later onset potential (~0.2 V_{RHE}). The increased amount of surface catalyst also leads to weaker light absorption, which is indicated by the decreased V_{oc} of J-V curves

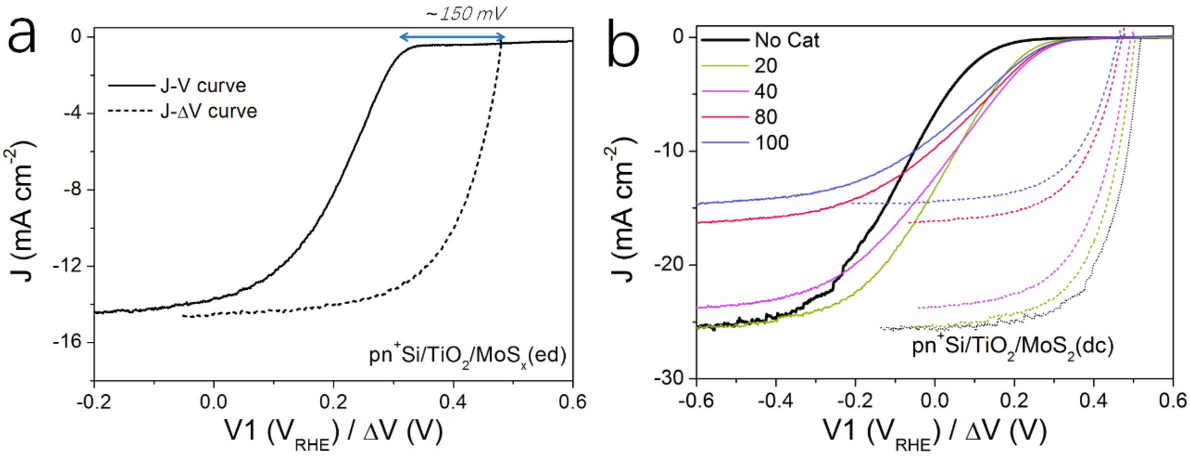

Figure 2-15 (a) J-V1 and J-ΔV curves of $pn^+Si/TiO_2/MoS_x$(ed) in 0.5 M H_2SO_4. (b) J-V1 and J-ΔV curves of $pn^+Si/TiO_2/MoS_2$(dc) loaded with 0, 20, 40, 80, 100 µL MoS_2 suspension.

2.6 Deep understanding of photocathode degradation mechanism

2.6.1 Introduction

A critical issue for photoelectrodes is the long-term stability. A standard procedure for assessing the stability is to carry out a chronoamperometry experiment under a static back contact potential and to compare the J-V1 behavior before and after the stability test. This type of analysis, however, is relatively limited because the underlying degradation mechanisms are inaccessible. The decrease in PEC performance can be due to several factors. Firstly, the H_2-evolving catalyst may be deactivated, poisoned or dislodged from the electrode surface. Secondly, the p–n junction may produce a reduced output V_{oc}, for example due to partial photocorrosion and increased recombination. These changes in the semiconductor material also result in lower photocurrent densities and fill factor. Here we use the DWE technique to distinguish the catalyst degradation and semiconductor degradation by comparing the J-ΔV curves before and after the stability test.

2.6.2 Stability measurements

The stability measurements of the samples were performed for 2 h with V1 held at 0 V_{RHE}, a typical value for these types of test in the literature,[149] under one sun illumination. During all measurements, the second working electrode was kept at open circuit to record the surface potential (V2) against the reference electrode

2.6.3 Results and discussion

Figure 2-16a shows the J-V1 and J-ΔV curves before and after the 2 h stability test. Compared with the initial J-V1 scan, the scan after the 2 h shows similar onset potential and slightly decreased saturation photocurrent, but a remarkably poorer fill factor. As the J-ΔV curves remain the same, it is immediately apparent that the problem relates to the catalyst and not to the buried junction. Figure 2-16b depicts how the surface potential V2 and photocurrent density change over time under a static back contact potential of 0 V_{RHE}. Over 2 h, the photocurrent density drops from ~23 to ~20 mA cm^{-2}, while V2 steadily shifts to more negative values. Figure 2-16c clearly shows the negative shift of the surface potential following the stability test, which indicates that higher overpotential is needed in order to achieve a similar

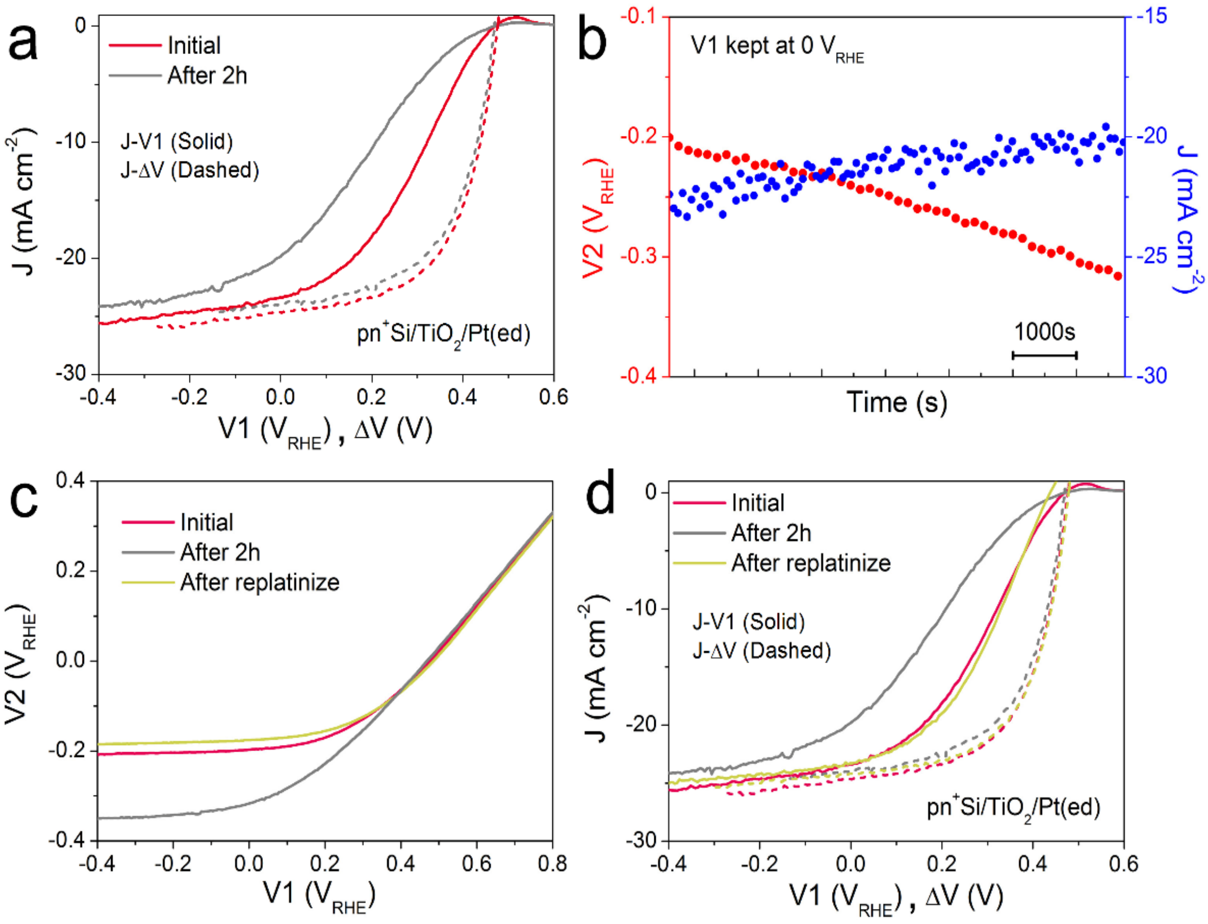

Figure 2-16 (a) J-V1 (solid) and J-ΔV curves (dashed) of pn$^+$Si/TiO$_2$/Pt(ed) before and after a 2 h stability test, collected by a LSV scan with a scan rate of 50 mV s^{-1} towards negative potential in 0.5 M H$_2$SO$_4$. (b) Changes in V2 and J during a 2 h stability test. V1 is held at 0 V$_{RHE}$. (c) V2-V1 curves of pn$^+$Si/TiO$_2$/Pt(ed) before and after a 2 h stability test, and after Pt catalyst re-deposition. (d) J-ΔV curves (dashed) of pn$^+$Si/TiO$_2$/Pt(ed) and the corresponding J-V1 curves (solid). All data are collected under simulated one sun illumination

current density. A poor contact between the surface and the catalyst (TiO$_2$/catalyst) as well as worsening kinetics at the catalyst/electrolyte interface (e.g. surface poisoning) will result in a higher overpotential for the catalytic interface.[150] Pt was then re-deposited onto the electrode surface (Figure 2-16d). Due to the fact that the fill factor is completely restored upon re-platinization, we can confirm that neither a degradation in the p–n junction of the silicon nor resistive losses through e.g. formation of a silicon oxide layer are responsible for the change in the J-V1 curve. The degradation likely results from desorption of the Pt nanoparticles, as has been previously observed for electrodeposited platinum on ALD TiO_2.[112]

When the ALD TiO_2 was replaced by a thin metallic Ti film, the Pt catalyst binding was much more robust over a 2 h stability measurement. As shown in Figure 2-17, V_{oc} of 448 mV and a J_{sc} of 23.5 mA cm^{-2} are obtained from the initial J-ΔV curve, slightly smaller than that of the $pn^+Si/TiO_2/Pt(ed)$ photocathode, which may be due to the antireflective property of TiO_2 layer.[151] The initial J-V1 curve exhibits a large fill factor loss relative to the J-ΔV curve. The similarities of the J-ΔV parameters of this sample with those of the ALD-protected sample indicates that the 100 nm-thick TiO_2 layer is highly conductive and does not contribute to a loss of fill factor in the J-V1 curve. After the 2 h stability test, the saturated photocurrent, V_{oc} and fill factor of the J-ΔV curves remained the same, showing that the pn^+-Si junction is well protected by the thin Ti layer during the 2 h test.

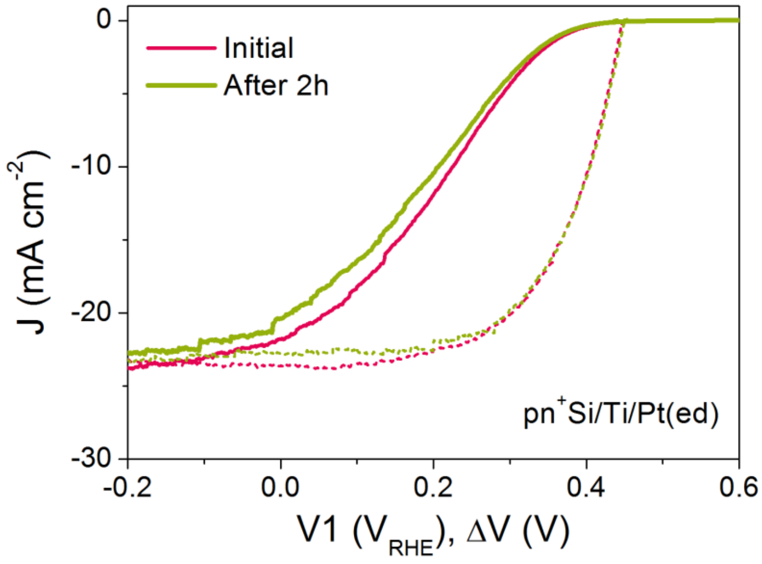

Figure 2-17 J-V1 (solid) and J-ΔV (dashed) curves of $pn^+Si/Ti/Pt(ed)$ before and after 2 h stability test.

2.6.4 Degradation mechanism of MoS_x catalyst

To investigate the degradation mechanism of the $pn^+Si/TiO_2/MoS_x(ed)$ photocathode, we applied several subsequent LSV scans. As shown in Figure 2-18, the FF gradually deteriorates from 1st can to 15th. After a post-1 h chronoamperometry, the FF becomes even worse. Note that the saturated photocurrent remains similar values which means the deposited $MoS_x(ed)$ had not detached from the electrode surface. After taking out and washing with water, the FF of the pn$^+$Si/TiO$_2$/MoS$_x$(ed) photocathode restores and the photocurrent density increases from 15.0 to 18.2 mA cm^{-2}. This suggests that during the stability measurements the inactive phase of MoS$_x$ formed which can be removed by rinsing. The underlying TiO$_2$/MoS$_x$ interface did not change despite the fact that MoS$_x$ became less effective at catalyzing H$_2$ evolution.

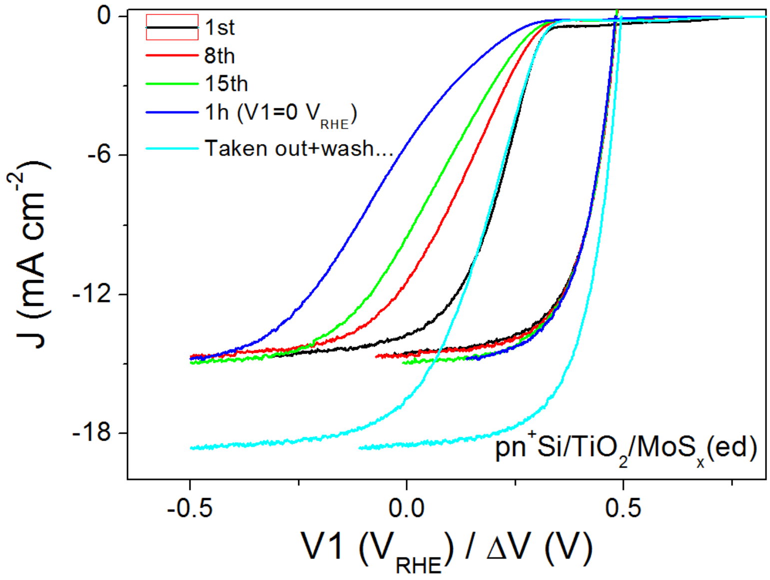

Figure 2-18 J-V1 and J-ΔV curves of pn$^+$Si/TiO$_2$/MoS$_x$(ed).

2.7 Conclusions

In summary, we have developed a new configuration of the DWE technique that is able to probe the surface potential of a water splitting photocathode under operation without interfering in the actual charge transfer processes at the different interfaces. This technique has been demonstrated as a universal method to systematically investigate independently the photovoltaic and electrocatalytic properties of catalyst-modified buried junction photocathodes. A pn$^+$Si/TiO$_2$/Pt(ed) photocathode was first fabricated as a platform to model the DWE system. By means of surface potential measurements, the intrinsic properties of the buried p–n junction were studied, and the hidden J–V curve of a photovoltaic cell was extracted.

Additionally, the fill factor loss between J-V1 and J-ΔV curves was identified as a parameter that characterizes the TiO$_2$/Pt/electrolyte interface, where the morphology of the catalyst plays an important role. For example, the pn$^+$Si/TiO$_2$/Pt(sp) showed better FF than the pn$^+$Si/TiO$_2$/Pt(ed) photocathode because the Pt(sp) film has a larger coverage and better contact with TiO_2 than the Pt(ed) particles. Another H_2-evolving catalyst MoS_x, applied by electrodeposition and drop-casting, was studied by the DWE technique. The real overpotential was determined as 150 mV, in line with literature values.

Finally, the PEC performance degradation mechanism was investigated and discussed. We have demonstrated that the stability of underlying p–n junctions in buried junction photocathodes can be characterized in operando. For the pn^+Si/TiO_2/Pt(ed), the underlying pn Si junction is stable, confirmed by the nearly unchanged J-ΔV curves before and after the stability test. Pt catalyst was detached from the surface and this is the main reason for the FF loss in J-V1 curves. Regarding to MoS_x(ed), the deactivation occurred during the stability test and the inactive phase could be removed by rinsing.

3 Application of DWE on emerging photocathode systems

3.1 $Cu_2O/Ga_2O_3/TiO_2/Pt$ DWE

3.1.1 Introduction

Chapter 2 introduced the DWE technique with a model $pn^+Si/TiO_2/Pt$ photocathode, with which we could gain a deeper insight into the PEC process and the photocathode stability. Next, we applied this technique to the emerging material ALD TiO_2-protected Cu_2O to demonstrate the generality of the technique and to probe a potential instability of the photovoltaic output of these materials.[32,152] An n-type Ga_2O_3 was used as a buffer layer between the Cu_2O and TiO_2 overlayer because this interlayer ensures a positively shifted onset potential, compared to that of n-Al:ZnO (AZO) (Figure 3-1).[153,154]

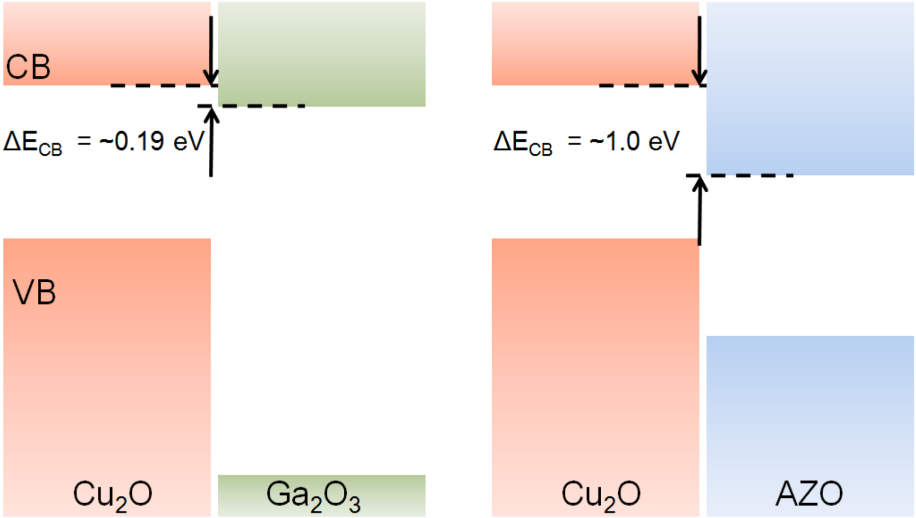

Figure 3-1 Schematic band alignment of the Cu_2O/Ga_2O_3 and Cu_2O/AZO heterojunctions. Cu_2O/Ga_2O_3 exhibits a small conduction band offset (ΔE_{CB}) of ~0.19 eV. This value is much smaller than the counterpart of Cu_2O/AZO (~1 eV). Therefore, ccompared with AZO, Ga_2O_3 shows an improved conduction-band offset with Cu_2O, enabling a larger photovoltage and the ability to shift the onset potential positively.

3.1.1 Fabrication of $Cu_2O/Ga_2O_3/TiO_2/Pt$ DWE

3.1.1.1 Cu_2O plate preparation

A Cu_2O plate was prepared via oxidation of a high purity Cu plate (99.9999%), using a method adapted from the literature.[155] The Cu plate (0.1 mm thick) was first cut into small pieces (~2 × 2 cm^2) and heated from room temperature to 1050 °C (ramp: 17 ℃ per min) and kept at this temperature for 1 h under Ar flow (1 L min^{-1}). Next, air was introduced into the furnace and held for 3 h. The gas environment was then switched back to Ar for another 3 h of

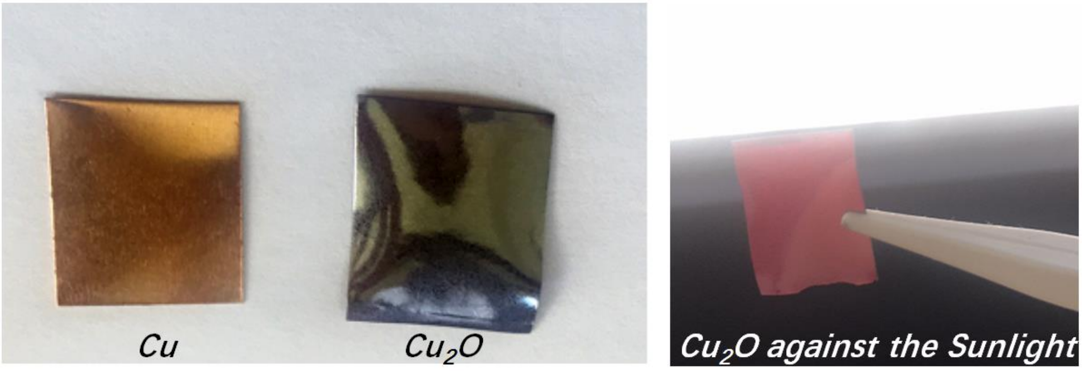

Figure 3-2 Optical pictures of Cu and the as-prepared Cu_2O foils.

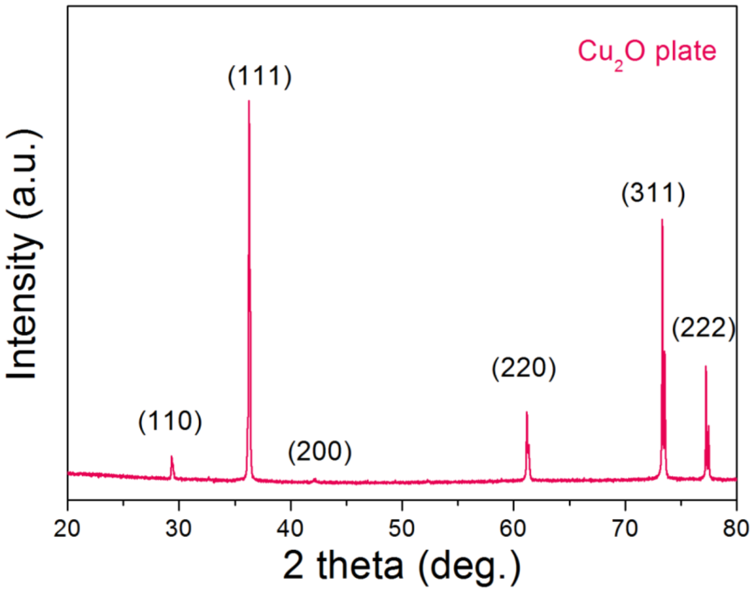

Figure 3-3 The XRD pattern of the synthesized Cu_2O plate. Identification of the diffraction peaks is referred to the standard Cu_2O data (JCPDS No. 05–0667).

annealing at the same temperature. After cooling down to room-temperature under Ar, the as-prepared Cu_2O plate was dark red when held up to the light, as shown in Figure 3-2. The polycrystalline structure of the Cu_2O plate is revealed by the X-ray diffraction (XRD) pattern (Figure 3-3), using a Rigaku Smartlab diffractometer with Cu Kα radiation.

3.1.1.2 Ga_2O_3/TiO_2 overlayer growth by ALD

For the Ga_2O_3 layer, bis(μ-dimethylamino)tetrakis-(dimethylamino)digallium (STREM, 98%) was used as Ga precursor. The ALD chamber temperature was kept at 160 °C during deposition. The Ga precursor was held at 150 °C and a 2.5 s pulse was used (with software boost function), followed by a 7.0 s N_2 purge. The H_2O was held at room temperature, and a 0.1 s pulse was used, followed by a 4.0 s N_2 purge time. To deposit a 20 nm-thick Ga_2O_3 thin film, 250 cycles were used. In order to avoid ALD growth on the back side of the sample (potentially leading to shunting problems), teflon tape was used to cover the back side of the Cu_2O plates during the ALD process. TiO_2 deposition was using the same recipe described in 2.2.2. Figure 3-4 the Cu_2O/Ga_2O_3/TiO_2 multilayered structure.

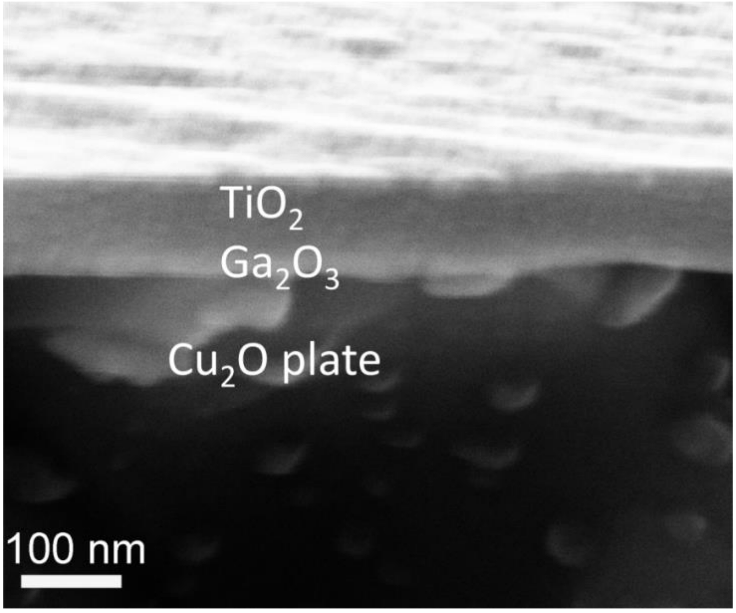

Figure 3-2 Cross-sectional SEM image of Cu_2O/Ga_2O_3/TiO_2 electrode. The thickness of Ga_2O_3 and TiO_2 are 20 nm and 100 nm, respectively.

3.1.1.3 Fabrication of the back and front contact

After the deposition of the Ga_2O_3-TiO_2 overlayer, a 100 nm-thick Au layer was then sputtered onto the back side of the Cu_2O plate (the front side was protected with teflon tape), followed by connecting an Ag wire with Ag paint as WE1. Epoxy resin was then used to cover the whole back side of the electrode to provide protection and enhance the stiffness of the Cu_2O plate. In a similar fashion as for the silicon photocathodes described previously, a second working electrode was introduced to probe the surface potential V2, prior to deposition of the Pt catalyst by sputtering. WE2 was connected to the ALD-TiO_2 surface using the same method as for the Si-based DWE, described in 2.2.3. The Pt catalyst was sputtered onto the electrode surface using a same procedure as described in 2.2.4. Figure 3-5 schematically depicts the multilayer structure of the Cu_2O/Ga_2O_3/TiO_2 photocathode.

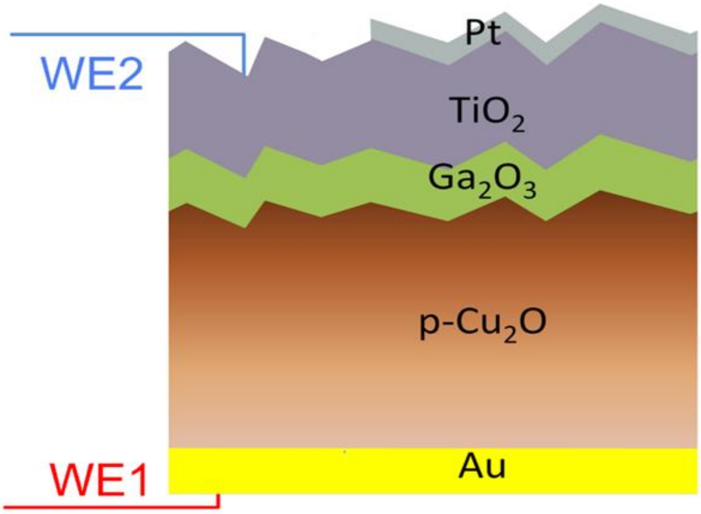

Figure 3-3 Schematic structure of a Cu_2O/Ga_2O_3/TiO_2/Pt(sp) DWE.

3.1.2 Results and Discussion

PEC measurements were performed in a 0.1 M pH 5 phosphate solution (containing 0.5 M Na_2SO_4). Figure 3-6 displays the J-V1 and J-ΔV curves. A positive onset potential of ~0.9 V_{RHE} is observed in the J-V1 curve, and at V1 = 0 V_{RHE}, the photocurrent density is 3.9 mA cm^{-2}. The onset potential is much more positive than that from both Cu_2O/ZnO and Cu_2O/AZO photocathodes, reflecting the larger photovoltage generated by the Cu_2O/Ga_2O_3 junction. In the case of the J-ΔV curve, the V_{oc}, J_{sc} and fill factor are 836 mV, 4.0 mA cm^{-2} and 36.1%, respectively. Compared with reported Cu_2O/Ga_2O_3 solar cells in the literature, the V_{oc} and fill factor values are comparable, but the J_{sc} is lower due to light absorption by the Pt catalyst.[154,156] Still, resistance at the TiO_2/Pt/electrolyte interfaces contribute to the fill factor loss between the J-V1 and J-ΔV curves. The fill factor loss is not very significant. As the J-ΔV curve mirrors the J-V1 curve, it is clear that that the photovoltaic output of the buried Cu_2O/Ga_2O_3 junction is responsible for the shape of the J-V1 curve of the photocathode, and not the catalytic activity of the Pt catalyst. When using an electrodeposited Pt catalyst, the PEC system exhibits a lower fill factor, indicating that the TiO_2/Pt/electrolyte resistance indeed can also limit J-V1 performance, as shown in Figure 3-7.

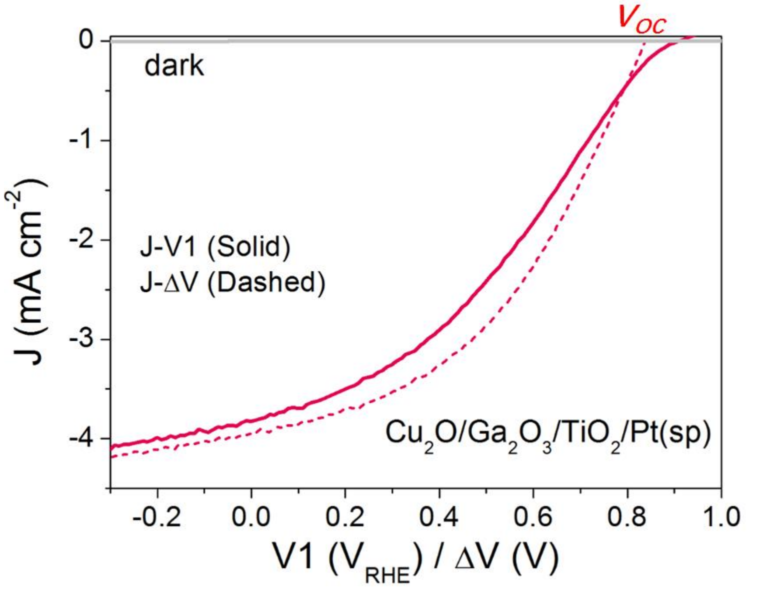

Figure 3-4 J-ΔV curves (dashed) of $Cu_2O/Ga_2O_3/TiO_2$/Pt(sp) in a pH 5 electrolyte solution.

We further carried out a stepwise test on the photocathode under illumination. Results are

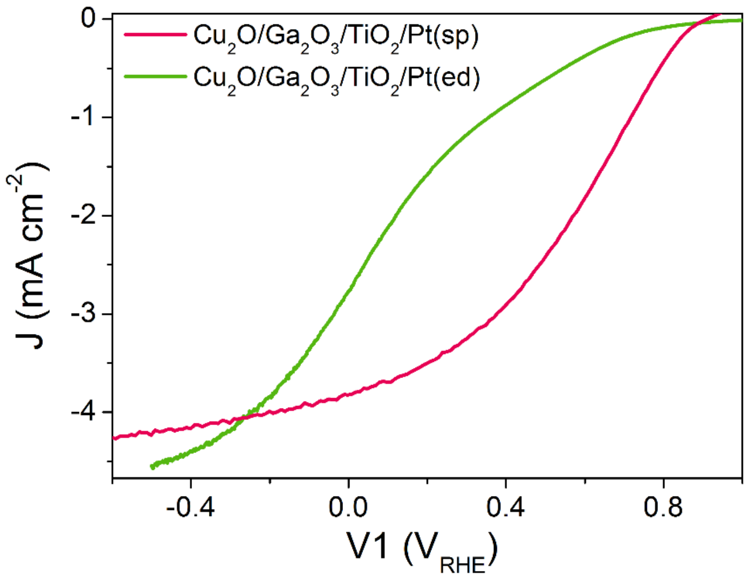

Figure 3-5 J-V1 curves of a $Cu_2O/Ga_2O_3/TiO_2/Pt$(sp) and a $Cu_2O/Ga_2O_3/TiO_2/Pt$(ed) photocathodes (under one sun illumination).

provided in Figure 3-8 When V1 is more positive than 0.8 V_{RHE}, V2 is more positive than 0 V_{RHE} but accompanied by a small photocurrent density. In this region, ΔV is determined as ~800 mV. When V1 is more negative than 0.8 V_{RHE}, the photocurrent increases and ΔV shrinks dramatically, following the same trend as with the pn^+/Si photocathode. Eventually the photocurrent reaches a plateau and V2 likewise saturates, even as the V1 potential moves steadily more negative.

As seen also with the Si-based photocathode, the onset potential occurs ~40 mV earlier than

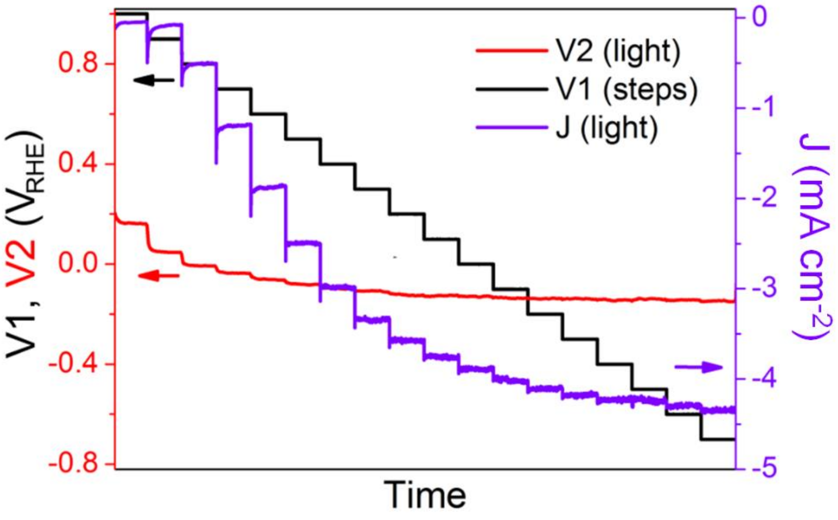

Figure 3-6 V2 and J values of the $Cu_2O/Ga_2O_3/TiO_2/Pt$(sp) photocathode under stepwise controlled V1 under one sun illumination. Each V1 step lasts 30 s

the V_{oc} (Figure 3-6). Again, this small offset is due to the remote configuration of WE2. Faradaic efficiency measurements were carried out at very small photocurrent densities, (e.g. -0.024 mA cm^{-2}), which confirmed that these currents do indeed correspond to hydrogen evolution.

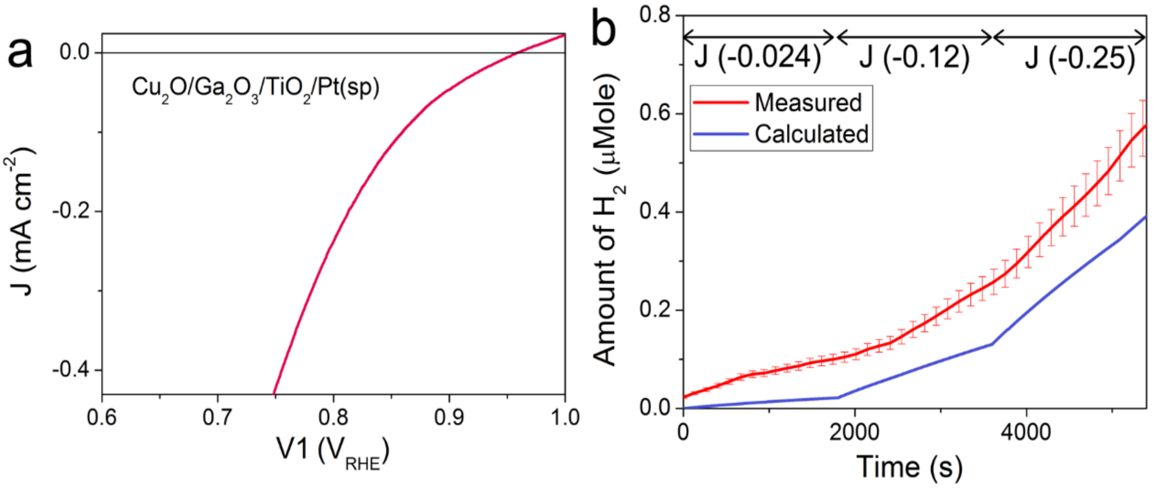

Figure 3-7 J-V1 curve of a $Cu_2O/Ga_2O_3/TiO_2/Pt(sp)$ photocathode for faradaic efficiency measurements. (b) Comparison of calculated (by photocurrent) and measured (by GC) H_2 under current control, due to the variation of potential with illumination intensity. Note that when the photocurrents are very small, precise measurement of the amount of H_2 by GC is difficult, resulting in seemingly >100% faradaic efficiency for the very small values.

3.1.3 Instability of the Cu_2O/Ga_2O_3 junction.

To study the stability of the $Cu_2O/Ga_2O_3/TiO_2/Pt(sp)$ photocathode, a 2 h chronoamperometric measurement was performed under illumination at V1 = 0 V_{RHE}. Fig. 4b shows the comparison of the J-V1 curves before and after a 2 h stability test. The onset potential shows a negative shift of nearly 120 mV, although the photocurrent density remains similar. Figure 3-10 compares the initial J-ΔV curve and the one after the 2 h stability test. An obvious decrease in V_{oc} is evident, from 836 mV to 743 mV, while the J_{sc} shows a slight increase from 4.0 to 4.1 mA cm^{-2}. In contrast to the pn^+-Si photocathode, the Cu_2O/Ga_2O_3 photocathode shows a degradation of the photovoltaic output of the underlying buried junction. For the Si system, J-ΔV remained constant while the J-V1 changed (Figure 2-16a). For the Cu_2O/Ga_2O_3 case, J-ΔV has changed while J-V1 remains similar (retains a similar photocurrent and fill

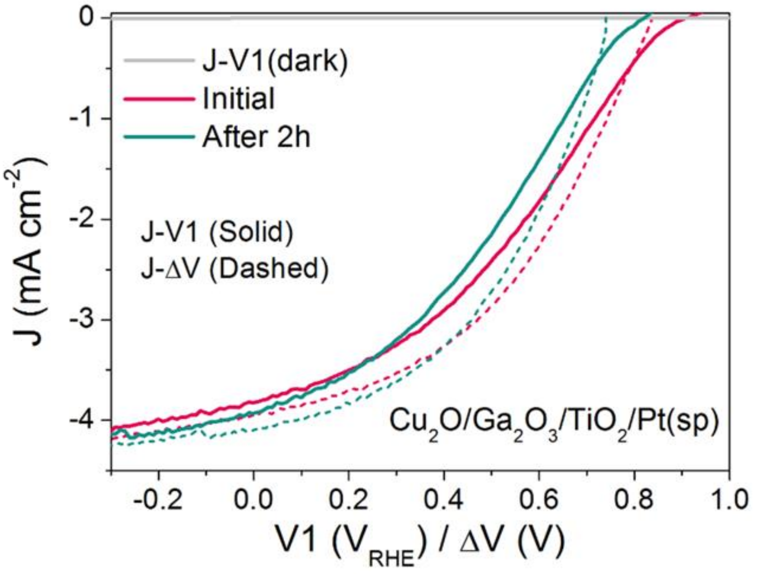

Figure 3-8 J-V1 and J-ΔV curves (dashed) of $Cu_2O/Ga_2O_3/TiO_2$/Pt(sp) before and after 2 h stability test, overlaid with the corresponding J-V1 curves (solid)

factor). In order to determine the origin of the degraded photovoltage, a solid-state measurement was carried out using the DWE photocathode in a 2-electrode configuration, directly obtaining photovoltaic J-V curves. Figure 3-11 shows the J-V characteristics of the $Cu_2O/Ga_2O_3/TiO_2$ DWE device before and after a stability measurement that was carried out

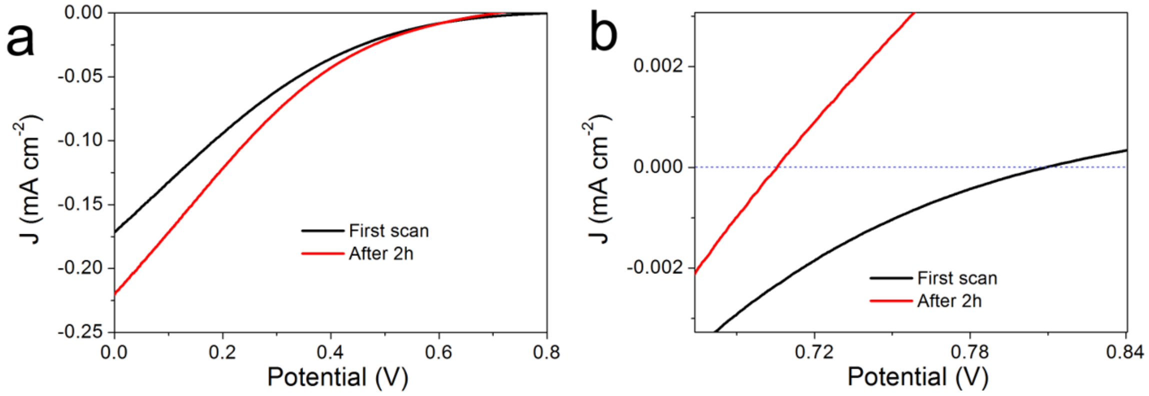

Figure 3-9 (a) Solid-state J-V curves of a $Cu_2O/Ga_2O_3/TiO_2$ DWE measured in 2-electrode configuration (in air, no electrolyte present), before and after a 2 hour stability measurement at short circuit. We note that the fill factor is poor and the series resistance is high since our DWE architecture was designed only to sense the potential of the surface with current being extracted into the electrolyte, and not to efficiently extract current through WE2. (b) Zoom-in of the V_{OC} region.

at short circuit for 2 h, where an obvious V_{oc} decrease in a range of 100 mV was observed. We note that the fill factor is poor and the series resistance is high since our DWE architecture was designed only to sense the potential of the surface with current being extracted into the electrolyte, and not to efficiently extract current through WE2. We therefore attribute the loss of the PEC performance in this system to an intrinsic problem with the Cu_2O/Ga_2O_3 junction, since corrosion through any pinholes in the ALD protective layer can be ruled out in the solid state measurement. Further studies are underway to more clearly identify the underlying reason for the instability in this junction.

3.1.4 Restorable V_{oc} behavior of the Cu_2O/Ga_2O_3 junction

The Cu_2O/Ga_2O_3 junction has shown instability. The generated V_{oc} decreases with time, which results in the negatively shifted onset potential in the J-V1 curve during the illuminated stability test. However, after being kept in the dark for 5 min, the onset potential positively shifts, from 0.7 to 0.76 V_{RHE}, (green and blue curves in Figure 3-12a). With the help of the DWE electrode, we then measure the V_{oc} and investigate the V_{oc} as a function of time. The first V_{oc}-time curve in Figure 3-12 b exhibits an initial V_{oc} of 0.75 V and then exponentially decreases in a few minutes until a relative steady value of 0.67 V. After being kept in a dark condition overnight (12 h), the V_{oc} restores, and exhibits an initial value of 0.75 V before again

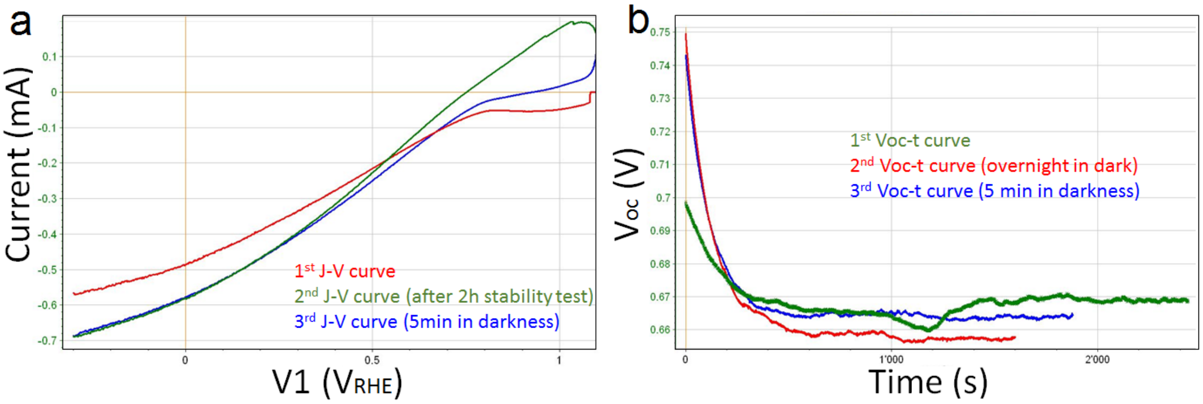

Figure 3-10 (a) LSV scans of the $Cu_2O/Ga_2O_3/TiO_2/Pt$ photocathode in the pH 5 phosphate, buffer: the 1st scan, the scan after 2 h-stability measurements and the scan after being kept in the dark for 5 min. (b) The V_{oc}-time curves in PV mode (two-electrode mode and without electolyte solution): the 1st Voc-time curve, the curve after being kept in the dark overnight, and the subsequent curve after being kept in the dark for 5 min.

slowly decreasing to 0.66 V. After being kept in the dark for another 5 min, the V_{oc} recovers to 0.7 V, and the slow decrease is again observed. This "restorable V_{oc}" behavior of Cu_2O/Ga_2O_3 was first revealed by the DWE technique. The reason is unclear so far but the "restorable V_{oc}" behavior with a time constant of few minutes is similar to the capacitance transient results by Mittiga and co-workers.[157] They found the transient decay in few minutes when applying reverse bias to Cu_2O and attributed this slow decay to Cu vacancies diffusion.

3.2 Sb_2Se_3-based DWE

3.2.1 Introduction

Sb_2Se_3 has been investigated as a promising absorber for solar energy conversion due to its narrow direct band gap (1.0-1.2 eV), high optical absorption coefficient and earth-abundance.[158] A remarkable solar conversion efficiency of around 6% has been achieved from Sb_2Se_3 polycrystalline film based-solar cells.[159] Recently, our group reported a Sb_2Se_3-photocathode towards water splitting. Coupled with the MoS_x catalyst, a photocurrent density of 5 mA cm^{-2} at 0 V_{RHE} was obtained in 1 M H_2SO_4. Furthermore, after a low temperature post-sulfurization process, a dramatically improved onset potential was obtained and the photocurrent density at 0 V_{RHE} increased to 16 mA cm^{-2}, as shown in Figure 3-13.[160] The reason

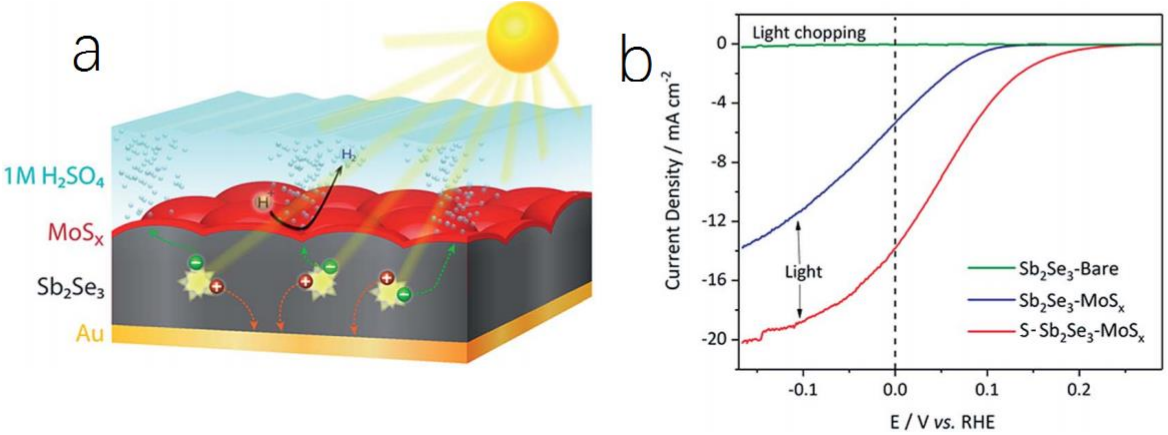

Figure 3-11 (a) Schematic representation of Sb_2Se_3–MoS_x photocathode. (b) Current density-potential characteristics of bare Sb_2Se_3(light chopping), Sb_2Se_3–MoS_x (non-sulfurized) and S-Sb_2Se_3–MoS_x (sulfurized) photocathode in 1 M H_2SO_4 under simulated one sun illumination.[160]

could be explained by a thin Sb_2S_3 hole-blocking layer that was formed between the Sb_2Se_3 and MoS_x layer, resulting in an enhanced charge separation. Here we applied the DWE technique in order to quantify the increased V_{oc} due to the sulfurization and investigate the Sb_2Se_3/Sb_2S_3 junction behavior. However, it was not possible to sense the electrochemical potential of the Sb_2Se_3 surface (or energy level of photo-excited electrons) with the remote configuration of the surface contact (WE2), due to the low lateral mobility of the photoexcited minority carriers. Besides, a 100-nm-thick TiO_2 layer was necessary to avoid short circuit when Au was sputtered onto the surface. Therefore, we fabricated a $Sb_2Se_3/TiO_2/Pt$ photocathode as the target sample. To study the Sb_2Se_3/Sb_2S_3 junction, the as-prepared Sb_2Se_3 thin film was sulfurized before the TiO_2 deposition by ALD.

3.2.2 Fabrication of Sb_2Se_3 DWE

150-nm-thick Au and 400-nm-thick Sb was sequentially sputtered onto cleaned FTO slides, followed by a selenization process with selenium pellets (30 mg) inside the same zone of a tube furnace in an Ar atmosphere at 350 °C for 40 min. To sulfurize the Sb_2Se_3 surface, sulfur powder was placed in one zone at 200 °C while Sb_2Se_3 sample was placed in the other zone (downstream), which was kept at 250 °C. Next, a 100-nm-thick TiO_2 layer was deposited by ALD and subsequently 5-nm-Pt was sputtered onto the TiO_2 surface as the catalyst. The sulfurized sample was named S-$Sb_2Se_3/TiO_2/Pt$. More selenization and sulfurization details can be found in our previous work.[160] Both $Sb_2Se_3/TiO_2/Pt$ and S-$Sb_2Se_3/TiO_2/Pt$ samples were then protected by epoxy, with a certain area of Pt exposed as the electrochemical active area.

To make the WE2 or the front contact, a 20 nm-thick Au layer was sputtered onto a part

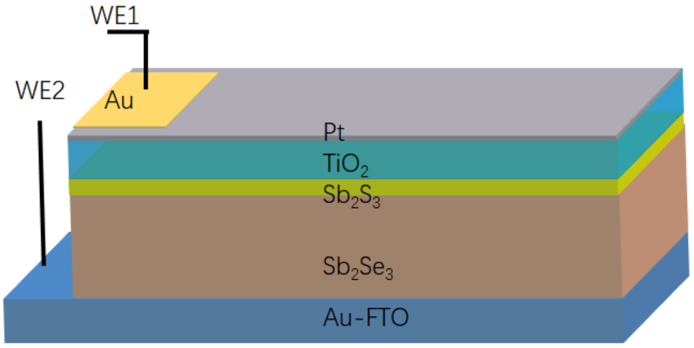

Figure 3-12 Schematic structure of the S-$Sb_2Se_3/TiO_2/Pt$ DWE. The epoxy is omitted here for clarity.

of the exposed Pt layer as well as the epoxy, as shown in Figure 3-14. A copper wire was then connected to the Au via Ag paint as the WE2 and covered another layer of epoxy for protection. The bare Au-coated FTO served as the WE1 or the back contact.

3.2.3 Results and Discussion

As shown in Figure 3-15, the sulfurized sample (S-Sb_2Se_3/TiO_2/Pt) exhibits an improved onset potential of ~0.35 V_{RHE}, compared to the S-Sb_2Se_3/TiO_2/Pt whose onset potential is ~0.21 V_{RHE}. The J-ΔV curves suggests that the V_{oc} generated by the Sb_2Se_3/TiO_2 heterojunction is ~0.21 V, which accords well with the value of the onset potential for the J-V1 curve. To investigate the Sb_2Se_3/Sb_2S_3 junction, the Sb_2Se_3 was sulfurized first, followed by the deposition of ALD-TiO_2. In this way, the V_{oc} is determined by the Sb_2Se_3/Sb_2S_3 junction and decoupled from the TiO_2 layer. Figure 3-13 shows that the V_{oc} generated by the Sb_2Se_3/Sb_2S_3 junction is ~0.35 V, 0.14 V more than the Sb_2Se_3/TiO_2 junction. Since both TiO_2 and Sb_2S_3 have a lower conduction band position than Sb_2Se_3, the V_{oc} difference could be from the conduction band offset. Regarding to the Sb_2Se_3/Sb_2S_3 junction, the conduction band offset is reported as < 0.1 V,[161] much smaller than the for the Sb_2Se_3/TiO_2 junction (0.35 V).[162]

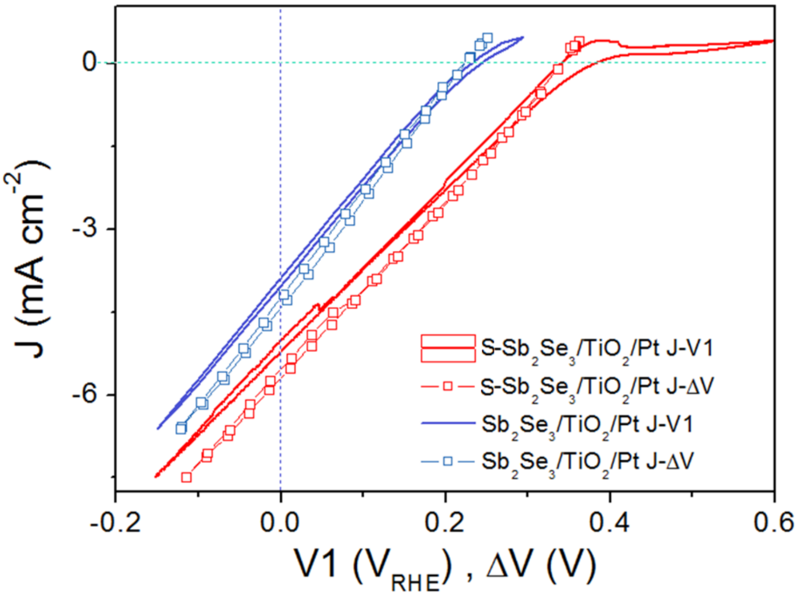

Figure 3-13 J-V1 and J-ΔV curves of Sb_2Se_3/TiO_2/Pt and S-Sb_2Se_3/TiO_2/Pt (sulfurized).

3.3 Stability of the p-Si/PA/TiO_2/Pt photocathode

3.3.1 Introduction

As previously mentioned, the conduction band offset is a key parameter for the V_{oc} generated by a heterojunction. Taking the Sb_2Se_3/TiO_2 junction as an example, the large conduction band offset contributes to the small V_{oc} of (0.21 V). Band edge engineering is a promising approach to obtain a large V_{oc} and a relatively positive onset potential for photocathodes. In particular, dipole-effect has been applied at the semiconductor/electrolyte interface and proved to be an effective strategy to tune the band edge offset.[163] However, this dipole layer suffers poor stability due to the direct contact to the electrolyte solution. Recently, our group reported that the ALD-TiO_2 functioned as an n-type partner for phosphonic acid (PA, H_3PO_3) modified p-Si, and also as a protective layer. As shown in Figure 3-16, the PA dipole layer shifts the relative band positions of the p-Si/TiO_2 junction, thus larger V_{oc} or photovolage (V_{ph}) can be achieved. For the p-Si/PA/TiO_2/Pt photocathode, the onset potential was positively shifted by ~0.2 V and the p–Si/PA/TiO_2 solar cell generated ~0.2 V larger V_{oc} than the counterpart without PA dipole layer.[164] In this section, we again fabricated p-Si/PA/TiO_2/Pt DWE to quantify the V_{oc} enhancement under water splitting condition. Additionally, the good stability of the underneath PA layer was confirmed by the DWE technique.

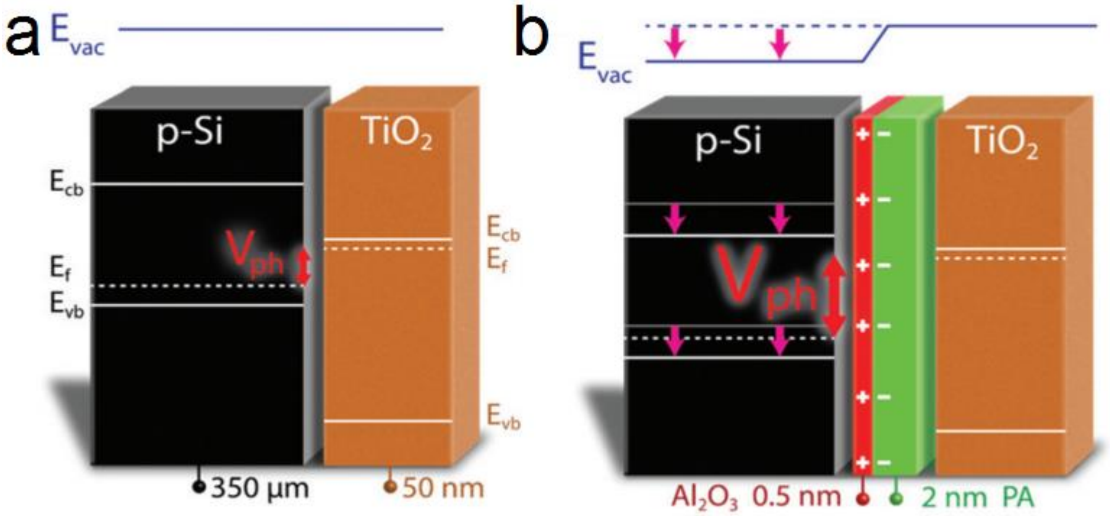

Figure 3-14 Band diagrams of p-Si/n-TiO_2 and p-Si/anchor layer/PA/n-TiO_2 in flat band condition.[164]

3.3.2 Fabrication of the p-Si/PA/TiO_2/Pt DWE

P-Si wafers (10-30 Ohm cm, doped by boron) were first cleaned and etched as in the previous process described in 2.2.1, and then quickly placed in the ALD chamber (120 °C) for the Al_2O_3 anchor layer deposition. Trimethylaluminium and H_2O were the precursors for Al and O, respectively and both of them are kept at room temperature (25 °C). The thickness of the Al_2O_3 was designed as 0.5 nm because thicker Al_2O_3 would inhibit the tunneling of the photo-excited electrons. The PA dipole layer was made by spin coating, where a 10 mM ethanol solution was used. Next, a 50-nm-thick TiO_2 was deposited by ALD to make the p-Si/TiO_2 junction and protect the PA layer. The p-Si/PA/TiO_2 wafer was attached to a Cu foil via Ga-In eutectic and covered by epoxy with a certain TiO_2 area exposed for sputtering a 2-nm-thick Pt layer. More details of PA layer fabrication can be found in our recent paper.[164]

The WE1 or the back contact was the Cu foil, fixed on a glass substrate. To fabricate the WE2, the same procedure was performed as described in 3.2.2.

3.3.3 Results and Discussion

Introducing the PA dipole layer to the p-Si/TiO_2 junction positively shifts the onset potential from ~0.1 to ~0.4 V_{RHE}, which is attributed to the increased larger V_{oc} from the dipole effect of

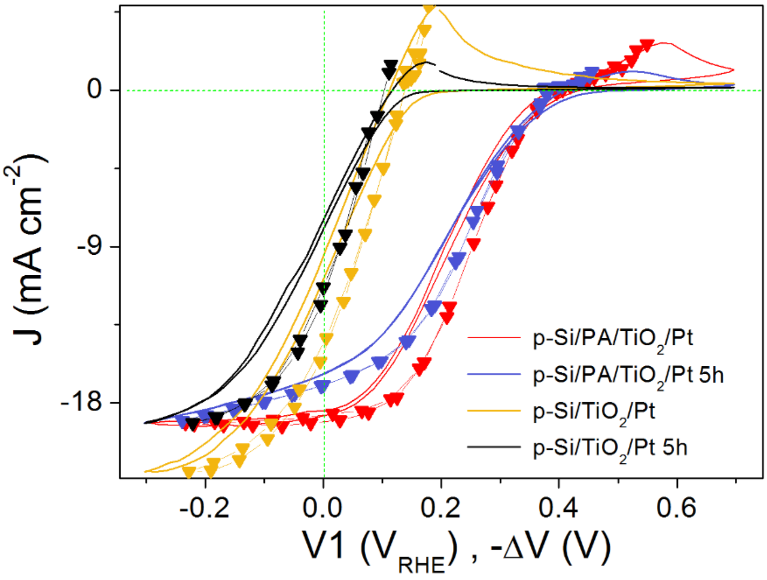

Figure 3-15 J-V1 (solid) and J-ΔV (solid+symbol) curves of p-Si/TiO_2/Pt with and without PA dipole layer in 1 M H_2SO_4 before and after the 5 h stability test.

the PA layer, as observed in Figure 3-17 (yellow and red solid curves). The V_{oc} of the p-Si/PA/TiO_2 junction is determined as ~0.4 V from the J-ΔV curve (red + symbol) while the p-Si /TiO_2 only exhibits a V_{oc} of 0.1 V. Even though the V_{oc} improvement could also be revealed by characterizing solar cells, the DWE technique demonstrates the investigation of the junction behavior under realistic photo-electrolysis condition.

To investigate the stability of the dipole effect, a 5 h chronoamperometry at 0 V_{RHE} was performed under illumination. For the p-Si/PA/TiO_2/Pt sample, a small FF loss in both J-V1 and J-ΔV curves were observed. The photocurrent density at 0 V_{RHE} decrease from 18.5 to 16.8 mA cm^{-2}. This suggests that the underlying p-Si/PA/TiO_2 junction slightly degraded. The saturation photocurrent density remained the same, indicating the robustness of the surface Pt catalyst. However, the saturated photocurrent density increased for the sample without the dipole (p-Si/TiO_2), suggesting that Pt peeled off from the surface, allowing more optical transmittance and leading to a slightly larger V_{oc} in the J-ΔV curve after the stability test. The difference behavior of the surface Pt may due to the sample-to sample variation. However, similar degradation of J-V and J-ΔV characters is observed after 5h test for p-Si/TiO_2/Pt, suggesting that the degradation of the dipole sample is not due to the instability of the PA layer.

3.4 Conclusions

In this chapter, the DWE technique was applied to several systems based on emerging materials and strategies, including the $Cu_2O/Ga_2O_3/TiO_2$/Pt, S-Sb_2Se_3/TiO_2/Pt and p-Si/dipole/TiO_2/Pt photocathodes. The DWE technique has shown good universality in *operando* characterization of buried junctions and unveiling of the degradation mechanism.

For the $Cu_2O/Ga_2O_3/TiO_2$/Pt photocathode, the large V_{oc} (~0.8 V) was determined from the J-ΔV curve and makes the onset potential as early as ~ 0.8V_{RHE} in the J-V1 curve. Besides, the intrinsic instability of the Cu_2O/Ga_2O_3, instead of the catalyst degradation, results in the reduced photovoltaic output after a stability measurement. Furthermore, we also found that the Cu_2O/Ga_2O_3 junction showed an intriguing “restorable V_{oc}” property, where the decreased V_{oc} restored after kept in dark for enough long time, perhaps due to the mobility of copper vacancies.

For the S-Sb_2Se_3/TiO_2/Pt photocathodes, we have proved that the improved J-V1 behavior was attributed to the large V_{oc} generated by the Sb_2Se_3/Sb_2S_3 junction formed during the post-sulfurization process. The Sb_2Se_3/Sb_2S_3 junction has a more favorable conduction band offset and promises a larger built-in voltage than the Sb_2Se_3/TiO_2 junction.

In the p-Si/PA/TiO_2/Pt photocathode case, the DWE technique has revealed and quantified the increased V_{oc} by the PA dipole layer. Note that here the TiO_2 act as both n-type partner for the pn junction and the protective layer. After a 5 h stability test, the slightly FF loss observed the J-ΔV curves suggests the degradation of the p-Si/PA/TiO_2 junction, which is mainly responsible for the FF loss in the J-V1 PEC behavior. However, a similar degradation was found in the photocathode without the PA layer, which indicates that the dipole layer is not the source of the loss in performance.

4 Identification of the Charge Carrier Processes in np$^+$Si/TiO$_2$/Ni Photoanodes

4.1 Introduction

4.1.1 Charge carrier processes in the PEC process

The magnitude of the photovoltage is mainly decided by the band alignments across the semiconductor/liquid interface or the buried junction. In addition, the PEC performance can also be affected by the kinetics of charge carrier transfer across the photoelectrodes. Besides the basic charge separation (by the electric field in the space charge region), Figure 4-1 depicts several charge carrier processes in a single n-type semiconductor photoanode under photo-electrolysis condition. The electron-hole pairs can recombine in the bulk or the space charge

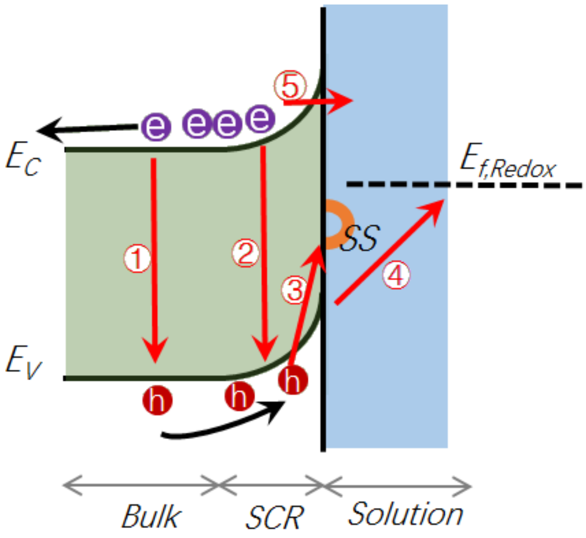

Figure 4-1 Typical charge carrier processes in a photoanode. Besides the desired processes of electrons moving to the back contact and holes to the solution interface due to the electric field (depicted by black arrows), photo-excited electron-hole pairs can recombine in the bulk of the n-type semiconductor (①) and the space charge region (SCR, ②). Surface recombination (③) occurs at the solid/solution interface due to surface states (SS); Holes arriving at the surface catalyst operates water oxidation (④); Electrons can tunnel through the energy barrier and enter the solution (⑤).

region of the semiconductor, showing up in the form of band to band recombination or recombination over defect states.[165,166] This recombination will affect the lifetime of the minority carriers, which are holes in this case. The surface recombination is mainly attributed to the surface states (SS) created by the termination of the crystal lattice. Photoexcited-holes can be trapped inside the SS and water oxidation is thus inhibited. The surface recombination effect can be relieved by a passivation layer or surface catalyst. [167,168] As for the multilayer structured photoelectrode, more charge carrier processes are involved and need to be considered due to the extra interfaces. For example, a $np^+Si/TiO_2/Ni$ photoanode where the photovoltage is generated by the np^+Si homojunction, and adding the TiO_2 protective layer produces at least 3 interfacial issues: (1) how can holes transfer through the p^+Si/TiO_2 interface; (2) how can holes transfer through the TiO_2 layer with intrinsic n-type nature; (3) how can holes transfer through the TiO_2/electrolyte interface. Moreover, the Ni catalyst also plays a critical role in hole transfer at the solid/liquid interface. Both the morphology and the oxidation state of the Ni species are important parameters to design a highly efficient photoanode.[58,169,170]

In this scenario, in-depth investigation of the charge carrier process in a photoelectrode is of vital significance, but is still a formidable challenge due to the complex multilayer structure, especially under operational water splitting conditions. To date, various in-situ approaches have been developed to investigate charge carrier processes hidden in the overall PEC performance, and most of them depend on spectroscopies such as synchrotron-based X-ray techniques.[171] However, those spectroscopic techniques cannot provide mechanistic information under the realistic operation condition and requires costly infrastructure. Additionally, the DWE technique introduced in Chapter 2 and 3 is an *operando* method but only provides energetic information rather than charge kinetics. Therefore, a less costly and *operando* methodology is highly desirable to provide a comprehensive study of the charge carrier process in PEC systems.

4.1.2 Photoelectrochemical Impedance Spectroscopy (PEIS)

Photoelectrochemical impedance spectroscopy (PEIS) is an established method for characterizing charge carrier phenomena under operational conditions. It has been commonly employed to detect the origin of limitations and improve the efficiency of these solar energy conversion devices.[172,173] The impedance response of the system is usually displayed in a

Nyquist plot, where charge carrier processes can be visualized and distinguished by the semicircle features in different frequency domains. For a complex system, different charge carrier processes can be extracted and separately studied by applying appropriate equivalent circuit (EC) models consisting of several constant phase elements (CPE).[174] Additionally, PEIS provides the electrochemical capacitance nature of different charge carrier processes. Combined with resistance information, the time constant for each charge carrier process can be obtained.

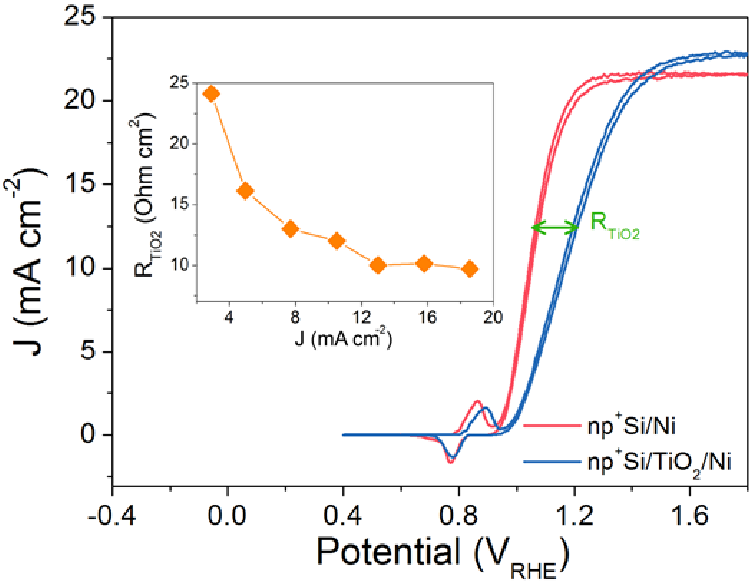

Figure 4-2 Typical CVs of np$^+$Si/Ni photoanodes with or without 100 nm thick TiO_2 protective layer in 1 M KOH under one sun illumination. The fill factor (FF) difference results from the increased series resistance brought by the TiO_2 layer (R_{TiO2}). The inset shows R_{TiO2} as a function of photocurrent density calculated from the J-V curves.

In this chapter, we aim to unveil and elucidate the detailed charge carrier processes in ALD-TiO_2 protected photoanode (np$^+$Si/TiO_2/Ni) by using PEIS. In particular, adding a protective TiO_2 layer introduce an extra series resistance, denoted as R_{TiO2} as confirmed by the decreased FF in the J-V curve (Figure 4-2). The potential dependence of R_{TiO2} from an np$^+$Si/TiO_2/Ni photoanode was analyzed. Additionally, we fabricated an np$^+$Si/TiO_2/Ni DWE to perform V2-controlled PEIS measurements, where the charge transfer in the p$^+$Si/TiO_2/Ni configuration was investigated, excluding the effect of charge recombination inside the np$^+$Si junction. By this means, a systematic investigation of the charge carrier processes in

$np^+Si/TiO_2/Ni$ protected photoanodes could be achieved. Finally, we applied PEIS to a $pn^+Si/TiO_2/Pt$ photocathode for comparison. The voltage dependency of R_{TiO2} in the photocathode case was investigated as well.

4.2 Experimental

4.2.1 Fabrication of $np^+Si/TiO_2/Ni$ DWE

4.2.1.1 Si wafer cleaning

(111)-oriented np^+Si and pn^+ wafers (thickness ~0.5 mm) were purchased from PrimeWafers (Country). For np^+Si wafers, the n-Si substrate was lightly phosphorous-doped (10^{16} cm^{-3}) and a 2 μm-thick heavily p^+-type surface layer (polished) was doped with boron (10^{19} cm^{-3}). For pn^+Si wafers, the p-Si substrate was lightly boron-doped (10^{16} cm^{-3}) and a n^+-type surface layer (polished) was phosphorus doped (10^{19} cm^{-3}). The wafers were cut into 2.5 × 1 cm^2 pieces followed by sequential sonication in acetone, ethanol and MilliQ water (18 MΩ) for 10 minutes each. Then a two-step deep cleaning was accomplished by using a 5:1:1 mixture of $H_2O:NH_4OH:H_2O_2$ and a 5:1:1 mixture of $H_2O:HCl:H_2O_2$, both in 50 °C water bath for 10 minutes, in order to completely remove organic and inorganic contaminants. To etched away the native oxide layer, wafers were finally dipped in 2% HF for 30 s, followed by rinsed with deionized water and dried under N_2 stream for the ALD-TiO_2 deposition.

4.2.1.2 Fabrication of the front contact and catalyst deposition

After the ALD-TiO_2 layer deposition, the back contact (the first working electrode or WE1) was made to the back side of the silicon by scratching the wafer, smearing Ga–In eutectic (Aldrich) and attaching a conductive copper wire. A layer of epoxy resin (Loctite Epoxide-resin EA 9461) was then used to cover and glue the wafer to a glass microscope slide, with a certain portion of the front surface left uncovered as the electrochemical active area. For making the front contact, a 20-nm-thick Au layer was sputtered (Safematic CCU-010) onto the epoxy as well as a small part of the exposed TiO_2. A copper wire was connected to the Au layer with Ag paint (Ted Pella, Inc.) on top of the epoxy, serving as the second working electrode (WE2). Finally, WE2 was protected from the electrolyte solution by masking it with another epoxy layer. In V2-controlled PEIS measurements, WE2 was connected to the p^+Si layer instead of TiO_2, as drawn in Figure 4-3. The pn^+Si/TiO_2 DWE were fabricated via the same methods except that WE2 connects to the p^+Si surface.

Ni metal layers (nominally 2 nm) were deposited onto the surface by sputtering. A working current of 30 mA and a working pressure of $8E^{-3}$ mbar were applied.

4.2.2 PEIS measurements

PEIS was performed during the voltage scanning in the desired potential window in steps of 50 mV with a 60 s equilibrium time at each bias potential step. The frequency range was from 10^{-1} Hz to 10^6 Hz and an oscillating voltage of 15 mV was applied. For photoanodes, PEIS were recorded in 1.0 M KOH, and 0.5 M H_2SO_4 was used for photocathodes. PEIS data were further fitted with ZView software (Scribner). For all spectra fitting process, a constant phase element (CPE) was used for the capacitive element. Note that the impedance study in this work are only based on the resistances rather than capacitances. This is because one Nyquist plot can be fitted with many different CPE arrangements, and thus it is hard to extract meaningful

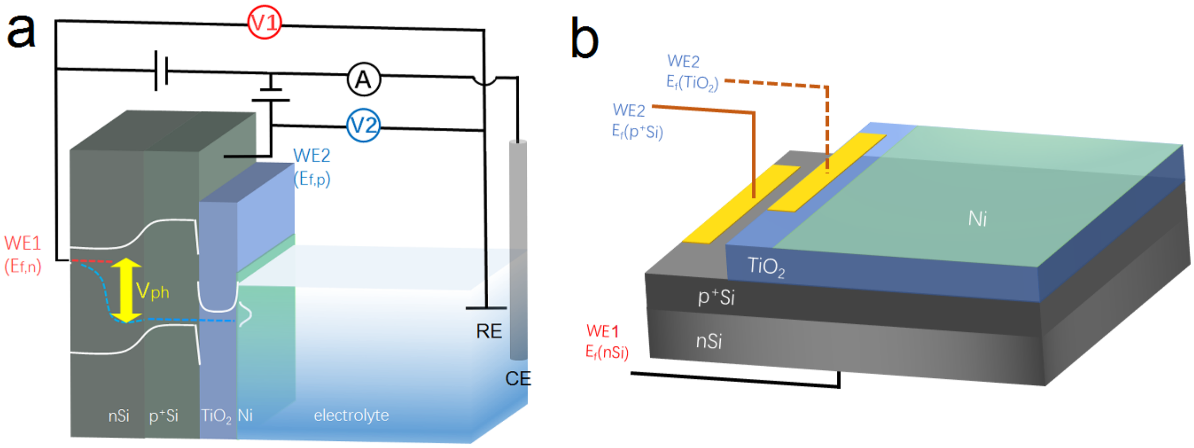

Figure 4-3 (a) Schematic illustration of $np^+Si/TiO_2/Ni$ DWE. For back contact potential (V1) controlled measurements (CV and EIS), front contact potential (V2) was kept at open circuit. In terms of V2 controlled measurements, V1 was kept at open circuit. V1 and V2 also represent the quasi Fermi levels of majority carriers in nSi (electron) and p^+Si (hole), respectively. (b) The structure of the second working electrode either connected to the p^+Si or TiO_2 surface via a 20-nm-thick Au layer. The WE2 is protected from the direct contact to the electrolyte solution by coating epoxy (omitted for clarity).

information. However, the resistances are usually in series no matter what the arrangement of the capacitive elements, and this makes a resistance-based study more reliable.[174]

The flat band potential (E_{FB}) of the ALD-TiO_2 layer was determined with a Mott -Schottky plot, which was derived from an EIS measurement in a three-electrode configuration under dark condition. The working electrode was a fluorine-doped tin oxide (FTO)-coated glass with a 100 nm-thick ALD TiO_2 layer. The counter and reference electrodes were a Pt wire and a Ag/AgCl electrode, respectively. The electrolyte solution used was 1 M H_2SO_4. The space charge capacitances (C_{sc}) were extracted from the fitting of Nyquist plots under applied potentials, thus no frequency dispersion appears in the Mott-Schottky plots.

4.3 Determination of band structures of nSi, p$^+$Si and ALD-TiO_2

The Fermi level of nSi and p$^+$Si are determined by equation (1) and (2), respectively.

$$E_{CB} - E_{FB} = \frac{kT}{q}\, ln\left(\frac{N_D}{N_C}\right) \qquad (4\text{-}1)$$

$$E_{FB} - E_{VB} = \frac{kT}{q}\, ln\left(\frac{N_V}{N_A}\right) \qquad (4\text{-}2)$$

where N_C and N_V are the effective density of states in the Si conduction band (~2.8×10^{19} cm^{-3}) and valence band (~1.2×10^{19} cm^{-3}), respectively, q is the electron charge, k is the Boltzmann constant and T is the temperature in Kelvin. For Si, E_{CB} and E_{VB} are located at ~ -0.5 and 0.6 eV versus RHE, respectively.[175] The donor density (N_D) of nSi is 10^{16} and the acceptor density

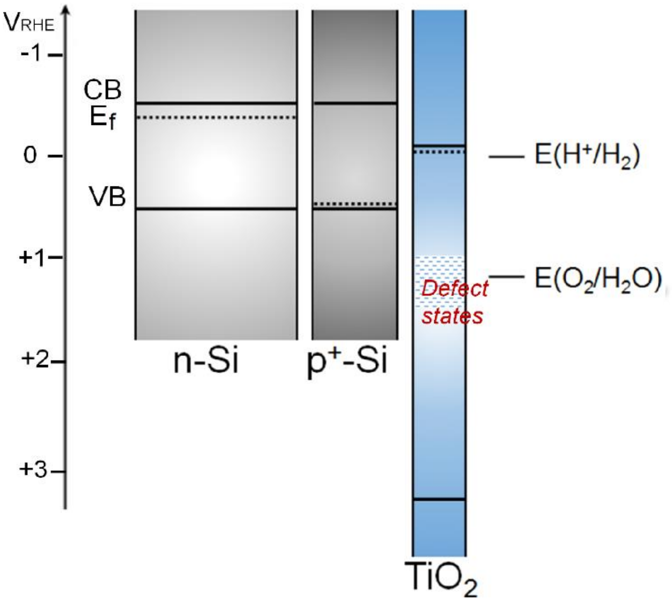

Figure 4-4 Band structures of nSi, p$^+$Si and ALD-TiO_2.

(N_A) of p^+Si is 10^{19} cm^{-3}. Therefore, E_{CB} - E_{FB} is ~ -150 mV, which means that the nSi fermi level locates 150 mV lower than the conduction band. In terms of p^+Si, $E_{FB} - E_{VB}$ is almost 0, suggesting that the high acceptor density makes the Fermi level location extremely close to the valence band edge.

The actual Fermi level position of ALD-TiO_2 was determined by the Mott-Schottky plot ($1/C_{sc}^2$ plotted versus the applied potential). The linear part fitting related to the equation is shown below:

$$\frac{1}{C_{SC}^2} = \frac{2}{N_D \varepsilon \varepsilon_0 q}\left(E - E_{FB} - \frac{\mathrm{kT}}{q}\right) \quad (4\text{-}3)$$

where E is the applied potential, ε is the dielectric constant (here, 38 for ALD-TiO_2) and ε_0 is the permittivity of vacuum.[176] C_{sc} is the space-charge capacitance. N_D is the doping density of ALD-TiO_2, which can be obtained from the slope of equation (3). The positive slope suggests the n-type doping and the x-intercept is indicative of the E_{FB}. By applying equation (3), a E_{FB} of -0.03 V_{RHE} and a N_D density of 5.2×10^{20} cm^{-3} can be determined. Applying equation (1) results in a CB which is located slightly higher than E_{FB}. Nc of ALD-TiO_2 is 7.8×10^{20}.[32] Since E_{FB} refers to the applied voltage that results in no band bending, E_{FB} is actually the Fermi level position of the semiconductor. Thus, the Fermi level of ALD-TiO_2 is located at -0.03 V_{RHE}. Finally, band energy positions for n-Si, p^+Si and TiO_2 are drawn in Figure 4-4. The defect states in the TiO_2 will be introduced in the next chapter.

4.4 Nyquist plots fitting

4.4.1 Back contact-controlled PEIS

Figure 4-5 provides the Nyquist and Bode plots achieved from a $np^+Si/TiO_2/Ni$ photoanode with different potential bias under illumination. 0.55 V_{RHE} is a potential prior to the onset of photocurrent for water oxidation. Three semicircles features are observed in the Nyquist plot. Note that the last semicircle with low frequencies shows a linear behavior as the resistance value is enormous. Thus we assign this semicircle as the charge transfer resistance at the surface Ni catalyst (NiCat) for water oxidation, named R_{ct}. The semicircle with high frequencies is assigned as the charge recombination inside the np^+Si junction, named R_{rec}. The intermediate semicircle was assigned as the charge transfer through the TiO_2, named R_{TiO2}. Due to the

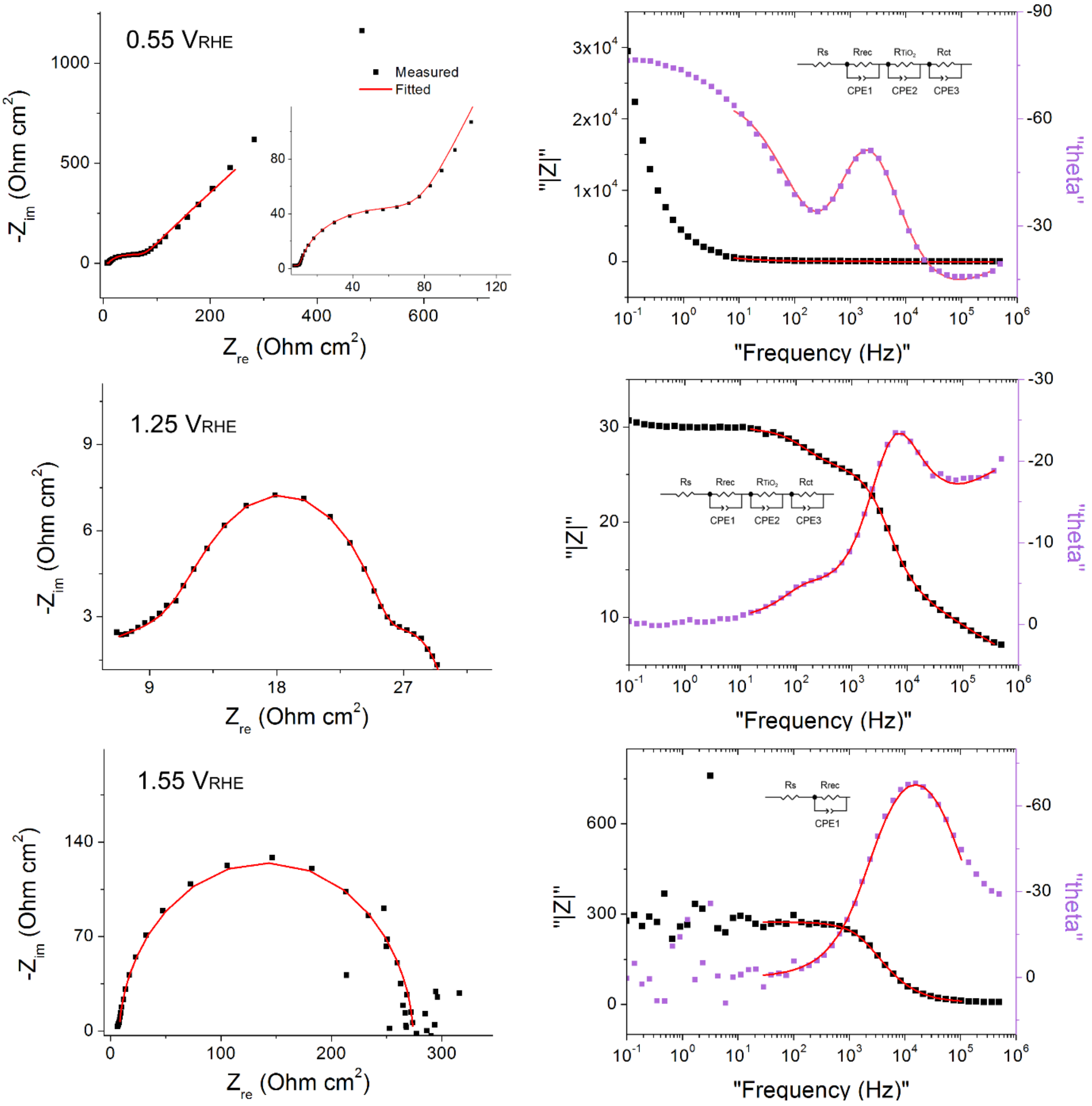

Figure 4-5 Nyquist and Bode plots and corresponding fitting of an np$^+$Si/TiO$_2$/Ni photoanode at back contact potentials of 0.55, 1.25 and 1.55 V$_{RHE}$ under one sun illumination. Equivalent circuit models are given as well. R$_s$ is the series resistance raised by the electrolyte solution. R$_{rec}$ is the overall resistance of charge recombination taking place in the abosrbers. R$_{TiO2}$ is the overall resistance of charge transfer through the TiO$_2$ layer. R$_{ct}$ is asscoicated with the oxygen-evolving process at the Ni catalyst surface.

photovoltage generated by the buried n-p Si junction, at 1.25 V$_{RHE}$, water oxidation is both thermodynamically and kinetically allowed, and the R$_{ct}$ becomes very small (few Ohm cm^{-2}). At 1.55 V$_{RHE}$, the R$_{ct}$ disappears and the intermediate R$_{TiO2}$, and the R$_{rec}$ exhibits a much larger value.

4.4.2 Front contact-controlled PEIS

The front contact (V2)-controlled PEIS shows similar trend except that R_{rec} is absent, as shown in Figure 4-6. In the prior-to-onset potential region, for example, 1.16 V_{RHE}, 3

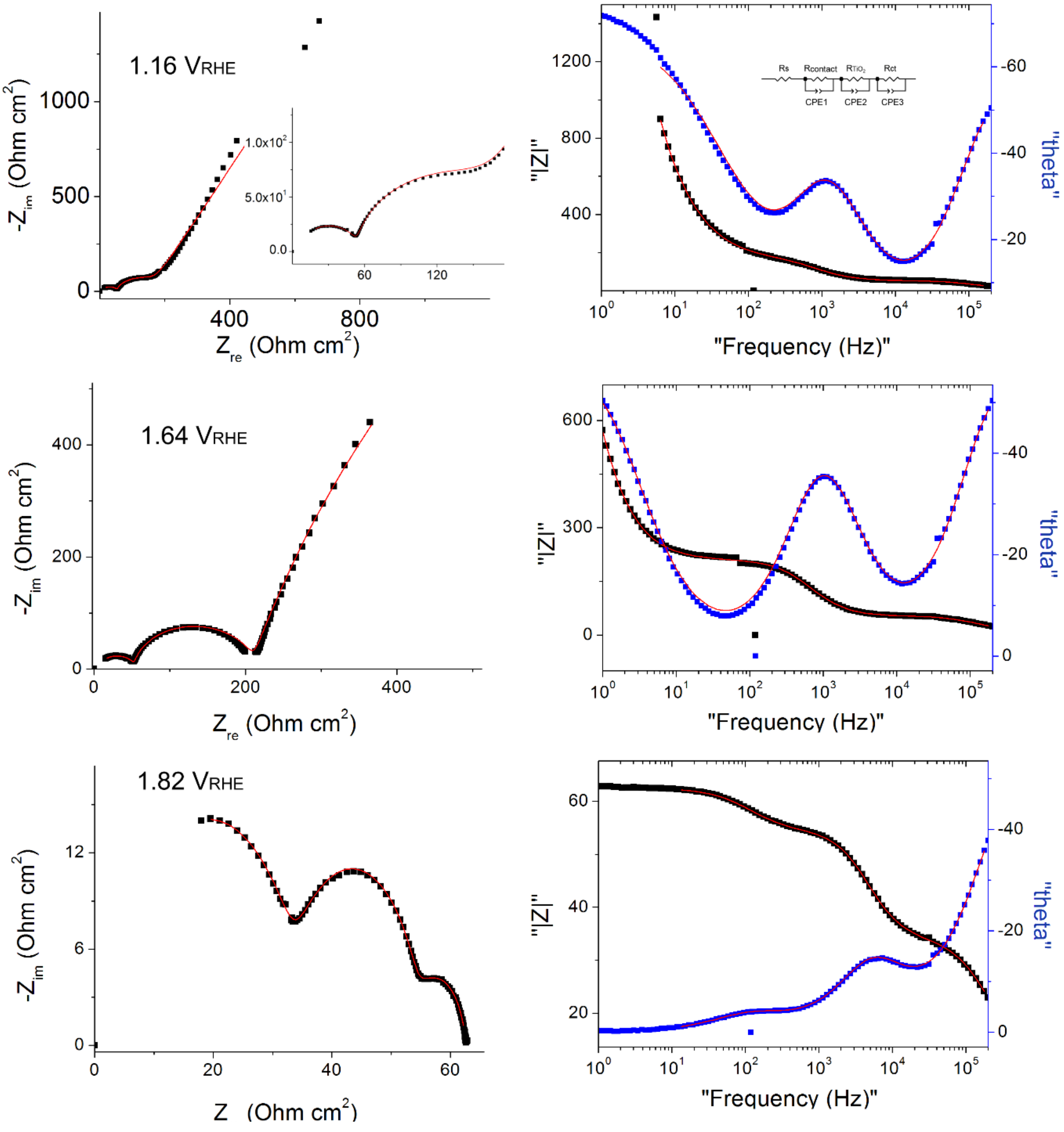

Figure 4-6 Nyquist and Bode plots from V2-controlled PEIS measurements and the corresponding fitting of an np$^+$Si/TiO$_2$/Ni photoanode at V1 of 1.16, 1.64 and 1.82 V_{RHE} under one sun illumination. In V2-controlled PEIS measurements, charges flow from the front contact to a p$^+$Si layer, then transfer through the TiO_2 layer and finally reach the surface of the Ni Catalyst. V2 was kept at open-circuit.

semicircles are revealed. In addition to the R_{TiO2} with intermediate frequency and R_{ct} with low frequency, the resistance in the high frequency region is raised by the contact of WE2, named $R_{contact}$, featuring a steady value (~40 Ohm cm^{-2}) in the prior-to-onset potential region and decreases as the current increases.

4.5 Charge carrier process in the $np^+Si/TiO_2/Ni$ photoanode

Figure 4-2 presents typical cyclic voltammograms (CVs) of np^+Si/Ni photoanodes with and without 100 nm ALD-TiO_2 layer in 1 M KOH (aq) under one sun illumination. A clear fill factor (FF) decrease can be observed for the TiO_2 protected one, indicating that the TiO_2 layer indeed introduces an extra series resistance (R_{TiO2}). Approximate R_{TiO2} values were calculated through a simple method: in the potential region where the photocurrent is rising (1.0-1.2 V_{RHE}), the potential difference of the two J-V curves in Figure 4-2 was divided by the photocurrent density.

From the PEIS fitting, we consider that three main processes are involved in the $np^+Si/TiO_2/Ni$ photoanode under the photo-electrolysis condition, as illustrated in Figure 4-7. When illuminated, minority carrier (holes) are excited and move to the p^+Si/TiO_2 interface by the built-in electric field across the np^+Si homojunction, accompanied by charge recombination process either in the bulk of Si or the space charge region (Process 1 in Figure 4-7a). Process 2 represents that charge carriers somehow transfer through the thick ALD-TiO_2 layer and arrive at the Ni catalyst. The third process is the charge transfer on the catalyst surface for water oxidation, which of course requires a potential in excess of the thermodynamic potential for oxygen evolution. These three steps can be expressed in terms of resistance obtained from the impedance measurements. The EC model used for fittings is provided in Figure 2-7a, wherein all resistances are in series.[174] Note that even though several EC models have been developed to picture PEC processes, it is the capacitive rather than resistive elements which distinguish them, which is why our following analysis is fully resistance-based.[174] Clear multi-semicircle features and voltage-dependency can be observed. Figure 4-7b plots the typical J-V1 curve of a $np^+Si/TiO_2/Ni$ photoanode, as well as the voltage–dependent values of the resistances obtained from the fit of the measured impedance spectra.

The high frequency resistance, R_{rec}, shows a low and constant value in the pre-onset potential region and exponentially increases after the onset potential. Generally, R_{rec} represents the overall recombination processes taking place in the space charge region and the bulk of the absorber, with larger values being better for device performance. The small R_{rec} values before the onset potential imply that the charge cannot be injected into the electrolyte and thus can

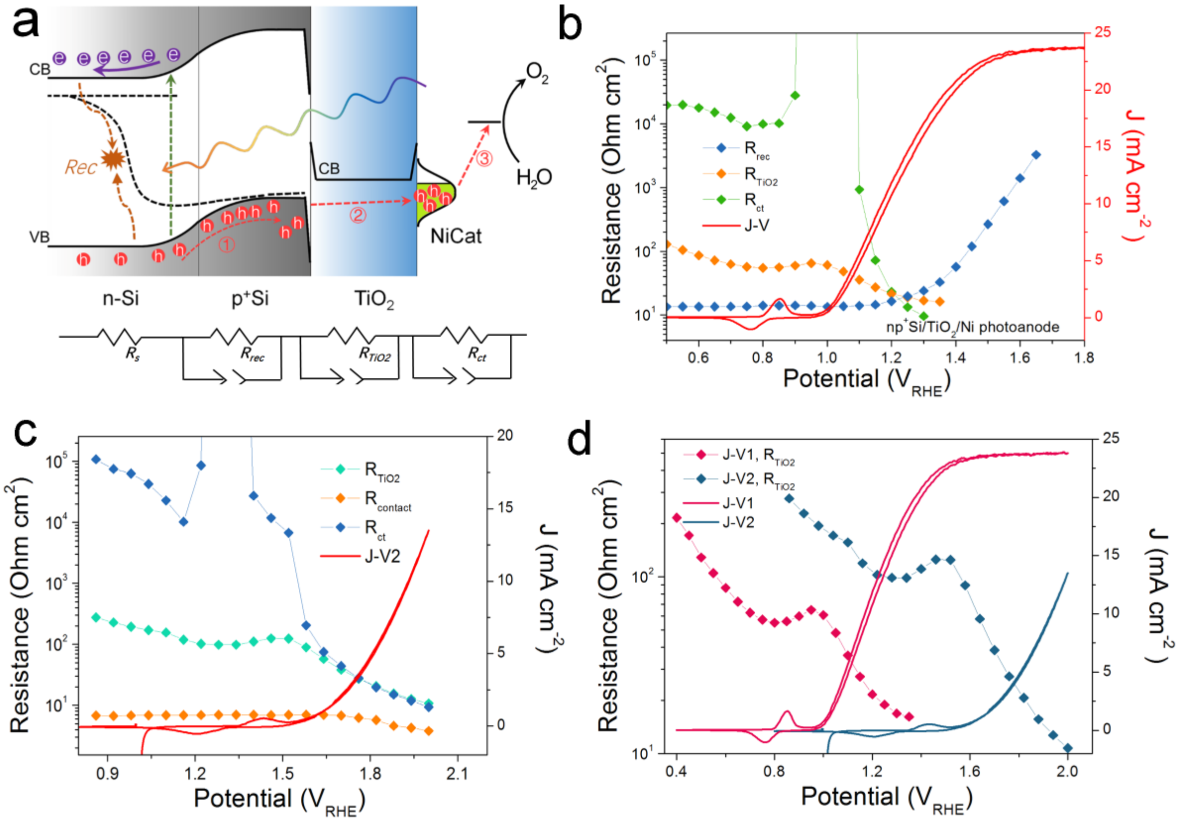

Figure 4-7 (a) Schematic illustration of charge transfer processes and energy band alignment of an O_2-evolving $np^+Si/TiO_2/Ni$ photoanode. The depicted process 1 represents the recombination taking place inside the buried np homojunction; Process 2 represents the charge transfer through the TiO_2 protective layer to reach the surface Ni catalyst (NiCat); Process 3 represents the water oxidation reaction process on the NiCat. The model used for fitting the EIS data is illustrated as well. R_s is the series resistance from the electrolyte solution. R_{rec}, R_{TiO2} and R_{ct} are assigned to Process 1, 2, and 3, respectively. (b) Resistances and photocurrent densities (J) versus the back contact potential. R_{rec}, R_{TiO2} and R_{ct} were obtained from fittings of Nyquist plots of V1-controlled PEIS. R_s was not plotted here. (c) Resistances and J-versus V2. $R_{contact}$, R_{TiO2} and R_{ct} were obtained from fittings of Nyquist plots of V2-controlled PEIS. R_s was not plotted here, either. (d) Comparison of R_{TiO2} obtained from V1 and V2 controlled PEIS.

only recombine. As charges flow into the electrolyte, the recombination process is suppressed due to the efficient charge separation, and under increased bias, R_{rec} consequently increases.

The low frequency resistance, R_{ct}, has large values (10^4 Ohm cm^2) before the onset potential, representing the inhibited O_2-evolving charge transfer process over the Ni catalyst into the electrolyte. Notably, R_{ct} shows a valley in the Ni-redox potential region, indicating the increased current flow due to the catalyst oxidation (0.9-1.1 V_{RHE}). Afterwards the resistance increases again before it steeply drops as the oxygen evolution current sets in, which is related to the charge storage /release properties of NiCat.[174,177] As the O_2-involving photocurrent increases, the value of R_{ct} dramatically reduces and finally disappears at very positive potential region (after 1.4 V_{RHE}), suggesting the fast charge transfer kinetics at the catalyst/electrolyte interface.

R_{TiO2}, with an intermediate frequency range, is related to the charge carrier processes in the TiO_2 protective layer. We note that several sub-process resistances can contribute to the overall R_{TiO2}, including charge transfer through the Si/TiO_2 and TiO_2/Ni catalyst interfaces, as well as the charge transport inside the TiO_2 layer. In the potential window from 0.4 to 1.3 V_{RHE}, R_{TiO2} declines continuously and shows a valley in the Ni-redox potential region. This valley is due to the hole storing properties of the NiCat. Both the downward trend and values of R_{TiO2} in the potential region of >1.0 V_{RHE} are consistent with the results shown in the inset of Fig. 1b, providing further evidence for the correct assignment of this process to the TiO_2 layer. Additionally, we performed V2-controlled impedance measurements, as shown in Figure 4-7c. R_{TiO2} was also observed and shows similar potential dependence to that in V1-controlled measurements. Notably, R_{TiO2} shows a shift between the V1 and V2- controlled impedance spectra (Figure 4-7d), which arises from the photovoltage provided by the underlying PV.

4.6 Charge carrier process in the $pn^+Si/TiO_2/Pt$ photocathode

For comparison, a $pn^+Si/TiO_2/Pt$ photocathode system was investigated. Similarly, three charge carrier processes are presented in Figure 4-8a, in accordance with the Nyquist and Bode plots shown in Figure 4-9. As can be seen in Figure 4-8b, R_{ct} shows large values until the hydrogen-evolving current rises, and then R_{ct} quickly disappears. Also, R_{rec} shows small values before the onset of H_2 evolution, and increases as the photocurrent current increases under increasingly strong bias (inhibiting recombination). R_{TiO2} decreases upon scanning to more negative potentials, from thousands to a few Ohm cm^2, and eventually disappears. R_{TiO2} also appears in V2-controlled PEIS measurements and exhibits a photovoltage-shift (Figure 4-8c), similarly to the photoanode case.

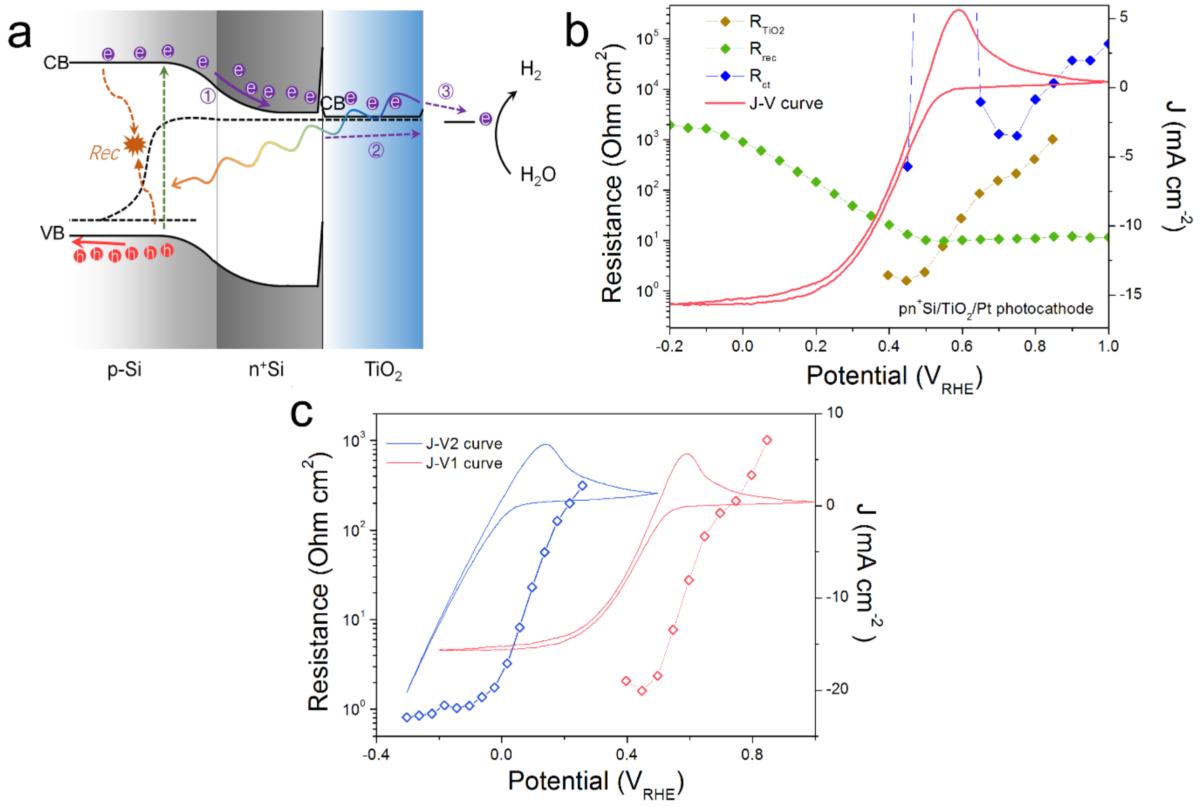

Figure 4-8 (a) Schematic energy band alignment in a H_2-evolving pn$^+$Si/TiO$_2$/Pt photocathode. Similarly, the depicted process 1 represents the recombination taking place inside the buried pn$^+$ homojunction; Process 2 represents the charge transfer through the TiO$_2$ protective layer and to reach the surface Pt catalyst; Process 3 represents the hydrogen evolution reaction process on the Pt. (b) Resistances and photocurrent densities versus the back contact potential. (c) R_{TiO2} obtained from V1 and V2 controlled PEIS measurements.

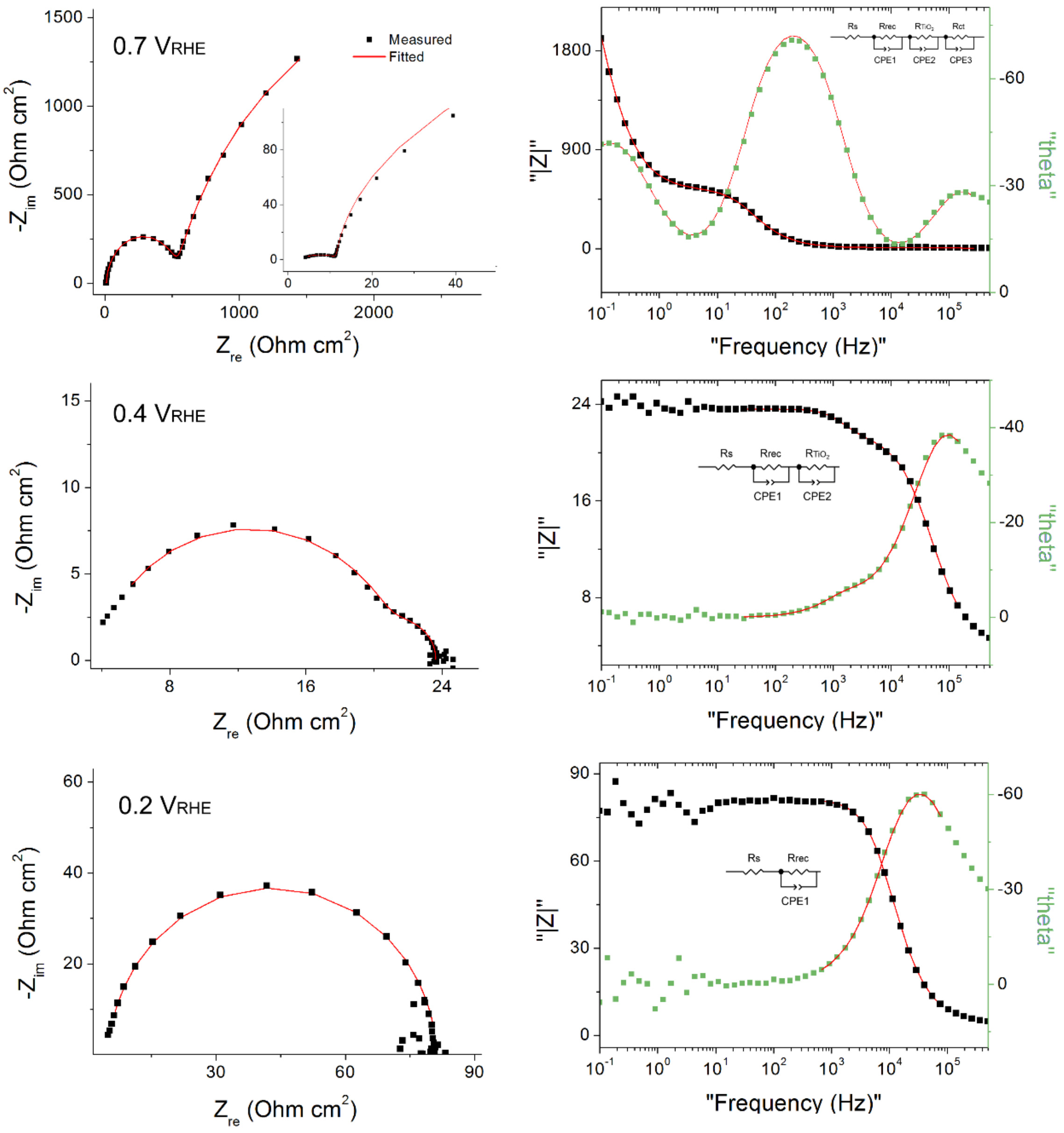

Figure 4-9 Nyquist and Bode plots and corresponding fitting of an pn$^+$Si/TiO$_2$/Pt photocathode at back contact potentials of 0.7, 0.4 and 0.2 V$_{RHE}$ under one sun illumination. Equivalent circuit models are given as well. R$_s$ is the series resistance raised by the electrolyte solution. R$_{rec}$ is the overall resistance of charge recombination taking place in the pn$^+$Si homojunction. R$_{TiO2}$ is the overall resistance of charge transfer through the TiO$_2$ layer. R$_{ct}$ is associated with the H$_2$-evolving process at the Pt catalyst surface.

4.7 Conclusions

We have applied PEIS measurements to unveil the charge carrier process in the np$^+$Si/TiO$_2$/Ni photoanode. Three basic processes have been identified and studied in the form of resistance, including R_{rec}, R_{TiO2} and Rct, according to their potential dependencies and frequency domains. In particular, we performed surface contact-controlled PEIS to further confirm the potential dependency of R_{TiO2}. Finally, the R_{TiO2} in the photocathode case has been investigated for comparison.

As mentioned in section 4.1.1, photo-excited holes transfer through the ALD-TiO$_2$ layer, which seems to contradict to the n-type nature of TiO$_2$. Moreover, Figure 4-4 shows that there is a huge barrier between the valence bands of TiO$_2$ and p$^+$Si, which should preclude hole transfer. Even though the resistance of charge transfer through the ALD-TiO$_2$ layer (R_{TiO2}) has been studied, the results are still not enough to explain the “hole-leaky” property of TiO$_2$. This intriguing phenomenon will be further elucidated in next chapter.

5 Understanding the “hole-leaky” property of TiO_2 as the protective layer for photoanodes

5.1 Overview of the “hole-leaky” property of TiO_2

ALD-TiO_2 has been shown to protect pSi-based photocathodes but also nSi-based photoanodes, demonstrating hole transport through the TiO_2, which is a seeming contradiction considering its n-type conductivity arising from oxygen vacancies. Nevertheless, the photo-excited holes are transported through the TiO_2, arriving at the water oxidation catalyst on the surface where the oxidative reaction takes place. For an ultrathin TiO_2 layer (< 2 nm), a direct tunneling mechanism was proposed by McIntyre and co-workers, as depicted in Figure 5-1a.[178,179] This tunneling mechanism is also possible with other ultrathin insulators such as Al_2O_3 and SiO_2,[180] however, is not able to explain the hole transfer through a thicker TiO_2 layer. Hu *et al.* proposed a mechanism where holes can be transported through a band of defect states deep in the bandgap of the TiO_2 (Figure 5-1b).[53,181] Mei *et al.*, however, demonstrated that crystalline TiO_2 can also be used as a protection layer for photoanodes (Figure 5-1c).[118] It should be noted that in contrast to the Hu *et al.* study, Mei *et al.* fabricated the TiO_2 by reactive sputtering, and a Ti metal layer at the interface of the Si and TiO_2 ensured an ohmic contact.

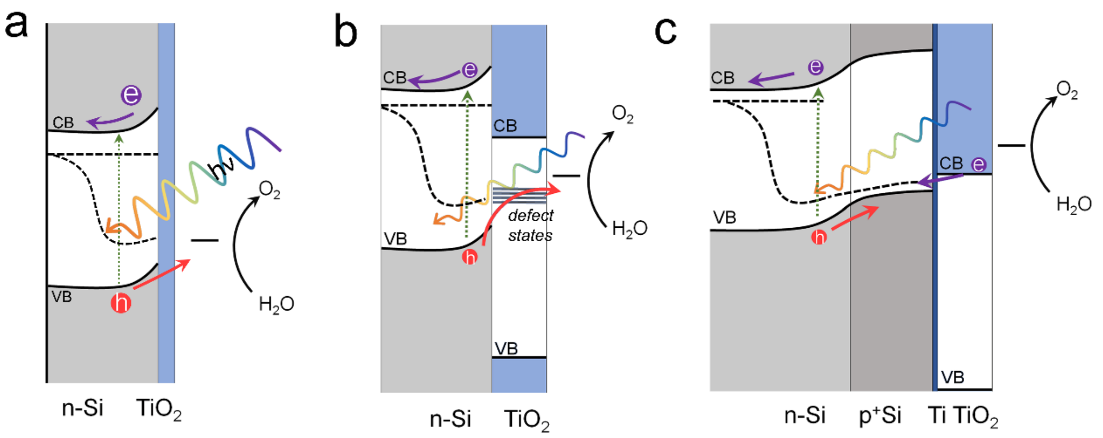

Figure 5-1 Three possible mechanisms for the “hole-leaky” property of TiO_2. (a) A thin tunnelling TiO_2 layer; (b) holes transfer through defect states; (c) electron transfer through the conduction band due to strong band bending in the TiO_2.

We sought to clarify whether such a conduction band mechanism is also operative in ALD-TiO_2 protected photoanodes in the absence of the Ti metal layer.

We also hypothesized that it should be possible to distinguish between the conduction band model and the defect-state model by analyzing the thickness-dependent resistances of the TiO_2 layer and interfaces. The defect states mediated hole transport in amorphous TiO_2 is assumed to be based on a “hopping” transport mechanism, occurring in filled defect states (Ti^{3+}) related to O vacancies and other impurities such as N and C species.[176] The hole hopping rate strongly depends on the distance between Ti^{3+} sites.[182] Compared to electron transport in the conduction band, the hole hopping rate inside the defect band should be much slower and therefore show an increased resistivity.[182,183] Thus, we hypothesized that R_{TiO2} ought to exhibit a clear thickness dependence if the defect states mechanism were operative. We therefore studied the charge transport in the TiO_2 protective layer by varying the thickness of the TiO_2 layer in the range of 50 to 170 nm.

5.2 Structural characterization of the ALD-TiO_2

The filled defect states in the mid-gap region is revealed from the X-ray photoemission valence spectrum (Figure 5-2a and b).[53,184] The defect band features of the TiO_2 layer was not observed after annealed in air (550℃, 2 h). This is in good agreement with previous analysis on oxygen deficient TiO_2.[185] Moreover, Figure 5-2c clearly shows that there is no Ti(0) present on the surface (which could be mistaken for a defect band due to the emergence of a fermi edge in the VB spectra). Moreover, the Ti(III) signal is significantly reduced after annealing, indicating further oxidation of the specimen and filling of oxygen vacancies.

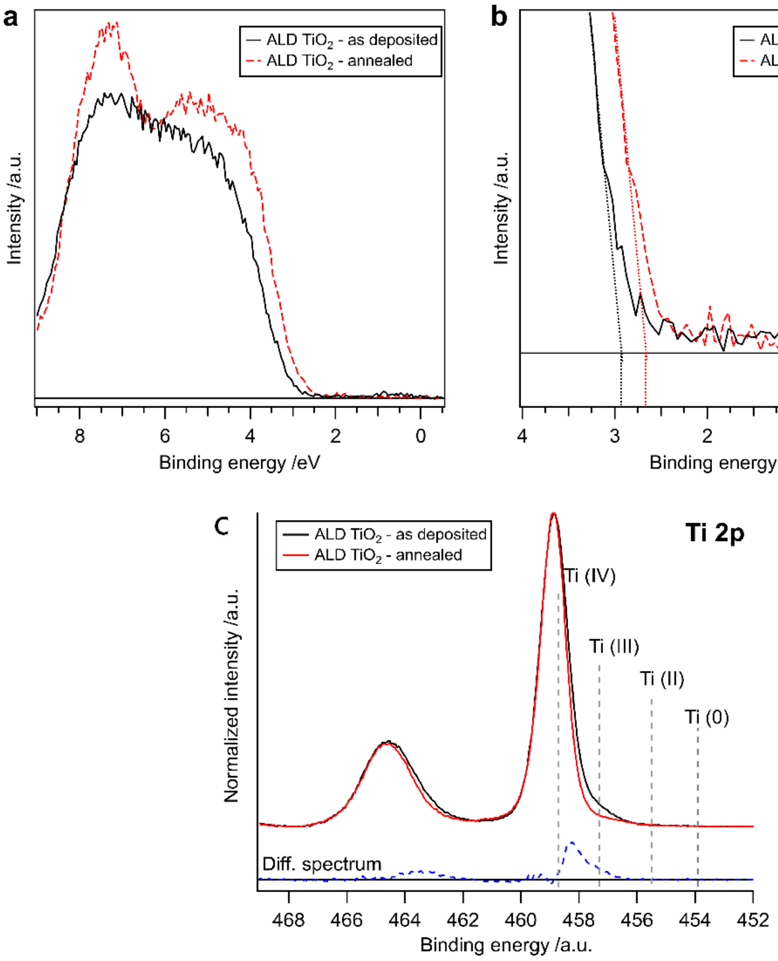

Figure 5-2 Valence band study of ALD-TiO_2 (red) and annealled TiO_2 (blue). (b) the zoom-in view. (c) Ti 2p spectra.

5.3 Thickness dependency of the R_{TiO2}

Fig. S7 shows that thicker TiO_2 does not lead to a significantly decreased FF in the J-V curve. Figure 5-3b exhibits a similar potential dependence of R_{TiO2} extracted from these samples, and R_{TiO2} values do not show a clear thickness dependence over the whole potential range, which is indicative of a transport through the conduction band.

For comparison, $pn^+Si/TiO_2/Pt$ photocathode with various TiO_2 thickness were investigated, where electron transport in the conduction band of TiO_2 is not controversial. The thickness independence of R_{TiO2} is apparent in Figure 5-4. The observed features of R_{TiO2} show clear similarity with those in the $np^+Si/TiO_2/Ni$ photoanode system, which is again an indication for the conduction band mechanism of the “hole-leaky” TiO_2 in the photoanode, even though the defect states in TiO_2 are present.

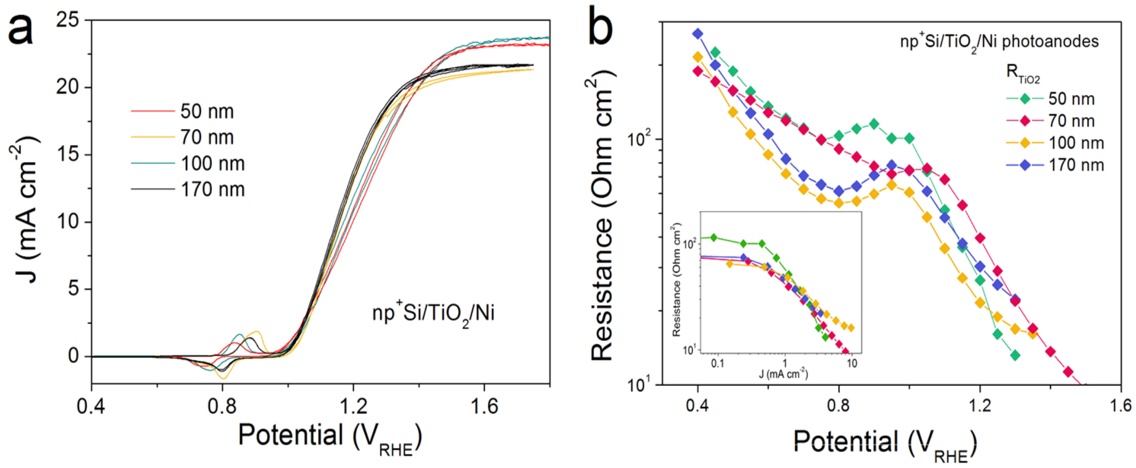

Figure 5-3 (a) CVs of $np^+Si/TiO_2/Ni$ photoanodes with various TiO_2 thickness. (b) R_{TiO2} Thickness dependence. Inset is the R_{TiO2} as a function of the photocurrent density.

Above we studied the charge transport inside the TiO_2 layer, where a conduction band mechanism has been proposed to interpret the "hole-leaky" property of TiO_2. In the following, we analyse the charge transfer across the interfaces. Two interfaces are involved for the $np^+Si/TiO_2/Ni$ configuration, p^+Si/TiO_2 and TiO_2/NiCat.

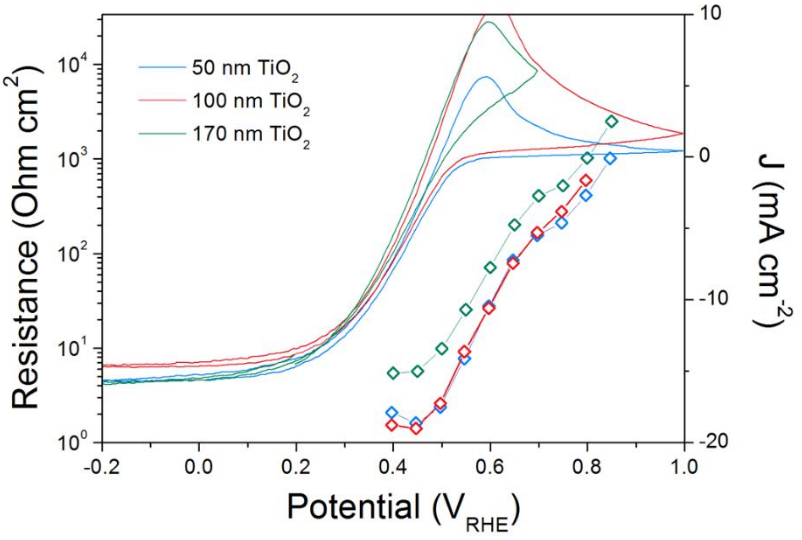

Figure 5-4 CVs and R_{TiO2} values measured from $pn^+Si/TiO_2/Pt$ photocathodes with different TiO_2 thickness.

5.4 The p^+Si/TiO_2 interface

The DWE technique, allowing *in-situ* surface potential sensing, was applied to study the interface properties. A stepwise chronoamperometric measurement was carried out whereby the potential of V1, equal to E_f(nSi), stepped towards more positive potential, and both the front contact V2 and the photocurrent were simultaneously recorded. V2 was equal to either the E_f(p^+Si) in an np^+Si/Ni photoanode or the E_f(TiO_2) in an np^+Si/TiO_2/Ni photoanode. As can be observed in Figure 5-5, E_f(TiO_2) and E_f(p^+Si) exhibit a very similar trend except for a slight deviation (~50 mV).

The change of V2 with respect to the V1 potential is typical of a buried junction photoelectrode, reported in our previous work.[186] At less positive V1, such as 0.5 or 0.6 V_{RHE}, V2 is not positive enough to drive water oxidation. ΔV values remain constant and equal to V_{oc}. As soon as V2 is slightly more positive than the $E(O_2/H_2O)$ (note that the overpotential of the NiCat must be accounted for), water oxidation is thermodynamically allowed, and electrons flow from the electrolyte/NiCat into the TiO_2 layer, accompanied by the generation of O_2 gas. The ΔV value begins to shrink as the O_2-evolving photocurrent increases and the E_f to the

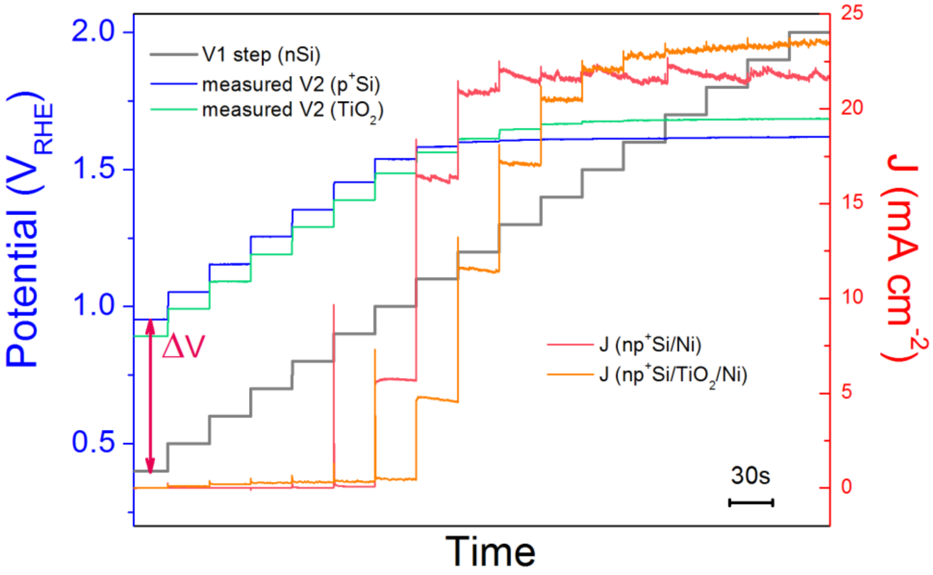

Figure 5-5 E_f(p^+Si) and J values of np^+Si/Ni; E_f(TiO_2) and J values of np^+Si/TiO_2/Ni photoanode with stepwise controlled V1 E_f(nSi) under one sun illumination. Each V1 step lasts 30 s.

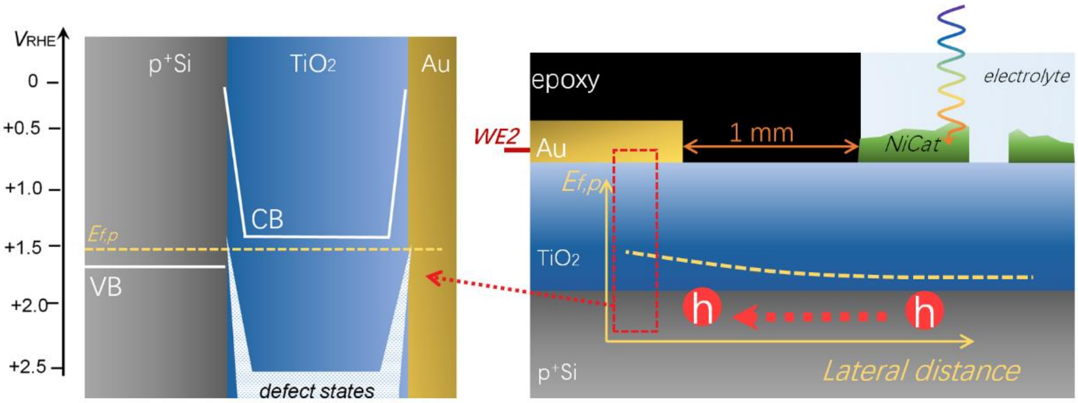

Figure 5-6 Schematic illustration of the quasi Fermi level of holes ($E_{f,p}$), sensed by WE2. The dashed red marking shows the region where band bending at the Si/TiO_2/Au interfaces is depicted (on the left)

electrolyte is pinned by the redox potential of the O_2 evolution reaction. The moment V1 reaches the same value as V2, the buried np^+ junction is at the short-circuit condition. Finally, as the photocurrent becomes saturated due to the photon flux and recombination limitation, V2 reaches a steady value independent of V1. The reverse bias across the np^+ junction becomes stronger as the controlled V1 level increases to more positive potentials.

Figure 5-6 depicts the architecture of the electrode as well as the band diagram at the contact of the second working electrode. This surface contact is remote from the actual voltage

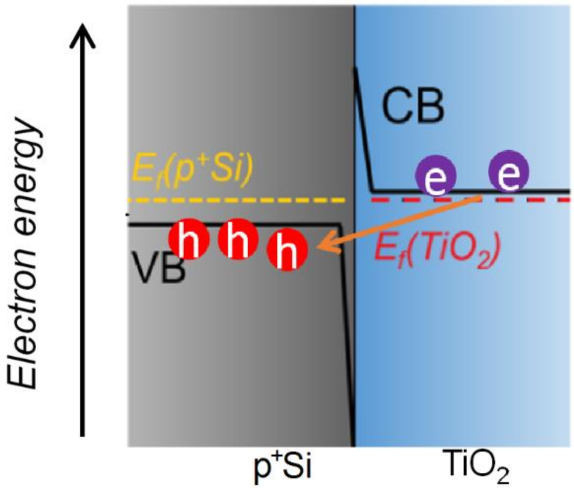

Figure 5-7 Band diagrams and charge transfer processes at the p^+Si/TiO_2 interface. Due to the large doping density in both p^+Si and TiO_2, then depletion regions are very narrow, in a range of few nm.

generating part of the photocathode and covered with thick epoxy (~1 mm from the active area and effectively in the dark, even while illuminating the active area), and is simply sensing the potential V2 with no current flow, implying a standard equilibration of the Fermi levels across the Si/TiO_2/Au interfaces. As no holes could be sustained in the defect band under this open-circuit condition, WE2 is sensing the Fermi level of the electrons (the majority carriers) in the TiO_2, which is situated very close to the conduction band edge due to the high donor density (See section 4.3). Equilibrium of the TiO_2 with the underlying p^+Si is then attained via band bending. Both p^+Si and TiO_2 layers are highly doped, and as a result, the space charge region in the junction is narrow enough for efficient electron tunneling (Figure 5-7). In such a situation, there is nearly no barrier for electrons entering p^+Si valence band from the TiO_2 conduction band.

5.5 The TiO_2 /NiCat/electrolyte interface

As is evident from Figure 5-5, the conduction band of TiO_2 becomes even more positive than the thermodynamic water oxidation potential. The onset potential for the O_2 evolution of the np^+Si/TiO_2/Ni photoanode is around 1.1 V_{RHE}, when $E_f(TiO_2)$ is 1.6 V_{RHE}. Notably, 1.6 V_{RHE}

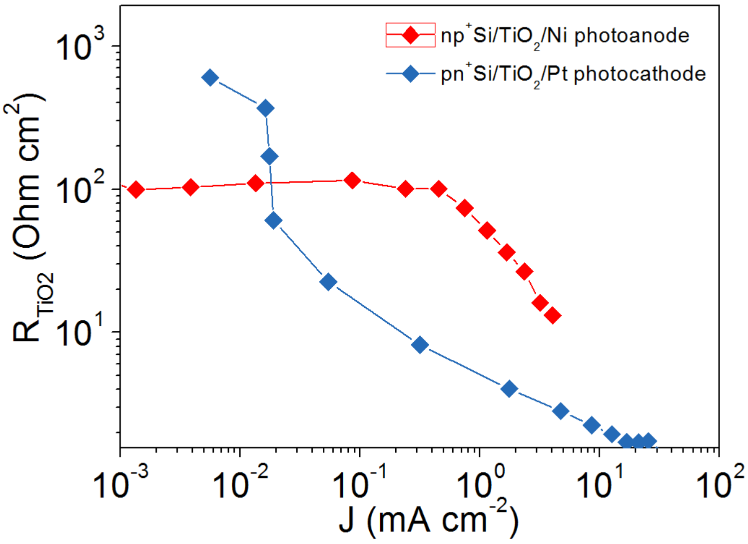

Figure 5-8 Comparison of R_{TiO2} (vs. photocurrent density) values obtained from the np^+Si/TiO_2/Ni photoanode and the pn^+Si/TiO_2/Pt photocathode. ALD-TiO_2 thickness is 50 nm. The photocurrent density values used here were the mean value of each potential step during the PEIS measurements.

is also the onset potential of the J-V2 curve in Figure 4-7c. The transition from an effective open circuit condition (at potentials where V2 is not positive enough to oxidize water) to potentials where water oxidation occurs shows a smooth trend of the TiO_2 Fermi level, analogous to the photocathode case,[186] and a transport through defect states need not be invoked. Our observations are in accordance with the description of the conduction band mechanism by Mei *et al.*, where the electrons are generated from the water oxidation process.[118] Electrons cannot enter the TiO_2 conduction band until the barrier of TiO_2/electrolyte and catalyst overpotential are overcome. This is also true for photocathodes. The barrier of TiO_2/electrolyte must be overcome first, then electrons can enter the electrolyte solution and reduce protons. However, R_{TiO2} exhibits very different values in the prior-to-onset potential region for the photoanode and photocathode. Generally, under operational conditions, the R_{TiO2} is lower for the photocathode case since we expect a lower barrier to the electrolyte (see Figure 5-8). On the other hand, in the photocathode case, R_{TiO2} varies from nearly 10^3 Ohm cm^2 in the prior-to-onset potential range, while in the photoanode case, R_{TiO2} only shows 100 Ohm cm^2 in the near-zero current region. This suggests that the electron transfer still occurs across the TiO_2 layer even in the prior-to-onset potential. We attribute this phenomenon to the ion-permeable property of NiCat. Many researchers have demonstrated that NiCat plays a role of so-called "hole-collector" as the catalyst in photoanode.[169,187] Holes are first collected and oxidize NiCat.

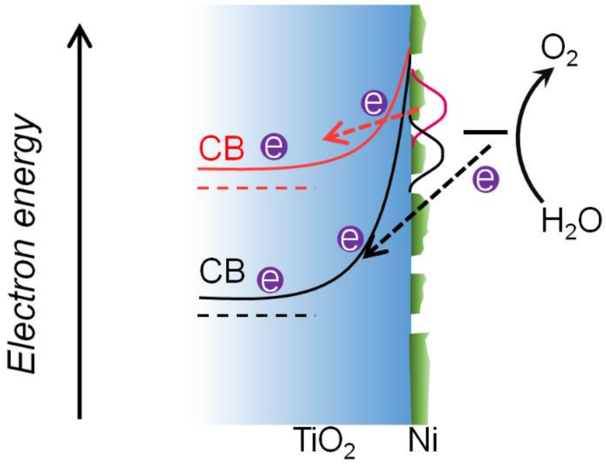

Figure 5-9 Band diagram and charge transfer processes at the TiO_2/NiCat/electrolyte interface. Due to the large doping density in TiO_2, then depletion region in TiO_2 is very narrow, in a range of few nm.

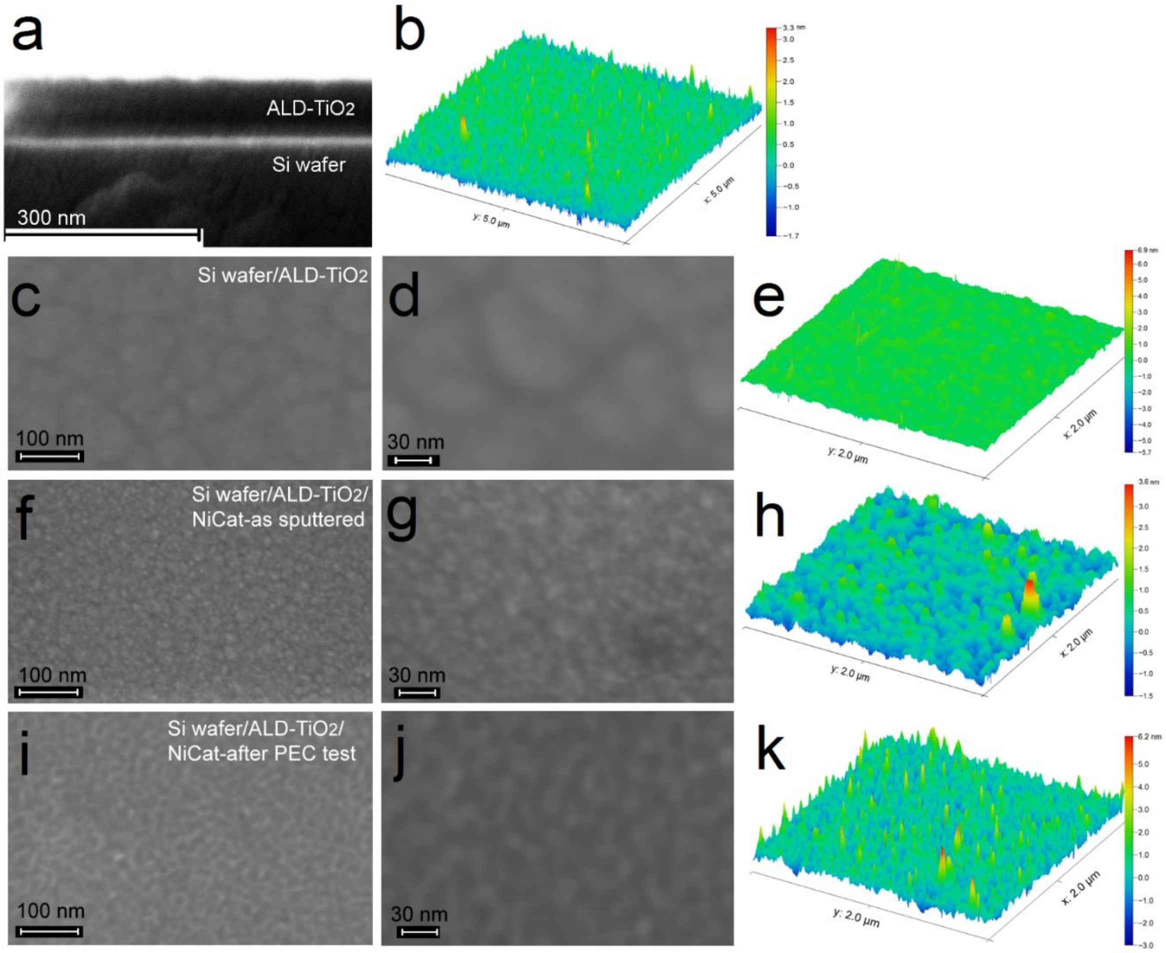

Figure 5-10 Morphology of the ALD-TiO_2 layer on Si wafer: (a) the cross-section SEM image, (b) the 3D AFM topography image of the TiO_2 surface within a larger area (5.0 µm × 5.0 µm), (c) and (d) top-view SEM images, (e) the 3D AFM topography within a small area (2.0 µm × 2.0 µm). The ALD technique guarantees the excellent flatness of the TiO_2 layer, with thickness difference no more than 1 nm. Morphology of the as-sputtered NiCat on TiO_2: (f) and (g) top-view SEM images, (h) the 3D AFM topography image with an area of 2.0 µm × 2.0 µm. The NiCat layer is a non-continuous layer with an island mophology. The height of most NiCat islands is ~ 2 nm. Morphology of NiCat on TiO_2 after PEC measurements: (i) and (j) top-view SEM images, (k) the 3D AFM topography image with an area of 2.1 µm × 2.1 µm. The island mophology of NiCat is remained after all PEC measurements, but in addition, the height becames~ 1 nm bigger due to the oxidation of metallic Ni to Ni hydroxide and oxyhydroxide.[193,194]

When the NiCat energy level is sufficiently positive, holes enter the electrolyte solution and

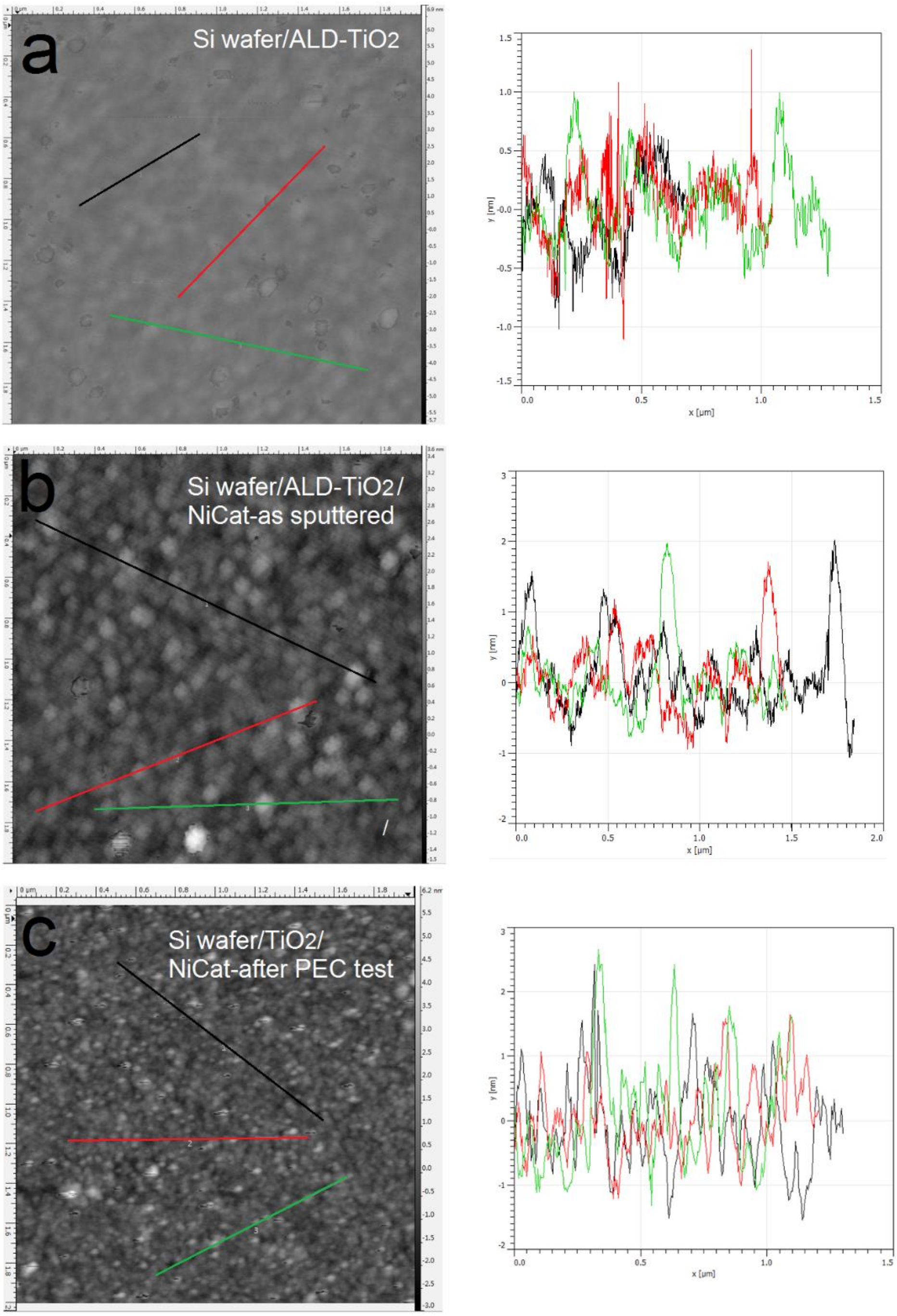

Figure 5-11 AFM topography images and height profiles of (a) the ALD-TiO_2 layer on Si wafer, (b) the as-sputtered NiCat on TiO_2 and (c) the NiCat on TiO_2 after PEC test. Again, the ALD-TiO_2 surface is very flat, suggests that the layer is conformal. The as-sputtered NiCat is in island mophology, with a height of ~2 nm. After PEC test, the NiCat is expanded.

oxidize water to oxygen. Similarly, in the $np^+Si/TiO_2/Ni$ photoanode, in the prior-to-onset potential region, electrons from NiCat enter TiO_2 conduction band and NiCat is oxidized, resulting in nearly zero net photocurrent. When photocurrent rises, electrons generated by water oxidation process enter TiO_2 conduction band (Figure 5-9). In comparison, Pt is not ion-permeable and no electrons can transfer into the TiO_2 and be collected in Pt catalyst until cathodic photocurrent rises, which is why R_{TiO2} shows extremely high values in the prior-to-onset potential region in the $pn^+Si/TiO_2/Pt$ photocathode. Moreover, it is important to note that the morphology of the NiCat plays a crucial role in the solid/liquid interface.[24] The NiCat in our work deposited by sputtering was nominally 2-nm-thick, however, the layer is neither conformal nor continuous and has an island morphology, as confirmed by scanning electron microscopy (SEM, Zeiss Supra 50 VP) and atomic force microscopy (AFM, Asylum Research) (Fig. 5-10 and 5-11). Thus, the TiO_2 directly contacts the electrolyte solution, which pins the band edge of the TiO_2. In the presence of the Ni catalyst and at high applied bias (large band bending), electrons from the electrolyte solution are thus able to tunnel through the narrow depletion region and enter the TiO_2 conduction band due to the high doping density of TiO_2, as illustrated in Figure 5-12.[12]

5.6 nSi/TiO_2/Ni photoanode

The conduction band mechanism has been implicated with the $np^+Si/TiO_2/Ni$ photoanode system in the above discussion. Next, we wished to study the charge transfer across a non-homojunction system, the $nSi/TiO_2/Ni$ photoanode, wherein the nSi/TiO_2 interface is significantly different to the p^+Si/TiO_2 interface. In the $nSi/TiO_2/Ni$ photoanode, the nSi/TiO_2 interface cannot be seen as an ohmic contact due to the non-degenerate nSi.

5.6.1 The nSi/TiO_2 junction

The n-Si wafers used for nSi/TiO_2 Ni photoanodes were double-polished and phosphorous-doped with a dopant density of 10^{16} cm^{-3} (Sil'tronix). In terms of nSi/TiO_2 DWE, WE2 is the sputtered 20 nm Au layer attached onto the TiO_2 surface, as drawn in Figure 5-12 (left). A photovoltage of 90 mV was measured by the DWE technique (Figure 5-12, right). The buried junction behaviour of nSi/TiO_2 interface was demonstrated by the stepwise DWE measurements results. As can be seen in Figure 5-13, ΔV keeps a similar value of 85 mV in the prior-to-onset potential region. With photocurrent rising, ΔV starts to shrink. $E_f(TiO_2)$ becomes constant as the photocurrent becomes saturated. In the dark condition, $E_f(nSi)$ and $E_f(TiO_2)$

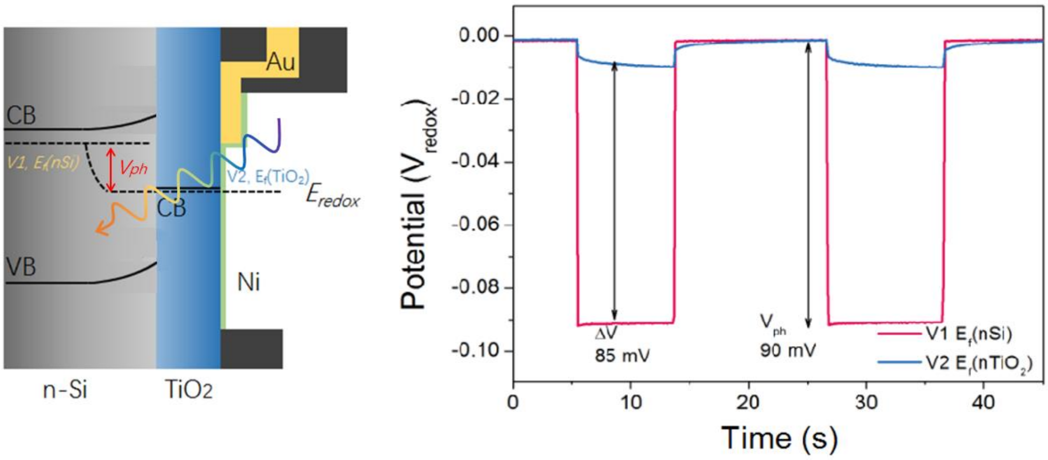

Figure 5-12 Determination of the V_{ph} generated by nSi/TiO_2 junction. Left: schematic of the band diagram of an nSi/TiO_2/Ni DWE. V1 is the back contact potential, controlling E_f(nSi); V2 is attached to the TiO_2, controlling the E_f(TiO_2). Right: V_{ph} determination in a $[Fe(CN)_6]^{4-}$/$[Fe(CN)_6]^{3-}$ redox solution. Both V1 and V2 are kept at open circuit.

are equilibrated with the solution redox potential. Hence V1 and V2 values are close to zero vs. the redox couple the in dark. Under illumination, photovoltage is generated. The nSi quasi Fermi level for holes and E_f(TiO_2) are equilibrated with the solution redox, while nSi quasi Fermi level for electrons (V1) is shifted up. This is why V1 shows a large negative value and V2 doesn't change to much under illumination. The change of V1 is the V_{ph}, determined as 90

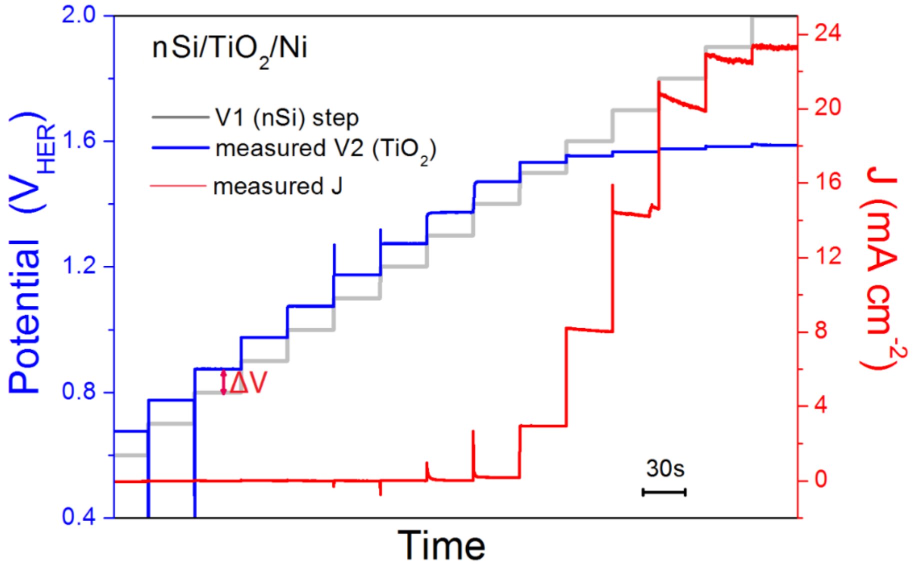

Figure 5-13 E_f(TiO_2) and J values and J values of nSi/TiO_2/Ni photoanode with stepwise controlled V1.

mV. The ΔV is 85 mV. The tiny difference can be due to the contact problems.

The built-in voltage (V_{bi}) of the nSi/TiO_2 junction was conducted with a similar Mott-Schottky method as described above but using a two-electrode mode under dark condition (without electrolyte solution). One of the electrodes was connected to the back contact of the nSi/TiO_2 electrode. The other one was connected to the front contact, which was a 20 nm-thick Ni metal layer sputtered onto the TiO_2 surface. A V_{bi} of 320 mV was measured with the Mott–Schottky method (Figure 5-14). We note that both the photovoltage and built-in voltage are smaller compared to the values in Hu *et al.*'s work, which are 390 and 700mV, respectively.[188] This considerable difference can arise from the different experimental procedure. In our system, the TiO_2 layer was immediately deposited after the HF-etching in order to avoid the formation of surface SiO_2 formation. In Hu *et al.*'s work, the HF-etched Si wafers were subsequently immersed in $H_2O/HCl/H_2O_2$ solution (RCA-2 Treatments), which made the oxide layer regrow.[189,190] Presumably, this ultrathin SiO_2 layer either passivates surface states or unpins nSi so that larger photovoltage can be achieved. Nevertheless, this difference to previous work does not affect the following analysis

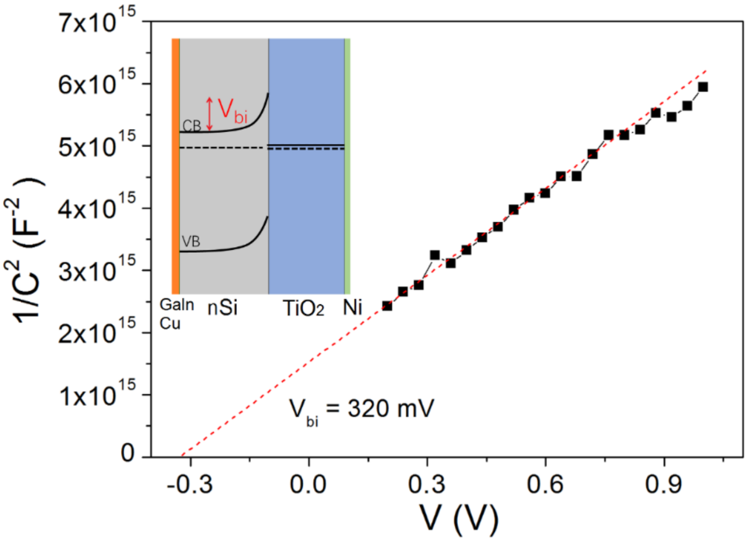

Figure 5-14 Mott-Schottky plot of the nSi/TiO_2 electrode. The capacitance data are obtained from electrical impedance spectroscopy with two-electrode mode in dark condition. The inset is the structure of the electrode.

5.6.2 Charge carrier process

PEIS measurements for the nSi/TiO_2/Ni photoanode were carried out under 0.1 sun illumination to increase the signal to noise ratio. Fitting details can be found in Figure 5-15.

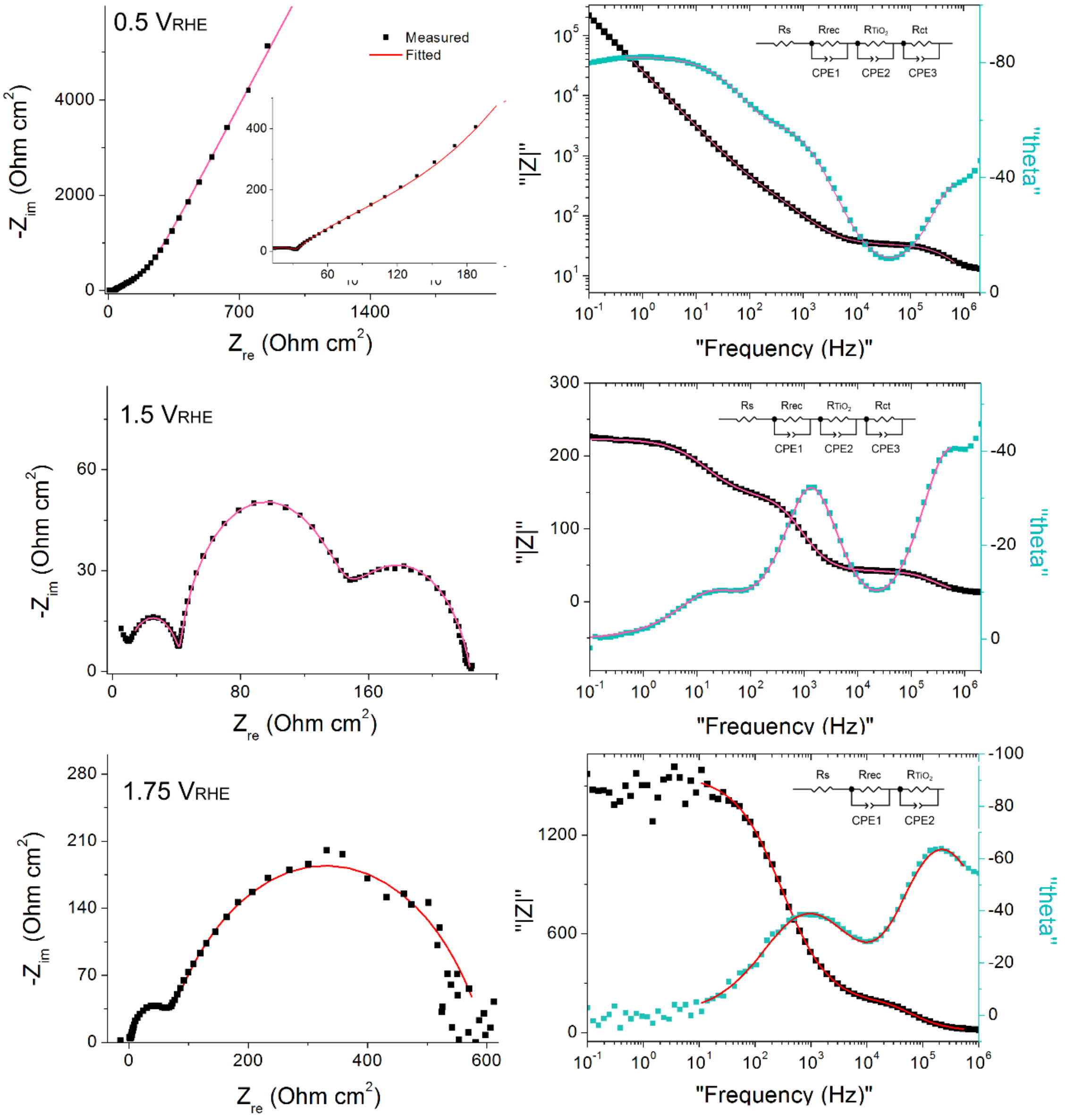

Figure 5-15 Nyquist and Bode plots and corresponding fitting of an nSi/TiO_2/Ni photoanode at back contact potentials of 0.55, 1.5 and 1.75 V_{RHE} under one sun illumination. Equivalent circuit models are given as well. R_s is the series resistance raised by the electrolyte solution. R_{rec} is the overall resistance to charge recombination taking place in the nSi. R_{TiO2} is the overall resistance of charge transfer through the TiO_2 layer. R_{ct} is associated with the O_2-evolving process at the Ni catalyst.

Similarly, R_{rec}, R_{TiO2} and R_{ct} were extracted. Figure 5-16a presents the CV of the nSi/TiO_2/Ni photoanode as well as the voltage–dependent values of R_{rec}, R_{TiO2} and R_{ct}. Due to the limited V_{ph} generated by nSi/TiO_2, a much later onset potential (1.5 V_{RHE}) was observed than for the np$^+$Si/TiO_2/Ni junction. R_{rec} values are low and constant and continue to increase as the photocurrent rises. R_{ct} mirrors the CV, exhibiting large values that rapidly decrease after onset potential. Figure 5-16b shows that the thickness of the TiO_2 layer does not affect the fill factor of the J-V curve. R_{TiO2} does not show a thickness dependence, suggesting that the conduction band mechanism is also true in the nSi/TiO_2/Ni photoanode system.

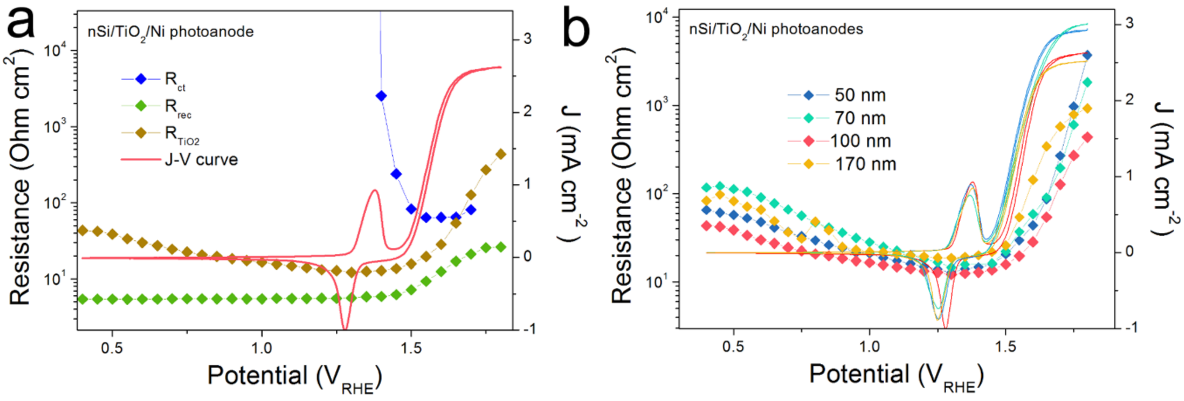

Figure 5-16 Resistances and photocurrent densities (J) versus the back contact potential for a nSi/TiO_2/Ni photoanode. (b) CVs and R_{TiO2} values measured from nSi/TiO_2/Ni photoanodes with different TiO_2 thickness.

However, unlike the downward trend in np$^+$Si/TiO_2/Ni and pn$^+$Si/TiO_2/Pt, R_{TiO2} in nSi/TiO_2/Ni shows a significant increase as photocurrent increases. This indicates a hidden process that hinders the charge transfer across the nSi/TiO_2 interface. We attribute this limitation to the defect states in TiO_2. Since E_f(TiO_2) becomes constant, as shown in the above stepwise DWE measurements, the reverse bias between nSi and TiO_2 is increasingly stronger. As illustrated in Figure 5-17, when the Si Fermi level is more positive than the TiO_2 defect states, electrons from the TiO_2 conduction band can be trapped before entering the Si valence band. One possible trapping mechanism is that electrons at the TiO_2 conduction band need to fill the empty trap states before entering Si valence band (i.e. before recombining with photo-excited holes in the nSi valence band). This trapping effect is growingly significant as the E_f(nSi) moves down, leading to slower charge kinetics and increased R_{TiO2} values.

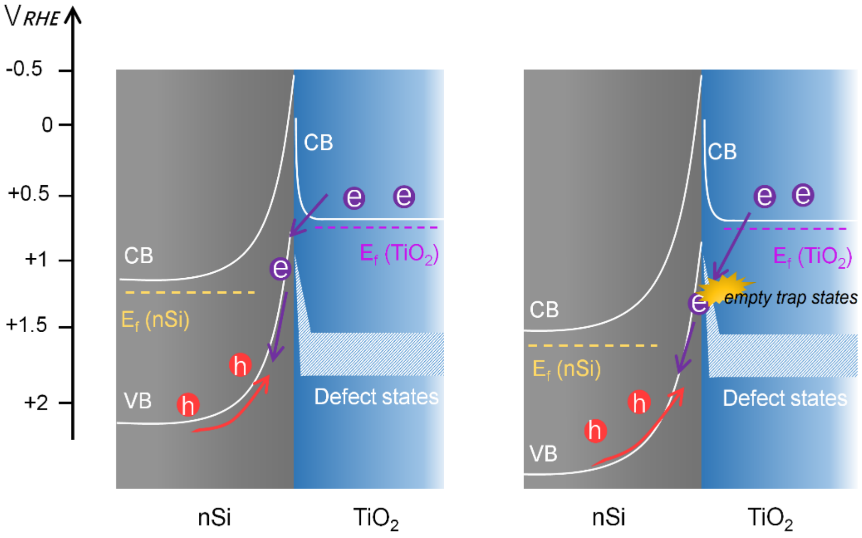

Figure 5-17 Band diagram and charge transfer process at the nSi/TiO$_2$ interface with photogenerated holes. The doping density of nSi is much smaller so that the depletion region width in nSi is very large compared to that in TiO$_2$ (in the range of hundreds of nm), resulting in a rectifying junction.

5.7 Conclusions

In summary, we utilized PEIS and DWE techniques to study the “hole-leaky” property of the ALD-TiO$_2$ and a detailed picture of the charge transfer through the multilayer structured photoanodes was obtained. For both R_{TiO2} of np$^+$Si/TiO$_2$/Ni and nSi/TiO$_2$/Ni photoanodes, R_{TiO2} did not show a clear thickness dependence, and the energetic position of the conduction band during operation as detected by the DWE technique suggests that the “hole-leaky” property of TiO$_2$ can be explained by charge transport in the conduction band, in spite of the presence of the defect states in TiO$_2$. R_{TiO2} behaved differently in the np$^+$Si/TiO$_2$/Ni and nSi/TiO$_2$/Ni photoanode. In the np$^+$Si/TiO$_2$/Ni photoanode, R_{TiO2} showed a reduction/decrease over the whole potential range as the p$^+$Si/TiO$_2$ interface behaves like an ohmic junction. In the nSi/TiO$_2$/Ni photoanode, R_{TiO2} increased as the photocurrent increases, which was interpreted by trapping in the defect states present at the interface of the nSi/TiO$_2$.

6 Conclusions and Perspectives

6.1 Conclusions

This dissertation demonstrates the *operando* electrochemical characterization of PEC devices with multilayer structures. In particular, the DWE techniques and PEIS are applied to obtain a deep understanding of both interfacial energetics and charge kinetics, which is poorly realized by the traditional 3-electrode PEC measurements. Meanwhile, we also conducted our analysis under realistic photo-electrolysis conditions and this is a primary advantage compared to other *operando*/*in situ* methods based on spectroscopic and scanning-probe techniques.

Chapter 2 introduced the DWE technique which enables the *in situ* surface potential probing under operation condition. Here we developed a "buried" second working electrode that is remote from the electrochemical active area, aiming to avoid interfering with the actual charge carrier process at the electrode/solution interface. We took the $pn^+Si/TiO_2/Pt$ electrode as a model system. Through the surface potential probing, the photovoltaic performance of the underlying junction (the J–ΔV curve) could be deconvoluted from the overall PEC performance (the J-V1 curve). The PEC performance was mainly determined by the buried p-n Si homojunction, therefore, the J–ΔV curve could be seen as the best possible J-V1 curve and the FF difference between these two curves could be used to examine the TiO_2/Pt interface. Considering this, we examined two Pt catalyst with different morphologies, nano-particles and film, and the FF loss for the Pt film sample was significantly smaller than the sample with Pt particles. Additionally, the DWE technique could be used to determine the actual overpotential of an H_2-evolving catalyst, which is MoS_x catalyst with 150 mV overpotential in our work. Finally, by comparing the J-ΔV curves before and after long term measurements, we could distinguish between the buried semiconductor degradation and degradation of the surface catalyst. Regarding the $pn^+Si/TiO_2/Pt$(ed) photocathode, p-n Si junction was proved to be stable and the PEC performance degradation has been attributed to the detachment of the Pt catalyst.

Chapter 3 showed the good universality of the DWE technique. We applied the DWE technique to several systems, including $Cu_2O/Ga_2O_3/TiO_2/Pt$, $S\text{-}Sb_2Se_3/TiO_2/Pt$ and p-Si/PA/TiO_2/Pt photocathodes. Similarly, J-ΔV curves were revealed and the related junction behavior were studied. For the $Cu_2O/Ga_2O_3/TiO_2/Pt$ photocathode, the large V_{oc} generated by the Cu_2O/Ga_2O_3 junction was quantified. The instability and the "restorable V_{oc}" of the junction was observed and discussed. For the S-$Sb_2Se_3/TiO_2/Pt$ photocathodes, we explained the reason for the enhanced PEC behavior of Sb_2Se_3 photocathode with a post-sulfurization process. In terms of the p-Si/PA/TiO_2/Pt photocathode, we learnt that the addition of the PA dipole layer enhanced the V_{oc} generated by the p-Si/ TiO_2 and the onset potential of the J-V1 curve thus positively shifted by 0.3 V. Finally, the stability of the PA layer was investigated and adding the PA layer did not affect the stability of the p-Si/TiO_2 junction.

To summarize the portion of the DWE work in Chapter 2 and 3, we gained a deep understanding in the individual behavior of the buried junction and the surface catalyst, the TiO_2/catalyst interface and the degradation mechanism for a photocathode. The above work has been published as "*Operando* deconvolution of photovoltaic and electrocatalytic performance in ALD-TiO_2 protected water splitting photocathodes" in *Chemical Science*.[186]

Chapter 4 mainly detailed the charge carrier processes in TiO_2 protected water splitting electrodes by PEIS. The targets included the $np^+Si/TiO_2/Ni$ photoanode and the $pn^+Si/TiO_2/Pt$ photoanode. Through the potential dependency and frequency domain, several charge carrier processes have been identified in the form of a resistance, such as R_{rec} (electron-hole pairs recombining in the semiconductor part), R_{TiO2} (charges from the semiconductor transferring through the TiO_2 layer and arriving at the surface catalyst) and R_{ct} (water oxidation occurring at the surface catalyst). We paid special attention to the property of R_{TiO2} that is raised by introducing the TiO_2 protective layer, and applied a surface contact-controlled PEIS for a comparison study. The R_{TiO2} was present in both photoanode and cathode cases and this could be a clue for understanding the "hole-leaky" property of the TiO_2.

In Chapter 5, we attempted to distinguish the "conduction band mechanism" and the "defect states mechanism" for elucidating how the photo-excited holes transfer though the n-type TiO_2 layer. The R_{TiO2} of the $np^+Si/TiO_2/Ni$ photoanode did not show a clear thickness dependence, indicating the conduction band mechanism. A stronger indication of the conduction band mechanism was given by the DWE stepwise measurements. The energetic position of the conduction band during operation was detected by the surface contact and suggested that it was electrons that transfer at the TiO_2 conduction band rather than hole transfer via mid-gap defect states in TiO_2. Furthermore, we provided a detailed picture of charge transfer across the $np^+Si/TiO_2/Ni$ photoanode: in the prior-to-onset potential region, electrons from NiCat enter TiO_2 conduction band and this results in the activation of NiCat, which is oxidized. When the water oxidation overpotential is overcome, photocurrent rises and electrons generated by water oxidation process enter the TiO_2 conduction band. The p^+Si/TiO_2 interface behaves like an ohmic junction and electrons enter the p^+Si valence band by recombining with holes. Finally, we studied the charge carrier process of the $nSi/TiO_2/Ni$ photoanode. Again, the conduction band mechanism was indicated to be tenable. However, R_{TiO2} behaved differently and showed an increasing trend as the photocurrent increases, which was interpreted by trapping in the defect states present at the interface of the nSi/TiO_2.

The work in Chapter 5 and 6 was a systematic investigation of the charge carrier process inside TiO_2-protected photoanode and photocathode, by using PEIS and the DWE technique. Particularly, the "hole-leaky" property of ALD-TiO_2 has been interpreted. These works have been published as "*Operando* electrochemical study of charge carrier processes in water splitting photoanodes protected by atomic layer deposited TiO_2" in *Sustainable Energy & Fuels.*[191]

6.2 Perspectives

Although much progress has been made, there remain some loose ends that should be cleared up with further research. This brings me to a series of work that could be done in the future, listed as follows:

(1) *The unclear "restorable V_{oc}" behavior of the Cu_2O/Ga_2O_3 junction*. In the section of 3.14, there is no hard evidence that the restorable V_{oc} is related to the Cu vacancies diffusion. To fully understand this phenomenon, there are two main works that could be done. One of them is using capacitance transient measurements to reveal the Cu vacancies diffusion process in various Cu_2O-based junctions, such as Cu_2O/TiO_2, Cu_2O/Ga_2O_3 and Cu_2O/AZO junctions.[157] The other one is to study the stoichiometric effect by fabrication Cu_xO/Ga_2O_3 ($1<x<2$) junction-based photocathodes. The concentration of Cu vacancies can be quantified and the Cu vacancies diffusion thus could be tailored. After fully understanding the restorable V_{oc}, we could utilize this property in realistic long term operation of Cu_2O-based PEC or PV devices. The small V_{oc} degradation after a day's work may not be a serious problem owing to this "self-

healing" capacity of Cu_2O.

(2) *The DWE technique*. In my thesis, a "remote" configuration of the front contact was applied to sense the surface potential (WE2). This raised two problems: first, the sensed potential by the WE2 is not the actual potential of the electrochemical area, as discussed in section 2.5.1, but is off by a few tens of mV. Besides, the spatial distribution of surface potential cannot be realized in this configuration, the effect of the surface roughness and morphology to the PEC performance is thus not possible to investigate. Second, the potential-sensing of WE2 was strongly dependent on the lateral conductivity of the contact layer, where the photo-excited minority carriers had to travel ~1 mm to be detected by WE2. This limits the use of the target systems, especially with relatively small doping density.

One promising technique is potential-sensing AFM (PS-AFM), which simultaneously enables surface topography and localized potential sensing.[86] Therefore, the real electrochemical potential of TiO_2 protective layer, the surface catalyst and even the quasi Fermi level of the minority carriers can be directly monitored. All the information will contribute to a much more refined understanding of interfacial energetics. Plus, the surface potential map allows the spatial-resolved study, such as the effect of catalyst particle size and orientation of the multicrystalline semiconductor.

(3) *The stability test of a photoelectrode.* So far, the stability test in this thesis was still traditional chronoamperometry except for the *in situ* surface potential sensing. However, to examine the stability of a buried junction, the band bending condition needs to be considered. When V1 is fixed at 0 V_{RHE}, the buried junction will be under strong bias, as shown in Figure 2-8, which is under much stronger band bending than the maximum power point (MPP) for a solar cell. Therefore, I propose a more reasonable stability test process. The first step is to find the MPP of the J-ΔV curve and the corresponding V1, named $V1_{MPP}$. Next step is still a chronoamperometry but to keep V1 at $V1_{MPP}$ rather than 0 V_{RHE} to mimic the practical photoelectrolysis under load.

(4) *PEIS*. The interpretation of charge carrier processes by PEIS is not straightforward. The Nyquist plots must be fitted with equivalent circuit models, and the equivalent circuit should have a basis in reality. Besides, it is hard to deconvolute one individual charge carrier process or interfacial property. For example, R_{TiO2} is an overall parameter and actually consists of three

different charge carrier processes: charge across the Si/TiO_2 interface, transport inside the TiO_2 and across the TiO_2/NiCat/electrolyte interface. Therefore, it is highly desirable to find an *operando* technology which enables direct investigation of interface properties. Again, PS-AFM seems promising because it enables localized surface study. With the proper surface design, the local potential of NiCat, TiO_2 and exposed Si and can be individually monitored. In this way, charge transfer across the Si/TiO_2/NiCat/electrolyte interface can be deeply characterized. Another potential technique is the transient photocurrent spectroscopy, which records the photocurrent response with the chopped illumination.[192] By fitting photocurrent decays and calculating time constants, the charge recombination and trapping properties can be studied. However, if coupling the transient measurement with the DWE technique, the "transient potential spectroscopy" could be realized. To study the potential decay behavior of each layer, more information of charge transfer through interfaces are expected to be achieved.

References

(1) Metz, B.; Metz, B. Energy Supply. In *Controlling Climate Change*; **2012**.

(2) Le Page, M. World without fossil fuels. *New Sci.* **2014**.

(3) *OECD Companion to the Inventory of Support Measures for Fossil Fuels 2018*; **2018**.

(4) Kaldellis, J. K.; Zafirakis, D. The wind energy (r)evolution: A short review of a long history. *Renewable Energy*. **2011**.

(5) Worrell, E.; Price, L.; Martin, N.; Hendriks, C.; Meida, L. O. Carbon dioxide emissions from the global cement industry. *Annu. Rev. Energy Environ.* **2001**.

(6) Meinshausen, M.; Meinshausen, N.; Hare, W.; Raper, S. C. B.; Frieler, K.; Knutti, R.; Frame, D. J.; Allen, M. R. Greenhouse-gas emission targets for limiting global warming to 2 ℃. *Nature* **2009**.

(7) Wang, W. Imaging the chemical activity of single nanoparticles with optical microscopy. *Chem. Soc. Rev.* **2018**, *47*, 2485–2508.

(8) Hosenuzzaman, M.; Rahim, N. A.; Selvaraj, J.; Hasanuzzaman, M.; Malek, A. B. M. A.; Nahar, A. Global prospects, progress, policies, and environmental impact of solar photovoltaic power generation. *Renewable and Sustainable Energy Reviews*. **2015**.

(9) BP. Energy Outlook 2019 Edition. *Bp* **2019**.

(10) Tian, Y.; Zhao, C. Y. A review of solar collectors and thermal energy storage in solar thermal applications. *Appl. Energy* **2013**.

(11) Goetzberger, A.; Hebling, C.; Schock, H. W. Photovoltaic materials, history, status and outlook. *Materials Science and Engineering R: Reports*. 2003.

(12) Yamori, W. Photosynthesis and respiration. In *Plant Factory: An Indoor Vertical Farming System for Efficient Quality Food Production*; 2015.

(13) Bard, A. J.; Fox, M. A. Artificial Photosynthesis: Solar Splitting of Water to Hydrogen and Oxygen. *Acc. Chem. Res.* **1995**.

(14) Ganesh, I. Conversion of Carbon Dioxide to Methanol Using Solar Energy - A Brief Review. *Mater. Sci. Appl.* **2011**.

(15) Dunn, S. Hydrogen futures: Toward a sustainable energy system. *Int. J. Hydrogen*

Energy **2002**.

(16) Lewis, N. S.; Nocera, D. G. Powering the planet: Chemical challenges in solar energy utilization. *Proc. Natl. Acad. Sci.* **2006**, *103*, 15729–15735.

(17) Osterloh, F. E.; Parkinson, B. A. Recent developments in solar water-splitting photocatalysis. *MRS Bull.* **2011**.

(18) Jacobsson, T. J.; Fjällström, V.; Edoff, M.; Edvinsson, T. Sustainable solar hydrogen production: from photoelectrochemical cells to PV-electrolyzers and back again. *Energy Environ. Sci.* **2014**, *7*, 2056–2070.

(19) Rothschild, A.; Dotan, H. Beating the Efficiency of Photovoltaics-Powered Electrolysis with Tandem Cell Photoelectrolysis. *ACS Energy Lett.* **2017**, *2*, 45–51.

(20) Eftekhari, A.; Babu, V. J.; Ramakrishna, S. Photoelectrode nanomaterials for photoelectrochemical water splitting. *International Journal of Hydrogen Energy*. **2017**.

(21) Kahn, A. Fermi level, work function and vacuum level. *Materials Horizons*. **2016**.

(22) Tamirat, A. G.; Rick, J.; Dubale, A. A.; Su, W. N.; Hwang, B. J. Using hematite for photoelectrochemical water splitting: A review of current progress and challenges. *Nanoscale Horizons*. **2016**.

(23) Wang, S.; Chen, P.; Yun, J. H.; Hu, Y.; Wang, L. An Electrochemically Treated BiVO4 Photoanode for Efficient Photoelectrochemical Water Splitting. *Angew. Chemie - Int. Ed.* **2017**.

(24) Le Formal, F.; Pastor, E.; Tilley, S. D.; Mesa, C. A.; Pendlebury, S. R.; Grätzel, M.; Durrant, J. R. Rate Law Analysis of Water Oxidation on a Hematite Surface. *J. Am. Chem. Soc.* **2015**.

(25) Zhang, X.; Li, H.; Wang, S.; Fan, F. R. F.; Bard, A. J. Improvement of hematite as photocatalyst by doping with tantalum. *J. Phys. Chem. C* **2014**.

(26) Spurgeon, J. M.; Velazquez, J. M.; McDowell, M. T. Improving O2 production of WO3 photoanodes with IrO2 in acidic aqueous electrolyte. *Phys. Chem. Chem. Phys.* **2014**.

(27) Gonçalves, R. H.; Leite, L. D. T.; Leite, E. R. Colloidal WO3 nanowires as a versatile route to prepare a photoanode for solar water splitting. *ChemSusChem* **2012**.

(28) Enesca, A.; Duta, A.; Schoonman, J. Study of photoactivity of tungsten trioxide (WO3) for water splitting. *Thin Solid Films* **2007**.

(29) Higashi, M.; Domen, K.; Abe, R. Fabrication of efficient TaON and Ta3N5photoanodes for water splitting under visible light irradiation. *Energy Environ. Sci.* **2011**.

(30) Seo, J.; Takata, T.; Nakabayashi, M.; Hisatomi, T.; Shibata, N.; Minegishi, T.; Domen, K. Mg-Zr cosubstituted Ta3N5 photoanode for lower-onset-potential solar-driven photoelectrochemical water splitting. *J. Am. Chem. Soc.* **2015**.

(31) Morales-Guio, C. G.; Tilley, S. D.; Vrubel, H.; Graẗzel, M.; Hu, X. Hydrogen evolution from a copper(I) oxide photocathode coated with an amorphous molybdenum sulphide catalyst. *Nat. Commun.* **2014**, *5*, 1–7.

(32) Paracchino, A.; Mathews, N.; Hisatomi, T.; Stefik, M.; Tilley, S. D.; Gr ätzel, M.; Graetzel, M. Ultrathin films on copper(i) oxide water splitting photocathodes: A study on performance and stability. *Energy Environ. Sci.* **2012**, *5*, 8673–8681.

(33) Tilley, S. D.; Schreier, M.; Azevedo, J.; Stefik, M.; Graetzel, M. Ruthenium oxide hydrogen evolution catalysis on composite cuprous oxide Water-splitting photocathodes. *Adv. Funct. Mater.* **2014**, *24*, 303–311.

(34) McKone, J. R.; Lewis, N. S.; Kelzenberg, M. D.; Turner-Evans, D.; Warren, E. L.; Walter, M. G.; Brunschwig, B. S.; Santori, E. A.; Boettcher, S. W.; Atwater, H. A.; et al. Photoelectrochemical Hydrogen Evolution Using Si Microwire Arrays. *J. Am. Chem. Soc.* **2011**, *133*, 1216–1219.

(35) Fujishima, A.; Honda, K. Electrochemical photolysis of water at a semiconductor electrode. *Nature* **1972**.

(36) Sivula, K.; Le Formal, F.; Gr ätzel, M. Solar water splitting: Progress using hematite (α-Fe 2O3) photoelectrodes. *ChemSusChem*. 2011.

(37) Chen, Z.; Jaramillo, T. F.; Deutsch, T. G.; Kleiman-Shwarsctein, A.; Forman, A. J.; Gaillard, N.; Garland, R.; Takanabe, K.; Heske, C.; Sunkara, M.; et al. Accelerating materials development for photoelectrochemical hydrogen production: Standards for methods, definitions, and reporting protocols. *Journal of Materials Research*. 2010.

(38) Weber, M. F.; Dignam, M. J. Efficiency of Splitting Water with Semiconducting Photoelectrodes. *J. Electrochem. Soc.* **1984**.

(39) Chu, S.; Li, W.; Yan, Y.; Hamann, T.; Shih, I.; Wang, D.; Mi, Z. Roadmap on solar water splitting: Current status and future prospects. *Nano Futures*. 2017.

(40) He, Y.; Hamann, T.; Wang, D. Thin film photoelectrodes for solar water splitting. *Chem. Soc. Rev.* **2019**, *48*, 2182–2215.

(41) De Souza, F. L.; Xavier, A. M.; De Carvalho, W. M.; Gonçalves, R. H.; Leite, E. R. Facile routes to produce hematite film for hydrogen generation from Photoelectro-chemical water splitting. In *Nanoenergy: Nanotechnology Applied for Energy Production*; 2013.

(42) Cox, C. R.; Winkler, M. T.; Pijpers, J. J. H.; Buonassisi, T.; Nocera, D. G. Interfaces between water splitting catalysts and buried silicon junctions. *Energy Environ. Sci.* **2013**, *6*, 532–538.

(43) Smith, W. A.; Sharp, I. D.; Strandwitz, N. C.; Bisquert, J. Energy & Environmental Science Interfacial band-edge energetics for solar fuels production. *Energy Environ. Sci. Energy Environ. Sci* **2015**.

(44) Scheuermann, A. G.; Kemp, K. W.; Tang, K.; Lu, D. Q.; Satterthwaite, P. F.; Ito, T.; Chidsey, C. E. D.; McIntyre, P. C. Conductance and capacitance of bilayer protective oxides for silicon water splitting anodes. *Energy Environ. Sci.* **2016**.

(45) Gu, J.; Aguiar, J. A.; Ferrere, S.; Steirer, K. X.; Yan, Y.; Xiao, C.; Young, J. L.; Al-Jassim, M.; Neale, N. R.; Turner, J. A. A graded catalytic-protective layer for an efficient and stable water-splitting photocathode. *Nat. Energy* **2017**.

(46) Abe, R. Recent progress on photocatalytic and photoelectrochemical water splitting under visible light irradiation. *Journal of Photochemistry and Photobiology C: Photochemistry Reviews*. 2010.

(47) Kim, D.; Sakimoto, K. K.; Hong, D.; Yang, P. Artificial photosynthesis for sustainable fuel and chemical production. *Angew. Chemie - Int. Ed.* **2015**.

(48) Bu, Y.; Ao, J. P. A review on photoelectrochemical cathodic protection semiconductor thin films for metals. *Green Energy and Environment*. 2017.

(49) Crespo-Quesada, M.; Reisner, E. Emerging approaches to stabilise photocorrodible electrodes and catalysts for solar fuel applications. *Energy and Environmental Science*. 2017.

(50) Jiang, C.; Moniz, S. J. A.; Wang, A.; Zhang, T.; Tang, J. Photoelectrochemical devices for solar water splitting-materials and challenges. *Chemical Society Reviews*. 2017, pp 4645–4660.

(51) Seger, B.; Pedersen, T.; Laursen, A. B.; Vesborg, P. C. K.; Hansen, O.; Chorkendorff,

I. Using TiO2 as a Conductive Protective Layer for Photocathodic H-2 Evolution. *J. Am. Chem. Soc.* **2013**, *135*, 1057–1064.

(52) Hengerer, R.; Bolliger, B.; Erbudak, M.; Grätzel, M. Structure and stability of the anatase TiO2 (101) and (001) surfaces. *Surf. Sci.* **2000**.

(53) Hu, S.; Shaner, M. R.; Beardslee, J. A.; Lichterman, M.; Brunschwig, B. S.; Lewis, N. S. Amorphous TiO2 coatings stabilize Si, GaAs, and GaP photoanodes for efficient water oxidation. *Science (80-.).* **2014**, *344*, 1005–1009.

(54) Azevedo, J.; Tilley, S. D.; Schreier, M.; Stefik, M.; Sousa, C.; Araújo, J. P.; Mendes, A.; Grätzel, M.; Mayer, M. T. Tin oxide as stable protective layer for composite cuprous oxide water-splitting photocathodes. *Nano Energy* **2016**, *24*, 10–16.

(55) Laskowski, F. A. L.; Nellist, M. R.; Venkatkarthick, R.; Boettcher, S. W. Junction behavior of n-Si photoanodes protected by thin Ni elucidated from dual working electrode photoelectrochemistry. *Energy Environ. Sci.* **2017**, *10*, 570–579.

(56) Lin, F.; Boettcher, S. W. Adaptive semiconductor/electrocatalyst junctions in water-splitting photoanodes. *Nat Mater* **2013**, *13*, 81–86.

(57) Smith, R. D. L.; Prévot, M. S.; Fagan, R. D.; Trudel, S.; Berlinguette, C. P. Water oxidation catalysis: Electrocatalytic response to metal stoichiometry in amorphous metal oxide films containing iron, cobalt, and nickel. *J. Am. Chem. Soc.* **2013**.

(58) Laskowski, F. A. L.; Nellist, M. R.; R, V.; Boettcher, S. Junction Behavior of n-Si Photoanodes Protected by Thin Ni Elucidated from Dual Working Electrode Photoelectrochemistry. *Energy Environ. Sci.* **2017**, *10*, 570–579.

(59) Särkkä, H.; Bhatnagar, A.; Sillanpää, M. Recent developments of electro-oxidation in water treatment - A review. *Journal of Electroanalytical Chemistry*. 2015.

(60) Badia-Bou, L.; Mas-Marza, E.; Rodenas, P.; Barea, E. M.; Fabregat-Santiago, F.; Gimenez, S.; Peris, E.; Bisquert, J. Water oxidation at hematite photoelectrodes with an iridium-based catalyst. *J. Phys. Chem. C* **2013**.

(61) Diaz-Morales, O.; Raaijman, S.; Kortlever, R.; Kooyman, P. J.; Wezendonk, T.; Gascon, J.; Fu, W. T.; Koper, M. T. M. Iridium-based double perovskites for efficient water oxidation in acid media. *Nat. Commun.* **2016**.

(62) Smith, R. D. L.; Sporinova, B.; Fagan, R. D.; Trudel, S.; Berlinguette, C. P. Facile

photochemical preparation of amorphous iridium oxide films for water oxidation catalysis. *Chem. Mater.* **2014**.

(63) Duan, L.; Araujo, C. M.; Ahlquist, M. S. G.; Sun, L. Highly efficient and robust molecular ruthenium catalysts for water oxidation. *Proc. Natl. Acad. Sci. U. S. A.* **2012**.

(64) Harriman, A.; Pickering, I. J.; Thomas, J. M.; Christensen, P. A. Metal oxides as heterogeneous catalysts for oxygen evolution under photochemical conditions. *J. Chem. Soc. Faraday Trans. 1 Phys. Chem. Condens. Phases* **1988**.

(65) McEwen, R. S. Crystallographic studies on nickel hydroxide and the higher nickel oxides. *J. Phys. Chem.* **1971**.

(66) Payne, B. P.; Biesinger, M. C.; McIntyre, N. S. The study of polycrystalline nickel metal oxidation by water vapour. *J. Electron Spectros. Relat. Phenomena* **2009**.

(67) Tang, C. W.; Wang, C. Bin; Chien, S. H. Characterization of cobalt oxides studied by FT-IR, Raman, TPR and TG-MS. *Thermochim. Acta* **2008**.

(68) Indra, A.; Menezes, P. W.; Sahraie, N. R.; Bergmann, A.; Das, C.; Tallarida, M.; Schmeißer, D.; Strasser, P.; Driess, M. Unification of catalytic water oxidation and oxygen reduction reactions: Amorphous beat crystalline cobalt iron oxides. *J. Am. Chem. Soc.* **2014**.

(69) Takashima, T.; Hashimoto, K.; Nakamura, R. Mechanisms of pH-dependent activity for water oxidation to molecular oxygen by MnO 2 electrocatalysts. *J. Am. Chem. Soc.* **2012**.

(70) Gorlin, Y.; Jaramillo, T. F. A bifunctional nonprecious metal catalyst for oxygen reduction and water oxidation. *J. Am. Chem. Soc.* **2010**.

(71) Sivula, K. Metal oxide photoelectrodes for solar fuel production, surface traps, and catalysis. *Journal of Physical Chemistry Letters*. **2013**.

(72) Kuo, C. H.; Mosa, I. M.; Poyraz, A. S.; Biswas, S.; El-Sawy, A. M.; Song, W.; Luo, Z.; Chen, S. Y.; Rusling, J. F.; He, J.; et al. Robust mesoporous manganese oxide catalysts for water oxidation. *ACS Catal.* **2015**.

(73) Mu, A.; Scheu, C.; Pokharel, A.; Bo, S.; Bein, T.; Fattakhova-rohlfing, D. Iron-Doped Nickel Oxide Nanocrystals Alkaline Water Splitting. *ACS Nano* **2015**.

(74) Fominykh, K.; Chernev, P.; Zaharieva, I.; Sicklinger, J.; Stefanic, G.; Döblinger, M.; Müller, A.; Pokharel, A.; Böcklein, S.; Scheu, C.; et al. Iron-doped nickel oxide nanocrystals as highly efficient electrocatalysts for alkaline water splitting. *ACS Nano* **2015**.

(75) Li, N.; Bediako, D. K.; Hadt, R. G.; Hayes, D.; Kempa, T. J.; Von Cube, F.; Bell, D. C.; Chen, L. X.; Nocera, D. G. Influence of iron doping on tetravalent nickel content in catalytic oxygen evolving films. *Proc. Natl. Acad. Sci. U. S. A.* **2017**.

(76) Ahn, H. S.; Bard, A. J. Surface interrogation of CoPi water oxidation catalyst by scanning electrochemical microscopy. *J. Am. Chem. Soc.* **2015**.

(77) Cobo, S.; Heidkamp, J.; Jacques, P. A.; Fize, J.; Fourmond, V.; Guetaz, L.; Jousselme, B.; Ivanova, V.; Dau, H.; Palacin, S.; et al. A Janus cobalt-based catalytic material for electro-splitting of water. *Nat. Mater.* **2012**.

(78) Ma, Y.; Kafizas, A.; Pendlebury, S. R.; Le Formal, F.; Durrant, J. R. Photoinduced Absorption Spectroscopy of CoPi on BiVO4: The Function of CoPi during Water Oxidation. *Adv. Funct. Mater.* **2016**.

(79) Alayoglu, S.; Nilekar, A. U.; Mavrikakis, M.; Eichhorn, B. Ru-Pt core-shell nanoparticles for preferential oxidation of carbon monoxide in hydrogen. *Nat. Mater.* **2008**.

(80) Strmcnik, D.; Lopes, P. P.; Genorio, B.; Stamenkovic, V. R.; Markovic, N. M. Design principles for hydrogen evolution reaction catalyst materials. *Nano Energy* **2016**.

(81) Ojha, K.; Saha, S.; Dagar, P.; Ganguli, A. K. Nanocatalysts for hydrogen evolution reactions. *Phys. Chem. Chem. Phys.* **2018**.

(82) Dominey, R. N.; Lewis, N. S.; Bruce, J. A.; Bookbinder, D. C.; Wrighton, M. S. IMPROVEMENT OF PHOTO-ELECTROCHEMICAL HYDROGEN GENERATION BY SURFACE MODIFICATION OF P-TYPE SILICON SEMICONDUCTOR PHOTO-CATHODES. *J. Am. Chem. Soc.* **1982**, *104*, 467–482.

(83) Ho, C. Y.; Chiu, S. H.; Ke, J. J.; Tsai, K. T.; Dai, Y. A.; Hsu, J. H.; Chang, M. L.; He, J. H. Contact behavior of focused ion beam deposited Pt on p-type Si nanowires. *Nanotechnology* **2010**.

(84) Merki, D.; Hu, X. Recent developments of molybdenum and tungsten sulfides as hydrogen evolution catalysts. *Energy and Environmental Science*. **2011**.

(85) Jaramillo, T. F.; Jørgensen, K. P.; Bonde, J.; Nielsen, J. H.; Horch, S.; Chorkendorff, I. Identification of active edge sites for electrochemical H2 evolution from MoS2 nanocatalysts. *Science (80-.).* **2007**.

(86) Laskowski, F. A. L. L.; Sivula, K.; Hajibabaei, H.; Nellist, M. R.; Hamann, T. W.;

Qiu, J.; Boettcher, S. W.; Laskowski, F. A. L. L.; Qiu, J.; Hajibabaei, H.; et al. Potential-sensing electrochemical atomic force microscopy for in operando analysis of water-splitting catalysts and interfaces. *Nat. Energy* **2017**, *3*, 46–52.

(87) Barroso, M.; Mesa, C. A.; Pendlebury, S. R.; Cowan, A. J.; Hisatomi, T.; Sivula, K.; Grätzel, M.; Klug, D. R.; Durrant, J. R. Dynamics of photogenerated holes in surface modified α-Fe 2O3 photoanodes for solar water splitting. *Proc. Natl. Acad. Sci. U. S. A.* **2012**.

(88) Jung, S.; McCrory, C. C. L.; Ferrer, I. M.; Peters, J. C.; Jaramillo, T. F. Benchmarking nanoparticulate metal oxide electrocatalysts for the alkaline water oxidation reaction. *J. Mater. Chem. A* **2016**.

(89) Binda, M. Deposition and patterning techniques for Organic Semiconductors Solution processable materials : deposition techniques. *Org. Electron. Princ. Devices Appl.* **2011**.

(90) Su, J.; Guo, L.; Bao, N.; Grimes, C. A. Nanostructured WO3/BiVO4 heterojunction films for efficient photoelectrochemical water splitting. *Nano Lett.* **2011**.

(91) Mitzi, D. B.; Kosbar, L. L.; Murray, C. E.; Copel, M.; Afzali, A. High-mobility ultrathin semiconducting films prepared by spin coating. *Nature* **2004**.

(92) Mane, R. S.; Lokhande, C. D. Chemical deposition method for metal chalcogenide thin films. *Materials Chemistry and Physics*. **2000**.

(93) Cheng, J.; Fan, D. B. F.; Wang, H.; Liu, B. W.; Zhang, Y. C.; Yan, H. Chemical bath deposition of crystalline ZnS thin films. *Semicond. Sci. Technol.* **2003**.

(94) Kang, D.; Kim, T. W.; Kubota, S. R.; Cardiel, A. C.; Cha, H. G.; Choi, K. S. Electrochemical Synthesis of Photoelectrodes and Catalysts for Use in Solar Water Splitting. *Chemical Reviews*. **2015**.

(95) Ismail, A. A.; Bahnemann, D. W. Photochemical splitting of water for hydrogen production by photocatalysis: A review. *Solar Energy Materials and Solar Cells*. **2014**.

(96) Dias, P.; Vilanova, A.; Lopes, T.; Andrade, L.; Mendes, A. Extremely stable bare hematite photoanode for solar water splitting. *Nano Energy* **2016**.

(97) Lorentzou, S.; Agrafiotis, C. C.; Konstandopoulos, A. G. Aerosol spray pyrolysis synthesis of water-splitting ferrites for solar hydrogen production. *Granul. Matter* **2008**.

(98) Contreras, M. A.; Romero, M. J.; To, B.; Hasoon, F.; Noufi, R.; Ward, S.; Ramanathan, K. Optimization of CBD CdS process in high-efficiency Cu(In,Ga)Se2-based solar cells. In

Thin Solid Films; **2002**.

(99) Abou-Ras, D.; Kostorz, G.; Romeo, A.; Rudmann, D.; Tiwari, A. N. Structural and chemical investigations of CBD- and PVD-CdS buffer layers and interfaces in Cu(In,Ga)Se 2 -based thin film solar cells. In *Thin Solid Films*; **2005**.

(100) Engelhardt, F.; Bornemann, L.; Köntges, M.; Meyer, T.; Parisi, J.; Pschorr-Schoberer, E.; Hahn, B.; Gebhardt, W.; Riedl, W.; Rau, U. Cu(In,Ga)Se 2 solar cells with a ZnSe buffer layer: Interface characterization by quantum efficiency measurements. *Prog. Photovoltaics Res. Appl.* **1999**.

(101) Adegoke, O.; Nyokong, T.; Forbes, P. B. C. Deposition of CdS, CdS/ZnSe and CdS/ZnSe/ZnS shells around CdSeTe alloyed core quantum dots: Effects on optical properties. *Luminescence* **2016**.

(102) Lu, Y.; Meng, X.; Yi, G.; Jia, J. In situ growth of CuS thin films on functionalized self-assembled monolayers using chemical bath deposition. *J. Colloid Interface Sci.* **2011**.

(103) Sangamesha, M. A.; Pushpalatha, K.; Shekar, G. L.; Shamsundar, S. Preparation and Characterization of Nanocrystalline CuS Thin Films for Dye-Sensitized Solar cells. *ISRN Nanomater.* **2013**.

(104) Ahire, R. R.; Deshpande, N. G.; Gudage, Y. G.; Sagade, A. A.; Chavhan, S. D.; Phase, D. M.; Sharma, R. A comparative study of the physical properties of CdS, Bi2S3 and composite CdS-Bi2S3 thin films for photosensor application. *Sensors Actuators, A Phys.* **2007**.

(105) Ibanez, J. G.; Gomez, F.; Konik, I.; Lozano, D. E.; Mugica, A.; Singh, M. M.; Szafran, Z.; Pike, R. M. Preparation of Semiconducting Materials in the Laboratory, Part 2: Microscale Chemical Bath Deposition of Materials with Band Gap Energies in the UV, VIS, and IR. *J. Chem. Educ.* **1997**.

(106) Kokotov, M.; Biller, A.; Hodes, G. Reproducible chemical bath deposition of ZnO by a one-step method: The importance of "contaminants" in nucleation. *Chem. Mater.* **2008**.

(107) Sobha Jayakrishnan, D. Electrodeposition: The versatile technique for nanomaterials. In *Corrosion Protection and Control Using Nanomaterials*; 2012.

(108) Williamson, M. J.; Tromp, R. M.; Vereecken, P. M.; Hull, R.; Ross, F. M. Dynamic microscopy of nanoscale cluster growth at the solid-liquid interface. *Nature Materials*. 2003.

(109) Gabe, D. R. Electrodepositlon: the materials science of coatings and substrates. *Br.*

Corros. J. **2013**.

(110) Zhang, Z.; Wang, P. Highly stable copper oxide composite as an effective photocathode for water splitting via a facile electrochemical synthesis strategy. *J. Mater. Chem.* **2012**.

(111) Wick, R.; Tilley, S. D. Photovoltaic and Photoelectrochemical Solar Energy Conversion with Cu2O. *J. Phys. Chem. C* **2015**.

(112) Paracchino, A.; Laporte, V.; Sivula, K.; Grätzel, M.; Thimsen, E.; Gratzel, M.; Thimsen, E. Highly active oxide photocathode for photoelectrochemical water reduction. *Nat. Mater.* **2011**, *10*, 456–461.

(113) Yao, B. D.; Chan, Y. F.; Wang, N. Formation of ZnO nanostructures by a simple way of thermal evaporation. *Appl. Phys. Lett.* **2002**.

(114) Han, J. G. Recent progress in thin film processing by magnetron sputtering with plasma diagnostics. *J. Phys. D. Appl. Phys.* **2009**.

(115) Bishop, C. A. Electron Beam (E-beam) Evaporation. In *Vacuum Deposition onto Webs, Films and Foils*; **2011**.

(116) Shen, J.; Gai, Z.; Kirschner, J. Growth and magnetism of metallic thin films and multilayers by pulsed-laser deposition. *Surface Science Reports*. **2004**.

(117) Scragg, J. J.; Kubart, T.; Wätjen, J. T.; Ericson, T.; Linnarsson, M. K.; Platzer-Björkman, C. Effects of back contact instability on Cu2ZnSnS4 devices and processes. *Chem. Mater.* **2013**.

(118) Mei, B.; Pedersen, T.; Malacrida, P.; Bae, D.; Frydendal, R.; Hansen, O.; Vesborg, P. C. K.; Seger, B.; Chorkendorff, I. Crystalline TiO2: A Generic and Effective Electron-Conducting Protection Layer for Photoanodes and -cathodes. *J. Phys. Chem. C* **2015**, *119*, 15019–15027.

(119) Sun, K.; Saadi, F. H.; Lichterman, M. F.; Hale, W. G.; Wang, H.-P.; Zhou, X.; Plymale, N. T.; Omelchenko, S. T.; He, J.-H.; Papadantonakis, K. M.; et al. *Stable solar-driven oxidation of water by semiconducting photoanodes protected by transparent catalytic nickel oxide films*; 2015.

(120) Husain, M.; Singh, B. P.; Kumar, S.; Sharma, T. P.; Sebastian, P. J. Optical, electrical and structural investigations on Cd1-xZnxSe sintered films for photovoltaic applications. *Sol.*

Energy Mater. Sol. Cells **2003**.

(121) Rani, S.; Rajan, S. T.; Shanthi, J.; Ayeshamariam, A.; Jayachandran, M. Review on the materials properties and photoelctrochemical (PEC) solar cells of CdSe, Cd1-x ZnxSe, Cd1-x InxSe, thin films. *Materials Science Forum*. **2015**.

(122) Koh, J.; Ferlauto, A. S.; Rovira, P. I.; Wronski, C. R.; Collins, R. W. Evolutionary phase diagrams for plasma-enhanced chemical vapor deposition of silicon thin films from hydrogen-diluted silane. *Appl. Phys. Lett.* **1999**.

(123) Tucci, M. Optimization of n-doping in n-type a-SI : H/p-type textured c-Si heterojunction for photovoltaic applications. *Sol. Energy Mater. Sol. Cells* **1999**.

(124) Ujiie, Y.; Nishinaga, T. Epitaxial lateral overgrowth of gaas on a si substrate. *Jpn. J. Appl. Phys.* **1989**.

(125) Kay, A.; Cesar, I.; Grätzel, M. New benchmark for water photooxidation by nanostructured α-Fe 2O3 films. *J. Am. Chem. Soc.* **2006**.

(126) Lee, D. J.; Kim, H. M.; Kwon, J. Y.; Choi, H.; Kim, S. H.; Kim, K. B. Structural and electrical properties of atomic layer deposited Al-doped ZnO films. *Adv. Funct. Mater.* **2011**.

(127) Parsons, G. N.; George, S. M.; Knez, M. Progress and future directions for atomic layer deposition and ALD-based chemistry. *MRS Bull.* **2011**.

(128) Son, M. K.; Steier, L.; Schreier, M.; Mayer, M. T.; Luo, J.; Grätzel, M. A copper nickel mixed oxide hole selective layer for Au-free transparent cuprous oxide photocathodes. *Energy Environ. Sci.* **2017**.

(129) Shah, A. V. *Thin-film silicon solar cells*; 2010.

(130) Malizia, M.; Seger, B.; Chorkendorff, I.; Vesborg, P. C. K. Formation of a p-n heterojunction on GaP photocathodes for H2 production providing an open-circuit voltage of 710 mV. *J. Mater. Chem. A* **2014**, *2*, 6847–6853.

(131) Seger, B.; Laursen, A. B.; Vesborg, P. C. K.; Pedersen, T.; Hansen, O.; Dahl, S.; Chorkendorff, I. Hydrogen production using a molybdenum sulfide catalyst on a titanium-protected n(+)p-silicon photocathode. *Angew Chem Int Ed Engl* **2012**, *51*, 9128–9131.

(132) Shinagawa, T.; Takanabe, K. Towards Versatile and Sustainable Hydrogen Production through Electrocatalytic Water Splitting: Electrolyte Engineering. *ChemSusChem*. **2017**.

(133) Nakato, Y.; Egi, Y.; Hiramoto, M.; Tsubomura, H. HYDROGEN EVOLUTION AND IODINE REDUCTION ON AN ILLUMINATED N-P JUNCTION SILICON ELECTRODE AND ITS APPLICATION TO EFFICIENT SOLAR PHOTOELECTROLYSIS OF HYDROGEN IODIDE. *J. Phys. Chem.* **1984**, *88*, 4218–4222.

(134) Boettcher, S. W.; Warren, E. L.; Putnam, M. C.; Santori, E. A.; Turner-Evans, D.; Kelzenberg, M. D.; Walter, M. G.; McKone, J. R.; Brunschwig, B. S.; Atwater, H. A.; et al. Photoelectrochemical Hydrogen Evolution Using Si Microwire Arrays. *J. Am. Chem. Soc.* **2011**, *133*, 1216–1219.

(135) Huang, Q.; Ye, Z.; Xiao, X. Recent progress in photocathodes for hydrogen evolution. *J. Mater. Chem. A* **2015**, *3*, 15824–15837.

(136) Hisatomi, T.; Kubota, J.; Domen, K. Recent advances in semiconductors for photocatalytic and photoelectrochemical water splitting. *Chem. Soc. Rev.* **2014**, *43*, 7520–7535.

(137) Zhang, Z.; Yates, J. T. Band Bending in Semiconductors: Chemical and Physical Consequences at Surfaces and Interfaces. *Chem. Rev.* **2012**, *112*, 5520–5551.

(138) Pham, T. A.; Ping, Y.; Galli, G. Modelling heterogeneous interfaces for solar water splitting. *Nat. Mater.* **2017**, No. January, 1–8.

(139) Nakato, Y.; Ohnishi, T.; Tsubomura, H. PHOTO-ELECTROCHEMICAL BEHAVIORS OF SEMICONDUCTOR ELECTRODES COATED WITH THIN METAL FILMS. *Chem. Lett.* **1975**, *4*, 883–886.

(140) PINSON, W. E. Quasi-Fermi level measurement in an illuminated GaP photoelectrolysis cell. *Nature* **1977**, *269*, 316–318.

(141) Wilson, R.; Harris, L.; Gerstner, M. The Potential of the Gold Overlayer on n ‐ GaP Photoelectrodes. *J. Electrochem. Soc.* **1977**, *124*, 2–3.

(142) Hodes, G.; Thompson, L.; Dubow, J.; Rajeshwar, K. Heterojunction Silicon/Indium Tin Oxide Photoelectrodes: Development of stable systems in aqueous electrolytes and their applicability to solar energy conversion and storage. *J. Am. Chem. Soc.* **1983**, *1289*, 324–330.

(143) White, J. R.; Fan, F.-R. F.; Bard, A. J. Semiconductor Electrodes. LVI. Principles of Multijunction Electrodes and Photoelectrosynthesis at Texas Instruments' p/n-Si Solar Arrays. *J. Electrochem. Soc.* **1985**, *132*, 544–550.

(144) Gu, J.; Yan, Y.; Young, J. L.; Steirer, K. X.; Neale, N. R.; Turner, J. a. Water reduction

by a p-GaInP2 photoelectrode stabilized by an amorphous TiO2 coating and a molecular cobalt catalyst. *Nat. Mater.* **2015**, *15*, 456.

(145) Fountaine, K. T.; Lewerenz, H. J.; Atwater, H. A. Efficiency limits for photoelectrochemical water-splitting. *Nat. Commun.* **2016**, *7*, 13706.

(146) Kemppainen, E.; Bodin, A.; Sebok, B.; Pedersen, T.; Seger, B.; Mei, B.; Bae, D.; Vesborg, P. C. K. K.; Halme, J.; Hansen, O.; et al. Scalability and feasibility of photoelectrochemical H2 evolution: the ultimate limit of Pt nanoparticle as an HER catalyst. *Energy Environ. Sci.* **2015**, *8*, 2991–2999.

(147) Cui, W.; Ge, C.; Xing, Z.; Asiri, A. M.; Sun, X. NixSy-MoS2 hybrid microspheres: One-pot hydrothermal synthesis and their application as a novel hydrogen evolution reaction electrocatalyst with enhanced activity. *Electrochim. Acta* **2014**, *137*, 504–510.

(148) Tran, P. D.; Pramana, S. S.; Kale, V. S.; Nguyen, M.; Chiam, S. Y.; Batabyal, S. K.; Wong, L. H.; Barber, J.; Loo, J. Novel assembly of an MoS 2 electrocatalyst onto a silicon nanowire array electrode to construct a photocathode composed of elements abundant on the earth for hydrogen generation. *Chemistry - A European Journal*. **2012**, pp 13994–13999.

(149) Hisatomi, T.; Kubota, J.; Domen, K. Recent advances in semiconductors for photocatalytic and photoelectrochemical water splitting. *Chem. Soc. Rev.* **2014**, *43*, 7520–7535.

(150) Seger, B.; Tilley, D. S.; Pedersen, T.; Vesborg, P. C. K. K.; Hansen, O.; Gratzel, M.; Chorkendorff, I.; Grätzel, M.; Chorkendorff, I. Silicon protected with atomic layer deposited TiO2: durability studies of photocathodic H-2 evolution. *Rsc Adv.* **2013**, *3*, 25902–25907.

(151) Richards, B. S. Comparison of TiO2 and other dielectric coatings for buried-contact solar cells: a review. *Prog. Photovoltaics* **2004**, *12*, 253–281.

(152) Paracchino, A.; Laporte, V.; Sivula, K.; Gratzel, M.; Thimsen, E. Highly active oxide photocathode for photoelectrochemical water reduction. *Nat Mater* **2011**, *10*, 456–461.

(153) Li, C.; Hisatomi, T.; Watanabe, O.; Nakabayashi, M.; Shibata, N.; Domen, K.; Delaunay, J.-J. Positive onset potential and stability of Cu2O-based photocathodes in water splitting by atomic layer deposition of a Ga2O3buffer layer. *Energy Environ. Sci.* **2015**, *8*, 1493–1500.

(154) Lee, Y. S.; Chua, D.; Brandt, R. E.; Siah, S. C.; Li, J. V; Mailoa, J. P.; Lee, S. W.; Gordon, R. G.; Buonassisi, T. Atomic layer deposited gallium oxide buffer layer enables 1.2 V

open-circuit voltage in cuprous oxide solar cells. *Adv Mater* **2014**, *26*, 4704–4710.

(155) Minami, T.; Nishi, Y.; Miyata, T.; Nomoto, J. I. High-Efficiency Oxide Solar Cells with ZnO/Cu2O Heterojunction Fabricated on Thermally Oxidized Cu2O Sheets. *Appl. Phys. Express* **2011**, *4*, 62301.

(156) Minami, T.; Nishi, Y.; Miyata, T. High-Efficiency Cu2O-Based Heterojunction Solar Cells Fabricated Using a Ga2O3Thin Film as N-Type Layer. *Appl. Phys. Express* **2013**, *6*, 44101.

(157) Mittiga, A.; Biccari, F.; Malerba, C. Intrinsic defects and metastability effects in Cu2O. *Thin Solid Films* **2009**.

(158) Maghraoui-Meherzi, H.; Ben Nasr, T.; Dachraoui, M. Synthesis, structure and optical properties of Sb2Se3. *Mater. Sci. Semicond. Process.* **2013**.

(159) Wang, L.; Li, D. B.; Li, K.; Chen, C.; Deng, H. X.; Gao, L.; Zhao, Y.; Jiang, F.; Li, L.; Huang, F.; et al. Stable 6%-efficient Sb2Se3 solar cells with a ZnO buffer layer. *Nat. Energy* **2017**.

(160) Prabhakar, R. R.; Septina, W.; Siol, S.; Moehl, T.; Wick-Joliat, R.; Tilley, S. D. Photocorrosion-resistant Sb2Se3 photocathodes with earth abundant MoSx hydrogen evolution catalyst. *J. Mater. Chem. A* **2017**, *5*, 23139–23145.

(161) Tumelero, M. A.; Faccio, R.; Pasa, A. A. Unraveling the native conduction of trichalcogenides and its ideal band alignment for new photovoltaic interfaces. *J. Phys. Chem. C* **2016**.

(162) Lei, H.; Yang, G.; Guo, Y.; Xiong, L.; Qin, P.; Dai, X.; Zheng, X.; Ke, W.; Tao, H.; Chen, Z.; et al. Efficient planar Sb2S3 solar cells using a low-temperature solution-processed tin oxide electron conductor. *Phys. Chem. Chem. Phys.* **2016**.

(163) Iyer, A.; Kearney, K.; Wakayama, S.; Odoi, H.; Ertekin, E. Design Strategy for the Molecular Functionalization of Semiconductor Photoelectrodes: A Case Study of p-Si(111) Photocathodes for H 2 Generation. *Langmuir* **2018**.

(164) Wick-Joliat, R.; Musso, T.; Prabhakar, R. R.; Löckinger, J.; Siol, S.; Cui, W.; Sévery, L.; Moehl, T.; Suh, J.; Hutter, J.; et al. Stable and tunable phosphonic acid dipole layer for band edge engineering of photoelectrochemical and photovoltaic heterojunction devices. *Energy Environ. Sci.* **2019**.

(165) Aspnes, D. E. Recombination at semiconductor surfaces and interfaces. *Surf. Sci.* **1983**.

(166) Li, J.; Wu, N. Semiconductor-based photocatalysts and photoelectrochemical cells for solar fuel generation: A review. *Catalysis Science and Technology*. **2015**.

(167) Steinmiller, E. M. P.; Choi, K. S. Photochemical deposition of cobalt-based oxygen evolving catalyst on a semiconductor photoanode for solar oxygen production. *Proc. Natl. Acad. Sci. U. S. A.* **2009**.

(168) Zhang, M.; Luo, W.; Zhang, N.; Li, Z.; Yu, T.; Zou, Z. A facile strategy to passivate surface states on the undoped hematite photoanode for water splitting. *Electrochem. commun.* **2012**.

(169) Laskowski, F. A. L.; Nellist, M. R.; Qiu, J.; Boettcher, S. W. Metal Oxide/(oxy)hydroxide Overlayers as Hole Collectors and Oxygen-Evolution Catalysts on Water-Splitting Photoanodes. *J. Am. Chem. Soc.* **2019**, *141*, 1394–1405.

(170) Lin, F.; Boettcher, S. W. Adaptive semiconductor/electrocatalyst junctions in water-splitting photoanodes. *Nat. Mater.* **2014**, *13*, 81–86.

(171) Friebel, D.; Louie, M. W.; Bajdich, M.; Sanwald, K. E.; Cai, Y.; Wise, A. M.; Cheng, M. J.; Sokaras, D.; Weng, T. C.; Alonso-Mori, R.; et al. Identification of highly active Fe sites in (Ni,Fe)OOH for electrocatalytic water splitting. *J. Am. Chem. Soc.* **2015**.

(172) Klahr, B.; Gimenez, S.; Fabregat-Santiago, F.; Bisquert, J.; Hamann, T. W. Photoelectrochemical and impedance spectroscopic investigation of water oxidation with “co-Pi”-coated hematite electrodes. *J. Am. Chem. Soc.* **2012**, *134*, 16693–16700.

(173) Bertoluzzi, L.; Lopez-Varo, P.; Jiménez Tejada, J. A.; Bisquert, J. Charge transfer processes at the semiconductor/electrolyte interface for solar fuel production: Insight from impedance spectroscopy. *J. Mater. Chem. A* **2016**, *4*, 2873–2879.

(174) Moehl, T.; Cui, W.; Wick-Joliat, R.; Tilley, S. D. Resistance-based analysis of limiting interfaces in multilayer water splitting photocathodes by impedance spectroscopy. *Sustain. Energy Fuels* **2019**.

(175) Li, X.; Yu, J.; Low, J.; Fang, Y.; Xiao, J.; Chen, X. Engineering heterogeneous semiconductors for solar water splitting. *Journal of Materials Chemistry A*. 2015, pp 2485–2534.

(176) Moehl, T.; Suh, J.; Sévery, L.; Wick-Joliat, R.; Tilley, S. D. Investigation of (Leaky)

ALD TiO2 Protection Layers for Water-Splitting Photoelectrodes. *ACS Appl. Mater. Interfaces* **2017**, *9*, 43614–43622.

(177) Thorne, J. E.; Jang, J. W.; Liu, E. Y.; Wang, D. Understanding the origin of photoelectrode performance enhancement by probing surface kinetics. *Chem. Sci.* **2016**, *7*, 3347–3354.

(178) Chen, Y. W.; Prange, J. D.; Dühnen, S.; Park, Y.; Gunji, M.; Chidsey, C. E. D.; McIntyre, P. C. Atomic layer-deposited tunnel oxide stabilizes silicon photoanodes for water oxidation. *Nat. Mater.* **2011**, *10*, 539–544.

(179) Scheuermann, A. G.; Prange, J. D.; Gunji, M.; Chidsey, C. E. D.; McIntyre, P. C. Effects of catalyst material and atomic layer deposited TiO2 oxide thickness on the water oxidation performance of metal-insulator-silicon anodes. *Energy Environ. Sci.* **2013**, *6*, 2487–2496.

(180) Digdaya, I. A.; Trześniewski, B. J.; Adhyaksa, G. W. P.; Garnett, E. C.; Smith, W. A. General Considerations for Improving Photovoltage in Metal-Insulator-Semiconductor Photoanodes. *J. Phys. Chem. C* **2018**, *122*, 5462–5471.

(181) McDowell, M. T.; Lichterman, M. F.; Carim, A. I.; Liu, R.; Hu, S.; Brunschwig, B. S.; Lewis, N. S. The Influence of Structure and Processing on the Behavior of TiO2 Protective Layers for Stabilization of n-Si/TiO2/Ni Photoanodes for Water Oxidation. *ACS Appl. Mater. Interfaces* **2015**.

(182) Pham, H. H.; Wang, L. W. Oxygen vacancy and hole conduction in amorphous TiO2. *Phys. Chem. Chem. Phys.* **2015**, *17*, 541–550.

(183) Deskins, N. A.; Du, J.; Rao, P. The structural and electronic properties of reduced amorphous titania. *Phys. Chem. Chem. Phys.* **2017**, *19*, 18671–18684.

(184) Mattioli, G.; Filippone, F.; Alippi, P.; Amore Bonapasta, A. Ab initio study of the electronic states induced by oxygen vacancies in rutile and anatase TiO2. *Phys. Rev. B - Condens. Matter Mater. Phys.* **2008**, *78*.

(185) Cheung, S. H.; Nachimuthu, P.; Joly, A. G.; Engelhard, M. H.; Bowman, M. K.; Chambers, S. A. N incorporation and electronic structure in N-doped TiO2(1 1 0) rutile. *Surf. Sci.* **2007**, *601*, 1754–1762.

(186) Cui, W.; Niu, W.; Wick-Joliat, R.; Moehl, T.; Tilley, S. D. Operando deconvolution

of photovoltaic and electrocatalytic performance in ALD TiO2 protected water splitting photocathodes. *Chem. Sci.* **2018**, *9*, 6062–6067.

(187) Cui, C.; Heggen, M.; Zabka, W. D.; Cui, W.; Osterwalder, J.; Probst, B.; Alberto, R. Atomically dispersed hybrid nickel-iridium sites for photoelectrocatalysis. *Nat. Commun.* **2017**, *8*.

(188) Hu, S.; Richter, M. H.; Lichterman, M. F.; Beardslee, J.; Mayer, T.; Brunschwig, B. S.; Lewis, N. S. Electrical, Photoelectrochemical, and Photoelectron Spectroscopic Investigation of the Interfacial Transport and Energetics of Amorphous TiO 2 /Si Heterojunctions. *J. Phys. Chem. C* **2016**, *120*, 3117–3129.

(189) Digdaya, I. A.; Adhyaksa, G. W. P.; Trześniewski, B. J.; Garnett, E. C.; Smith, W. A. Interfacial engineering of metal-insulator-semiconductor junctions for efficient and stable photoelectrochemical water oxidation. *Nat. Commun.* **2017**, *8*.

(190) Nunez, P.; Richter, M. H.; Piercy, B. D.; Roske, C. W.; Cabán-Acevedo, M.; Losego, M. D.; Konezny, S. J.; Fermin, D. J.; Hu, S.; Brunschwig, B. S.; et al. Characterization of Electronic Transport through Amorphous TiO 2 Produced by Atomic-Layer Deposition . *J. Phys. Chem. C* **2019**.

(191) Wei Cui, Thomas Moehl, Sebastian Siol, S. D. T. Operando electrochemical study of charge carrier processes in water splitting photoanodes protected by atomic layer deposited TiO2. *Sustain. Energy Fuels* **2019**.

(192) Le Formal, F.; Pendlebury, S. R.; Cornuz, M.; Tilley, S. D.; Grätzel, M.; Durrant, J. R. Back electron-hole recombination in hematite photoanodes for water splitting. *J. Am. Chem. Soc.* **2014**.

(193) Ding, C.; Shi, J.; Wang, Z.; Li, C. Photoelectrocatalytic Water Splitting: Significance of Cocatalysts, Electrolyte, and Interfaces. *ACS Catal.* **2017**, *7*, 675–688.

(194) Nellist, M. R.; Laskowski, F. A. L.; Lin, F.; Mills, T. J.; Boettcher, S. W. Semiconductor-Electrocatalyst Interfaces: Theory, Experiment, and Applications in Photoelectrochemical Water Splitting. *Acc. Chem. Res.* **2016**, *49*, 733–740.

Curriculum Vitae and List of Publications

Name of author: Wei Cui

Education:

09.2015-10.2019：Ph.D. degree

Department of Chemistry, University of Zurich, Switzerland
Supervised by Prof. David Tilley
Thesis: *Operando* methodology: deep understanding of water splitting photoelectrodes with multilayer structures (defense date: 28. 10. 2019).

09.2012-06.2015：Master's degree

Changchun Institute of Applied Chemistry, University of Chinese Academy of Sciences, China
Supervised by Prof. Xuping Sun (The state key laboratory of electroanalytical chemistry)
Thesis: Novel Molybdenum-based electrocatalysts for hydrogen evolution reaction.

09.2008-06.2012： Bachelor's degree·

Department of Chemistry, Jilin University, China

Teaching Assistant Activities

15HS CHE321 lab course in Inorganic Chemistry II
16HS CHE171 Grundlagenpraktikum für die Life Sciences
17HS CHE328 Green Chemistry
18HS CHE171 Grundlagenpraktikum für die Life Sciences
19FS CHE153 Physikalisch-chemisches Praktikum für die Life Sciences

Publication list

1. *Operando electrochemical study of charge carrier processes in water splitting photoanodes protected by atomic layer deposited TiO_2*
   W Cui, T Moehl, R Wick-Joliat, SD Tilley
   Sustainable Energy&Fuels, in press, DOI: 10.1039/c9se00399a, 2019
2. *Resistance-based analysis of limiting interfaces in multilayer water splitting photocathodes by impedance spectroscopy*
   T Moehl, **W Cui**, R Wick-Joliat, SD Tilley

Sustainable Energy&Fuels, 3, 2067-2075, 2019

3. *Stable and tunable phosphonic acid dipole layer for band edge engineering of photoelectrochemical and photovoltaic heterojunction devices*
R Wick-Joliat, T Musso, RR Prabhakar, J Loeckinger, S Siol, **W Cui**, L Sévery, T Moehl, Jihye Suh, J Hutter, SD Tilley
Energy & Environmental Science, 12, 1901-1909, 2019.

4. *Operando deconvolution of photovoltaic and electrocatalytic performance in ALD* TiO_2 *protected water splitting photocathodes*
W Cui, W Niu, R Wick-Joliat, T Moehl, SD Tilley
Chemical science, 9, 6062-6067, 2018

5. *New Earth-abundant Materials for Large-scale Solar Fuels Generation*
RR Prabhakar, **W Cui**, SD Tilley
CHIMIA International Journal for Chemistry, 72, 333-337, 2018

6. *Extended Light Harvesting with Dual* Cu_2O *‐Based Photocathodes for High Efficiency Water Splitting*
W Niu, T Moehl, **W Cui**, R Wick‐Joliat, L Zhu, SD Tilley
Advanced Energy Materials, 8, 1702323, 2018

7. *Atomically dispersed hybrid nickel-iridium sites for photoelectrocatalysis*
C Cui, M Heggen, WD Zabka, **W Cui**, J Osterwalder, B Probst, R Alberto
Nature communications, 8, 1341, 2017

8. *Recent progress in cobalt-based heterogeneous catalysts for electrochemical water splitting*
J Wang, **W Cui**, Q Liu, Z Xing, AM Asiri, X Sun
Advanced materials, 28, 215-230, 2016

9. *MoP nanosheets supported on biomass-derived carbon flake: One-step facile preparation and application as a novel high-active electrocatalyst toward hydrogen evolution reaction*
W Cui, Q Liu, Z Xing, AM Asiri, KA Alamry, X Sun
Applied Catalysis B: Environmental, 164, 144-150, 2015

10. Mo_2C *Nanoparticles Decorated Graphitic Carbon Sheets: Biopolymer-Derived Solid-State Synthesis and Application as an Efficient Electrocatalyst for Hydrogen Generation*
W Cui, N Cheng, Q Liu, C Ge, AM Asiri, X Sun
ACS Catalysis, 4, 2658-2661, 2014

11. *Activated carbon nanotubes: a highly-active metal-free electrocatalyst for hydrogen evolution reaction*
W Cui, Q Liu, N Cheng, AM Asiri, X Sun
Chemical Communications, 50, 9340-9342, 2014

12. Ni_xS_y-MoS_2 *hybrid microspheres: One-pot hydrothermal synthesis and their application as a novel hydrogen evolution reaction electrocatalyst with enhanced activity*

W Cui, C Ge, Z Xing, AM Asiri, X Sun
Electrochimica Acta, 137, 504-510, 2014

13. *Shape-controllable synthesis of Mo2C nanostructures as hydrogen evolution reaction electrocatalysts with high activity*
C Ge, P Jiang, **W Cui**, ZH Pu, Z Xing, AM Asiri, AY Obaid, X Sun, J Tian
Electrochimica Acta, 134, 182-186, 2014

14. *Carbon nanotubes decorated with CoP nanocrystals: a Highly active non‐noble‐metal nanohybrid electrocatalyst for hydrogen evolution*
Q Liu, J Tian, **W Cui**, P Jiang, N Cheng, AM Asiri, X Sun
Angewandte Chemie International Edition, 53, 6710-6714,2014

15. *CoP nanostructures with different morphologies: synthesis, characterization and a study of their electrocatalytic performance toward the hydrogen evolution reaction*
P Jiang, Q Liu, C Ge, **W Cui**, Z Pu, AM Asiri, X Sun
Journal of Materials Chemistry A, 2, 14634-14640, 2014

International conferences

1. *Fe_2TiO_5-based photoanodes for water oxidation*
W Cui, SD Till*ey*
Poster, MRS 2016 Fall Meeting, Boston. USA

2. *Deconvolution of Photovoltaic and Electrocatalytic Performance in Water Splitting Photocathodes by Dual Working Electrode Photoelectrochemistry*
W Cui, T Moehl, R Wick-Joliat, SD Tilley
Oral talk, NanoGe 2017 September Meeting, Barcelona. Spain